2010

A Study of the Interactions of Lipid Bilayers and Dendrimers Using Small Angle X-Ray Scattering and Freeze Fracture Transmission Electron Microscopy

Derek R. Dorman
Louisiana State University and Agricultural and Mechanical College, ddorma1@lsu.edu

Recommended Citation

Dorman, Derek R., "A Study of the Interactions of Lipid Bilayers and Dendrimers Using Small Angle X-Ray Scattering and Freeze Fracture Transmission Electron Microscopy" (2010). *LSU Doctoral Dissertations*. 2923.
https://digitalcommons.lsu.edu/gradschool_dissertations/2923

A STUDY OF THE INTERACTIONS OF LIPID BILAYERS AND DENDRIMERS USING SMALL ANGLE X-RAY SCATTERING AND FREEZE FRACTURE TRANSMISSION ELECTRON MICROSCOPY

A Dissertation

Submitted to the Graduate Faculty of the
Louisiana State University and
Agriculture and Mechanical College
in partial fulfillment of the
requirements for the degree of
Doctor of Philosophy

in

The Department of Chemistry

by
Derek Richard Dorman
B.S., The University of Southern Mississippi, 2000
August 2010

DEDICATION

This dissertation is dedicated to my grandmother

Mildred Alice Flesher (1917-2008)

and friends

Samuel (Sammy) N. Broadhead III (1978-2004)

and

Kristi Gayle Throop (1980-2004)

ACKNOWLEDGEMENTS

My tenure at Louisiana State University has been an interesting journey: wrought with equipment issues and other obstacles. The expertise and support of my professors, family, and friends have brought my goal of becoming a Ph.D. chemist to fruition. I want to take the time to thank everyone and write some specific kudos here.

Dr. Paul S. Russo, Roy Paul Daniels Professor of Chemistry and my advisor, has supported me throughout my time as a graduate student. I would like to thank him for his encouragement and all the great ideas he provided along the way. Without his guidance, I would not be the scientist I am today.

To my committee: Prof. Les Butler, Prof. Jayne Garno, Prof. John Pojman, and Prof. Jeff Hanor; thank you for being so understanding, working through the extra emails that were sent for scheduling my general exam and dissertation defense, and agreeing to my academic extension. Seven years may be a long time to attend graduate school, but I believe it has paid off, making me a well versed polymer physical chemist.

Small angle X-ray scattering (SAXS) at the Center of Advanced Microstructures and Devices (CAMD) plays a starring role in this dissertation. Dr. Roland Tittsworth, Dr. Amativa Roy, Russell (Rusty) Louis, Andrew Weber, and the rest of the staff, thank you for all that you have done to make SAXS at CAMD possible. I would also like to thank Dr. John Pople at Stanford Synchrotron Radiation Laboratory (SSRL) for all his help and guidance on SAXS and Dr. Iris Torriani and Dr. Tomas Plivelicat at Laboratório Nacional de Luz Síncrotron (LNLS) for the hospitality, training, and use of their SAXS beamline.

Many highly skilled technical staff and professors have been invaluable to my research. Thank you, Dr. Rafael Cueto, for always being available to answer questions and help with GPC-MALLS, light scattering, and computer problems. Professor William (Bill) Henk and Dr. Olga Borkhsenious at LSU School of Veterinary Medicine Microscopy Center and Margaret Cindy Henk in the Socolofsky Microscopy Center in the Department of Biological Sciences taught me how to use transmission electron microscopy and showed me the tricks all good microscopists must know. I want to thank Dr. Al Coritz for teaching me how to make freeze-fractured replicas and repairing the Balzer BAF-400. I also want to recognize Prof. George Newkome at the University of Akron, Prof. George Phillies at the Worcester Polytechnic Institute, and Prof. Kiril Streletzky at Cleveland State University for providing me with interesting samples and science problems to study.

I would like to thank my former fellow Russo's Research Group members—Dr. Garrett Doucet, Dr. Jirun (Alan) Sun, Dr. Nadia Edward, Dr. Sibel Turksen, Dr. Erick Soto-Cantu, and Dr. Jianhong (Jan) Qiu—for their camaraderie. They showed me the ropes by introducing me to various laboratory instruments, sharing their experiences, and always going with me to get some coffee and talk science. I want to thank my lunch pals, Dr. Ryan Simon, Dr. Matthew Malwitz, and Jason Campbell, for all the engaging conversation.

Before I thank my friends and family, I want to express my appreciation for the funding I received for my stipend, travel, and supplies. Many thanks to the National Science Foundation for providing me funding through the Integrative Graduate Education Research Training program that enabled me to travel to SSRL in Menlo Park, California; National Institute for Standards and Technology Center for Neutron Research in Gaithersburg, Maryland; McMasters University in Hamilton, Ontario, Canada; LNLS in Campinas, Brazil; Middle Eastern Technical University in Ankara, Turkey; and the Max Planck Institute for Polymer Research in Mainz, Germany. Thanks to the LSU Department of Chemistry and the Graduate School for my TA stipend and supplement award.

My friends and family have always been there for me even if they didn't exactly understand the subject matter of the degrees I sought. I want to express my gratitude to all of those who befriended me in Baton Rouge and watched the LSU Tigers win 3 National Championship Titles with me. I would like to thank Chris Haftek for being such a good friend and him and Adam Sonnier for inviting me to all the Mardi Gras Balls and parades. I must give a special thanks to Shyue Lu. I am so glad to have met her through this experience and am grateful for her support, understanding, and love.

Finally, my sincerest thank you is reserved for my mom, Alice Dorman. She has constantly supported me and my decisions, provided me with encouragement when I felt down, and gave me so many gifts. I love you, Mom.

TABLE OF CONTENTS

LIST OF TABLES

LIST OF FIGURES

ABBREVIATIONS AND SYMBOLS

Å	Angstrom
2θ	Scattering Angle for Small Angle X-ray Scattering
a.u.	Arbitrary Units
AgBe	Silver Behenate
AUC	Analytical Ultracentrifugation
B	Blank or Background Scattering
C	Photon Counts in a Given Pixel
CAMD	The Center for Advanced Microstructures and Devices
CSV	Comma-Separated Values
D	Dark Count
DAB-Am	Polypropylenimine Dotriacontaamine Dendrimer
D_{app}	Apparent Diffusion
DCM	Double Crystal Monochromator
DLS	Dynamic Light Scattering
D_{m}	Mutual Diffusion
DOPC	1,2-Dioleoyl-sn-Glycerol-3-Phosphocholine
D_{s}	Self Diffusion
d-spacing	Space Between Layers or Atoms
E	Excess Scattering
EDS	Energy Dispersive X-ray Spectroscopy
FCCC	Fox Chase Cancer Center in Philadelphia, PA

GB	Gigabyte
GPC-MALS	Gel Permeation Chromatography—Multi-Angle Light Scattering
F	Flux of X-rays
He-Ne laser	Helium Neon Laser
HexRu	Hexagonal Terpyridine-Ruthenium Macrocyclic Complexes
HPC	Hydroxypropyl Cellulose
I (a.u.)	Intensity (arbitrary units)
IC	Ionization Chamber
I_t	Intensity at Time t
LNLS	Laboratório Nacional de Luz Síncrotron
LUV	Large Unilamellar Vesicle (>50 nm)
MLV	Multilamellar Vesicle
mM	Millimolar
mT	MilliTorr
M_w	Molecular Weight
nm	Nanometer
P	Parasitic Scattering or Stray Light
PAMAM(G#)	Poly(amidoamine) Dendrimer (Generation 1, 2, etc.)
PBS	Phosphate Buffer Solution
PMT	Photomultiplier Tube

q	The Magnitude of Scattered Light in Inverse Space
RAM	Random-access Memory
RBF	Round Bottom Flask
RC	Ring Current
R_g	Radius of Gyration
RGD	Rayleigh-Gans-Debye Form Factor Equation
R_h	Hydrodynamic Radius
SANS	Small Angle Neutron Scattering
SAXS	Small Angle X-ray Scattering
SLS	Static Light Scattering
SOP	Standard Operating Procedure
SSRL	Stanford Synchrotron Radiation Laboratory
SUV	Small Unilamellar Vesicle (<50 nm)
T	Transmittance
t	Acquisition Time or Thickness of Bilayer
TC	Thermocouple
ULV	Unilamellar Vesicle
USAXS	Ultra Small Angle X-ray Scattering
WAXS	Wide Angle X-ray Scattering
wt%	Weight Percent
XRD	X-ray Diffraction
X	Distance Measurement i.e. Path Length

X_{SD}	Distance Between Sample and Detector
Γ	First Cumulant
θ	Theta, Bragg Angle
λ	Wavelength of Light Source
τ	Lag Time of Autocorrelation Function

ABSTRACT

Lipids are fundamental to all life forms, a key component of cell walls, and essential to proper respiratory function. They are amphiphilic molecules and readily form bilayers. Dendrimers are designer molecules that can be tailored to provide a variety of endgroup moieties, sizes, and charges. The interaction of liposomes and dendrimers can provide information on how medicine interacts with cells and an array of unique structures can be imagined from their assembly into superstructures. Polypropylenimine tetraamine (DAB-Am) and 1-directional arborol dendrimers have been studied in different molar concentrations with 1,2-dioleoyl-sn-glycero-3-phosphocholine (DOPC) bilayers. One-directional arborols are amphiphilic dendrimers with a hydrophilic head group composed of 9 hydroxyl groups and a short alkyl chain for the hydrophobic tail while DAB-Am is a uniform, hydrophilic dendrimer.

Designing, building, and repairing equipment added instrumentation to Louisiana State University's research infrastructure and provided capabilities to perform experiments without traveling to distant laboratories. Small angle X-ray scattering (SAXS) was installed at the Center for Advanced Microstructures and Devices (CAMD) in 2002 and has begun to produce useful information about the size and structure of molecules. Its versatility and availability makes it a powerful tool for researchers and the user base is growing. The Balzers BAF 400 Freeze Etching equipment, or FF, was reintroduced after about 10 years of inactivity and, if properly maintained, will provide scientists the ability to explore samples *in situ* for years to come.

These techniques have been used to study dendrimers' interactions with lipid bilayers. The liposome decreases in size upon the addition of 1 × 10^{-6} moles per liter of dendrimer or less. As the dendrimer concentration increases, the lipid bilayer increases until it is no longer visible in SAXS spectra. FF-TEM shows the formation of large aggregates at high dendrimer concentration, 5 × 10^{-6} moles per liter.

CHAPTER 1 INTRODUCTION

1.1 Introduction

Lipids constitute a large class of molecules with a hydrophilic headgroup and twin non-polar lipophilic tails. Their amphiphilic nature and shape causes lipids to assemble into planar monolayers, bilayers or multilayers. A bilayer of mixed lipids provides the protective coating for all living cells. Spherical vesicles of almost uniform size, i.e. artificial cells, are easily prepared from pure lipids and are known to encapsulate a wide variety of molecules.[1] The net charge on the vesicle can be positive, negative, or neutral, depending on the choice of lipids and additives such as stearylamine. The bilayer may be fluid or gel-like, according to the temperature. Figure 1-1 shows the structure of a phosphocholine lipid, 1,2-dioleoyl-*sn*-glycero-3-phosphocholine or DOPC.

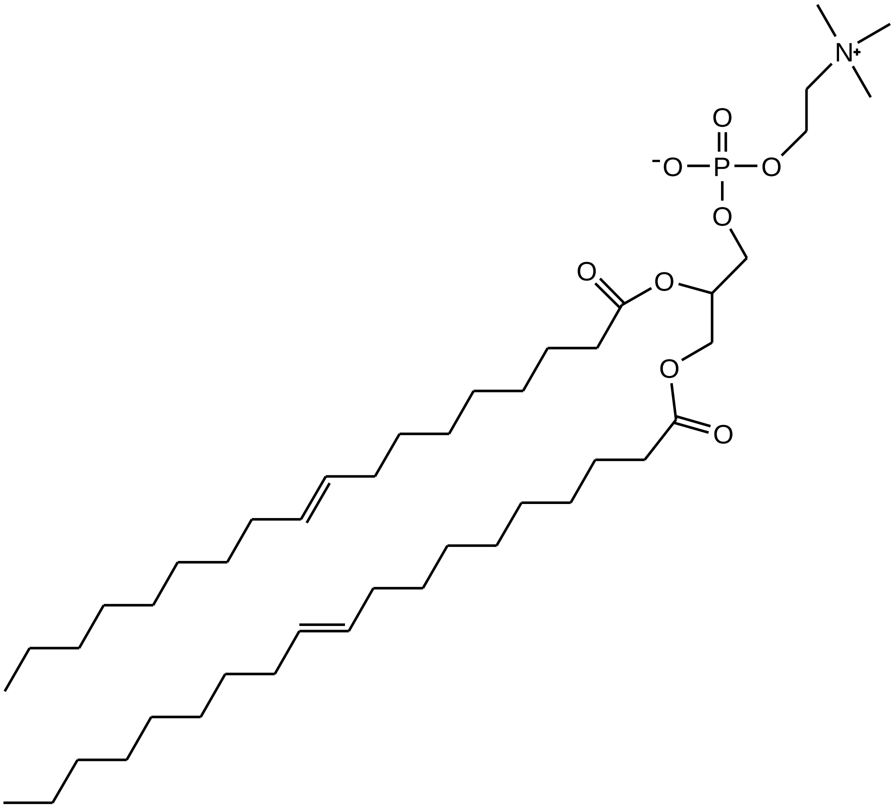

Figure 1-1 A common phosphocholine: 1,2-dioleoyl-sn-glycero-3-phosphocholine, DOPC.

Dendrimers are nearly monodisperse macromolecules that are constructed one generation at a time (see Figure 1-2 below).[2,3] They feature high surface density of functional groups and their molecular size is well defined. In these aspects, dendrimers resemble proteins, and it has even been proposed that they may be able to serve some of the same functions.[4]

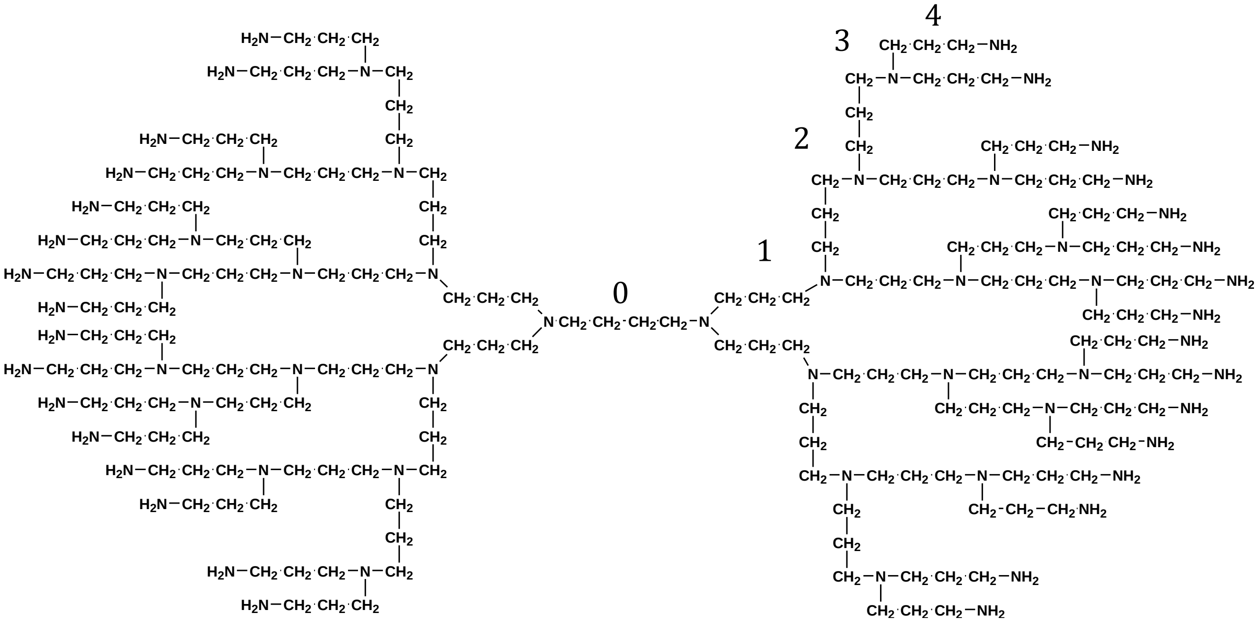

Figure 1-2 Polypropylenimine dotriacontaamine dendrimer, DAB-Am-32, a 4th generation dendrimer.

The interaction between lipids and dendrimers has not attracted the intense scrutiny that interaction between lipids with other biomolecules has.[5-15] Nevertheless, the materials science possibilities afforded by dendrimer interactions with other types of surfaces[14,14,16] and with other molecules[17-20] have not gone unnoticed. There are large experimental and theoretical efforts devoted to fundamental understanding of polyelectrolyte-colloid interactions,[21-26] including dendrimers.[27] The use of lipid superstructures for templating a variety of molecules and particles, sometimes followed by covalent binding, is known.[28-30] A frequent objective is to reduce the permeability of lipid vesicles. Other intriguing materials science possibilities stem from the wide variety of lipid superstructures, which ranges from tubules to space-filling networks. Of the several families of dendrimers, the poly(amidoamine)s are the most fully characterized.[31-33] PAMAMs are available with a variety of surfaces, the two most common being amino and carboxyl. The most relevant studies are those involving the interaction of PAMAMs and oppositely charged polymers[18,20] and surfactants.[17,34]

1.2 Background

The interaction of dendrimers with lipid bilayers has been investigated by few groups. Turro *et al.* have begun to characterize the interaction of PAMAM dendrimers through continuous wave (cw) and pulse electron paramagnetic resonance spectroscopy (EPR), TEM and DLS with vesicles, DNA, and micelles.[35-39] This work showed that a protonated dendrimer of generation 4-6 could perturb the bilayer structure of the membrane, but that the integrity of the vesicle was maintained.[39] Other work on anionic vesicles and polycationic dendrimers showed that higher generations of PAMAM, especially G6 and G7, would cause liposomes to leak.[40] It was suggested that the dendrimer caused the membrane to bend resulting in regions of inverse curvature of the vesicle and even fusion of vesicles. A paper by Mecke *et al.* shows that not only can dendrimers disturb a lipid bilayer, but both anionic and cationic G7 dendrimers can cause lipid bilayers to form around them.[41] The “holes” that form in the membrane of lipid bilayer could result as lipids leave the membrane to form a bilayer around the dendrimer. Mecke also finds that higher generations of positively and negatively charged dendrimers can cause charge-neutral lipid membrane disruptions.

The fluorescence study of Caminati *et al*[17]*.* is akin to the proposed research in that amphipathic molecules (surfactants, not lipids) are used, but the main objective is elucidation of the PAMAM structure. Nonetheless, the authors clearly recognized that these interactions were strong enough that the dendrimers could act as templates for the surfactants.

1.3 Motivation

That something interesting will happen when dendrimers and lipid superstructures are mixed is all but guaranteed by these aforementioned works; yet, one cannot predict the outcome under varying conditions. It is clear that the size, shape and charge of the dendrimer play an important role in how it will interact with a lipid membrane. The presence of a very large colloidal component (the vesicle) favors new methods to study the interaction. For example, vesicle suspensions are generally slightly turbid, even without interacting dendrimers. The first step to harnessing the interaction between dendrimers and lipids for the production of new materials is to define methods by which we can learn whether dendrimers are bound, can be encapsulated, or will not interact at all. In a project that treats dendrimers as surrogate proteins and vesicles as miniature molding machines, biophysical characterization techniques seem particularly appropriate. The long-term goal of this research is to reverse the roles where prefabricated lipid superstructures act as templates for the dendrimers.

Liposomal drug delivery systems are being developed by many research groups.[42-45] A drawback is the quick uptake of the liposome from the blood stream by the reticuloendothelial system (RES). Polyethylene glycol is known to prolong the time liposomal drug delivery systems can stay in the body's circulatory system by decreasing its uptake via the RES.[46] The hydroxyl groups on PEG have been theorized as the reason the RES ignores the vesicles and it is postulated that the inclusion of hydroxyl groups from other molecules could also bypass RES uptake. One-directional arborol dendrimers could be a way to introduce hydroxyl groups along the surface of the liposome. Work with 1-directional arborols has reported on the surface activity of these molecules.[47] This work begins to study how these novel surfactants, with a PEO-like ability to coat a lipid system with a hydrophilic moiety, might interact with lipids.

1.4 Dissertation Synopsis

This dissertation will cover all research efforts including some that may seem outside of the scope of the title. Chapters 2 and 3 discuss equipment built and repaired for small angle X-ray scattering (SAXS) at the Center for Advanced Microstructures and Devices (CAMD) and freeze fracture (FF) equipment for examining real space images of aqueous solutions. Chapter 4 looks at liposome and dendrimer studies performed and where future efforts should be focused. Research performed on semidilute hydroxypropyl cellulose (HPC), macrocyclic complexes of hexagonal terpyridine-ruthenium (HexRu), and work on dextran standards will be reported in the appendices. These projects were crucial in providing a solid foundation on the experimentation required to investigate the interactions between liposome and dendrimers.

CHAPTER 2 SMALL ANGLE X-RAY SCATTERING BEAMLINE AT THE CENTER FOR ADVANCED MICROSTRUCTURES AND DEVICES

2.1 Introduction

The use of X-rays for scientific evaluation of materials has become prevalent since their documentation by Wilhelm Conrad Röntgen in 1895.[48] Today, X-rays are commonly used in medicinal imaging to identify abnormal tissue and bone fractures in humans and animals alike. Small angle X-ray scattering (SAXS) goes a step further than X-ray photography by observing the X-rays that are scattered by materials. Depending on the experimental parameters, scientists can obtain the atom structure of crystals in the case of crystallography or size, shape, and structure information from molecules in a sample by observing the scattered X-rays using SAXS.

SAXS installations are of two main categories: laboratory based X-ray generators such as sealed tubes and rotating anodes and synchrotron sources producing hard X-rays. Seven synchrotron facilities are located in the USA with 14 SAXS beamlines among them. Information on X-ray facilities worldwide can be found at www.lightsources.org.[49] Synchrotrons produce a broad spectrum of radiation ranging from X-rays to IR. A monochromator is used to select the desired radiation energy for experimentation. Rigaku is leading laboratory based X-ray sources with their microfocus rotating anode generators (www.rigaku.com).[50] These generators offer X-ray flux that exceeds some second generation synchrotron sources at $1.6x10^{11}$ X-rays/mm^2/sec.

The J. Bennett Johnston Sr. Center for Advanced Microstructures and Devices (CAMD) has installed an X-ray beamline (6a) dedicated to small angle X-ray scattering spectroscopy (SAXS). The beamline is equipped with an LNLS (Laboratorio Nacional de

Luz Synchroton, Brazil) double crystal monochromator (DCM) with a practical energy range of 3 keV to 14 keV and is computer interfaced and controlled. The SAXS endstation is equipped with a Gabriel type, 2-dimensional, multiwire, position sensitive detector[51-53] from Molecular Metrology, Inc (now Rigaku Corporation).

CAMD is a first generation synchrotron source that provides IR, UV and X-rays to the Deep South. The facility is not limited to its name sake microfabrication projects; rather, it has grown to include 6 X-ray beamlines including SAXS. Users proximal to the LSU campus can prepare samples in their own labs but, like users of national facilities, are not required to design or maintain the equipment.

The SAXS endstation was installed at CAMD in fall 2002. Key features include a 2-D detector, large sample chamber that can accommodate a variety of sample types and even experiments positioned in the X-ray beam path, and a tunable, fixed output monochromator allowing any wavelength between 4.13 to 0.89 Å to be selected. Anomalous SAXS measurements can be made since the monochromator is tunable so samples may be investigated at differing X-ray wavelengths; for example, above and below the X-ray absorptions edges of the material of interest.

2.2 Monochromator Hutch and Shutter Controls

The SAXS beamline consists of two hutches: one for the monochromator and the other housing the SAXS endstation. The first contains the monochromator, shutters, pumps, and a beryllium window that reduces the ultra high vacuum of the synchrotron storage ring to a lower vacuum. X-rays are selected from a broad spectrum of radiation obtained from the bending magnet of the synchrotron storage ring with a double crystal monochromator (DCM) from LNLS. The DCM has a fixed X-ray output, which makes it preferable to other energy selection devices. One drawback to a fixed output monochromator is a reduction of potential flux; however, it allows users to select X-ray energies ranging from approximately 3 to 14 keV without changing the endstation's configuration. This corresponds to wavelengths of 4.13 to 0.89 Å, respectively. The monochromator has a Newport Motion Controller / Driver Model XPS that moves the crystals in order to change the energy range desired. Three different crystals can be used in this monochromator but currently a pair of silicon (111) and germanium (220) crystals are installed. Only one set of crystals is used at a time with the latter ones being used most often. The Ge(220) crystals are better for the current angle and energy range being used. They offer slightly less resolution but higher flux.

X-rays are absorbed as they pass through a material and generate ion pairs. The attenuation law, Equation 1, expresses how the X-ray intensity before absorption (I_0) is affected as they travel through a material with a linear absorption coefficient (μ), and a thickness (X).[54,55]

$$I = I_0 e^{-\mu X}$$

Equation 1

The ionization chamber (IC) consists of two plates under a supplied current and is used to collect the ion pairs created by a gas absorbing the X-ray's energy. Equation 2 uses the current measured by the IC in amps, N_{IC}, to determine the initial flux of X-rays in photons per second. The mass attenuation coefficient, μ/ρ, can be obtained from NIST tables for many common substances.[56] W is the average energy required to produce an ion pair and is 33.97 $J \cdot C^{-1}$ for dry air.[57,58] The electric charge, Q, is 1.602×10^{-19} C and E is the energy of the X-rays. Therefore, the flux of X-ray light leaving the monochromator at 8 keV (or a wavelength of 1.55 Å) is estimated at 7 x 10^9 photons·sec^{-1} for the Ge(220) crystals using an Advanced Design Consulting USA, Inc. Long Ion Chamber (Style 105-0000-2) and Equation 2.

$$I_0 = N_{\mathrm{IC}}\left(\frac{1}{\left[1 - e^{-\left(\frac{\mu}{\rho}\right)\rho X}\right]}\right)\left(\frac{W}{E}\right)\left(\frac{1}{Q}\right)$$

Equation 2

The amount of X-rays illuminating the sample changes throughout the day as the ring current (RC) in the storage ring decays and must be replenished. The complex decay of the flux at the sample makes it difficult to subtract spectra obtained from the beamline especially if long acquisition times are required. Figure 2-2 shows the RC decay and the RC / IC vs. time for the morning and afternoon injection of electrons into the storage ring. The IC is located inside the SAXS endstation hutch where the monochromatic X-rays enter just downstream of the monochromator. An initial maximum of the RC / IC vs. time trace is due to the crystals heating up and reaching thermal equilibrium after being illuminated with radiation from the storage ring. A second maximum or “sweet spot” occurs after the RC decays to between 115 and 140 mA. This is best explained by thermal fluctuations that occur in the crystals as the initial beam intensity obtained from the bending magnet decreases as a function of RC decay. Some DCMs overcome this by incorporating a water chiller to cool the crystals.

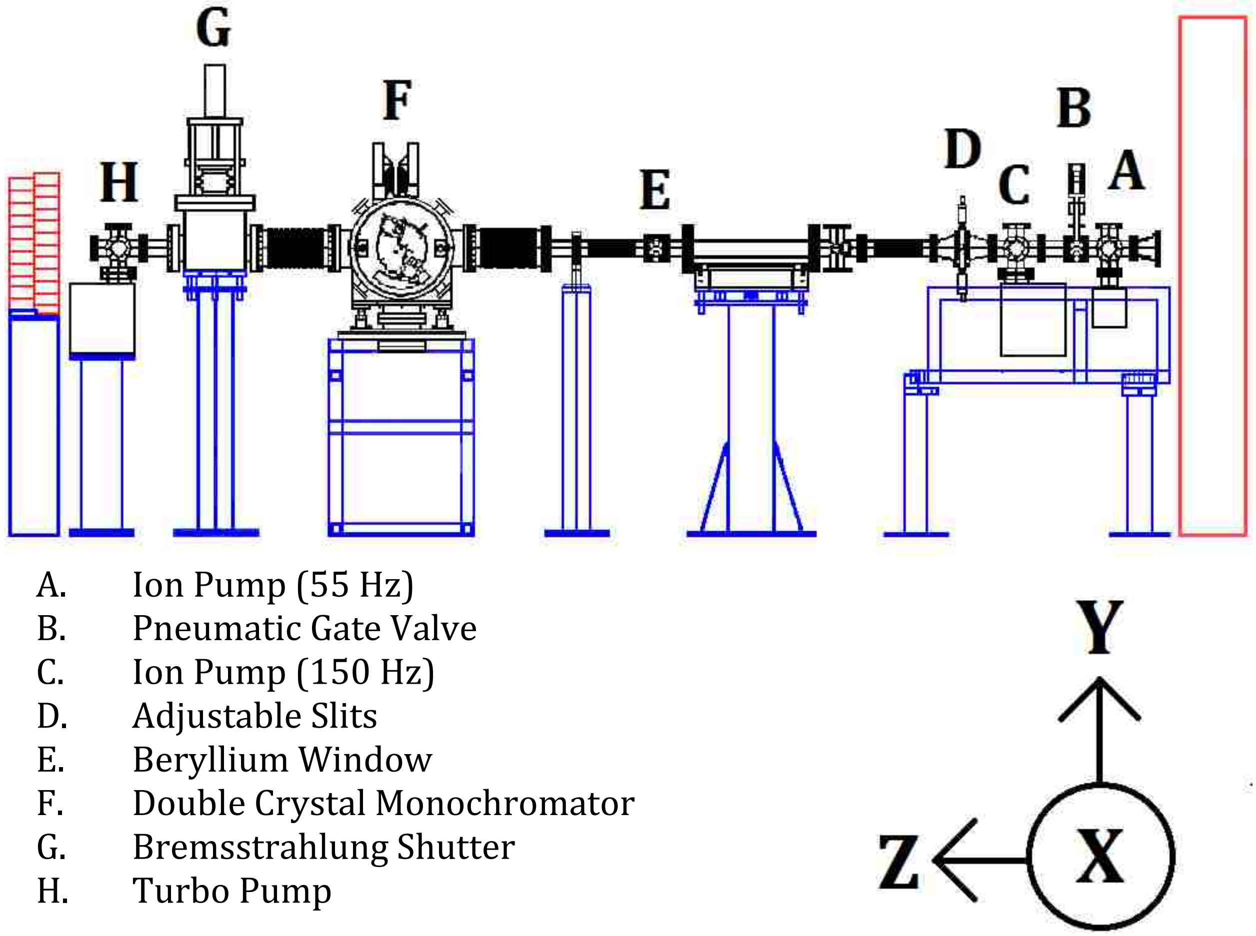

A. Ion Pump (55 Hz)
B. Pneumatic Gate Valve
C. Ion Pump (150 Hz)
D. Adjustable Slits
E. Beryllium Window
F. Double Crystal Monochromator
G. Bremsstrahlung Shutter
H. Turbo Pump

Figure 2-1 Schematic of the monochromator hutch at CAMD adapted from CAMD's *Rose Report*.[59] The electromagnetic radiation from the storage ring travels in the Z direction from right to left and the desired X-ray energy is isolated by the monochromator (F).

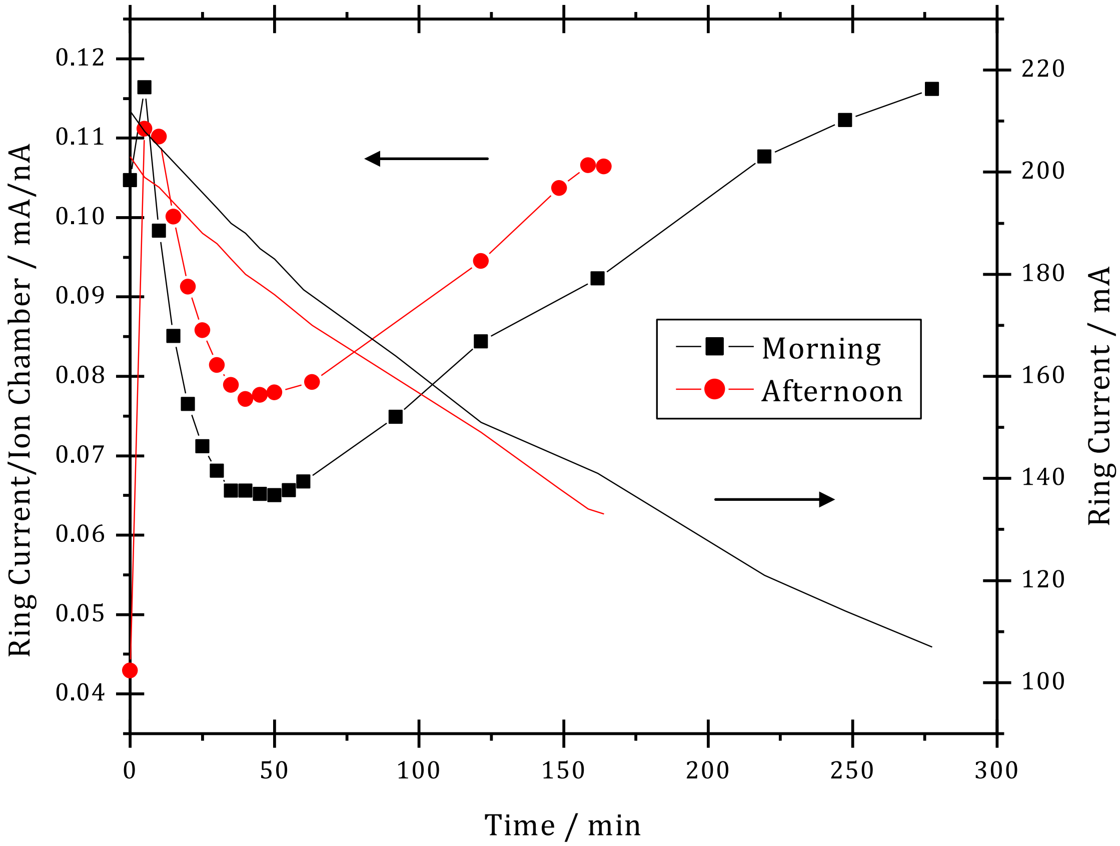

Figure 2-2 The current in the storage ring vs. X-ray flux exiting the monochromator. The solid curves trace the storage ring current during the morning (black) and afternoon (red) injection cycle.

2.3 User Endstation

X-rays from the monochromator enter a second hutch where the SAXS endstation resides. A small air gap between the monochromator hutch and SAXS equipment can be adjusted to allow for the insertion of components such as ion chambers for direct monitoring of flux from the monochromator. Each side is under vacuum and has a Kapton® window, a polyimide film from DuPont™, to minimize absorption while maintaining the vacuum required. Three pinholes prior to the sample chamber are for selecting the beam size that will be used to irradiate the sample and remove most of the parasitic scattering that results from the diffraction of the X-rays off the pinholes. Each pinhole has an x- and y-axis open loop stepper motor for remote (outside of the hutch) positioning to ±2 μm. The available pinhole sizes are 200, 400 and 800 μm as well as some empty pinhole mounts. The pinholes are interchangeable and can be mounted reliably by magnets that line up the pinholes on the motor mounts. In the current configuration, pinholes 1 and 2 are 400 μm in diameter and 160 cm apart while the 3rd one is 800 μm and 38 cm after the 2nd. Samples ran prior to 2009 used a 200, 400, 800 μm arrangement. The third pinhole's purpose is to "clean up" the X-ray beam defined by the first two and reducing parasitic scattering. Perhaps a smaller 3rd pinhole of 600 μm would reduce the parasitic scattering observed around the beamstop enough to see larger details of the sample. The flux of X-rays at the sample (after the pinholes) is estimated at 2.17×10^{7} photons·sec^{-1}.

The aluminum sample chamber features a sample arm hanging from the top about 8 cm from the 3rd pinhole. The arm provides space for multiple samples to be placed simultaneously and two motors control its movement for positioning the samples in the X-ray beam in the x and y direction. The entire sample arm can be swung to adjust the pitch of the arm in the sample chamber. Depending on the sample type and container, they are inserted in the beam path by holders that attach to the sample arm including a capillary holder. A hot stage can also be added for thermal studies.

Figure 2-3 Picture of the SAXS endstation. The blue box on the left is the detector. The pinholes are obscured by the black sample chamber and grazing incidence-small angle x-ray scattering “coffin” in the background on the right side of the picture.

2.3.1 Detector

A 2-dimensional Gabriel type gas-filled wire detector[51] with a resolution of 200 -250 µm—measured at full width half maximum (FWHM) at 8 keV—is used to collect the scattered X-rays. The detector has a 200 mm diameter active area in a 1024 x 1024 square. A 3 mm beamstop in front of the detector prevents non-scattered X-rays from striking the detector and has a photodiode mounted on it for determining the transmitted intensity. Foils of various thicknesses can be installed to control how much X-ray light reaches the photodiode. The beamstop is controlled by two stepper motors so it can be positioned to block the direct X-ray beam.

The detector requires a small electronics rack that includes an ORTEC® Model 660 dual 5-kV detector bias supply, 2 ORTEC® Model 566 time-to-amplitude converters, 2

ORTEC® Model 416A gate and delay generators, and 2 FAST ComTec Communication Technology GmbH 7070 ADC Wilkinson type analog-to-digital converters in order to process the scattered X-rays detected and display them. The detector uses a FAST ComTec MPA-3 dual parameter multichannel analyzer (MPA-3 Server Model MPA-3DP Serial # 266) to interface with the computer.

A Phosphor Imager SI by Molecular Dynamics (Model No. 475 and Serial No. 75125) is an image plate reader used for wide angle X-ray scattering (WAXS) studies. The image plate is mounted in the back of the sample chamber. One of the image plates has been modified by drilling a hole in the center to allow for simultaneous SAXS and WAXS measurements.

An X-Ray Eye by Photonic Science Ltd. is available for alignment and set up. The X-ray eye is an X-ray sensitive video camera with a 2-d real time display of the beam. A variable gain controller enables the X-ray eye to detect X-rays at levels lower than are possible with a fluorescent screen.

2.3.2 Vacuum

The SAXS endstation's flight path is placed under vacuum to run experiments. The vacuum is maintained by a Boc Edwards M2E40 two stage rotary vane oil vacuum pump capable of pressures as low as 1×10^{-3} mbar (7.7×10^{-4} Torr). A copper manifold was made with residential copper pipe, some ball valves (both purchased from Home Depot), and stainless steel vacuum flanges (ISO NW40 from MDC Vacuum Products, LLC) to connect the pump to the beamline. The manifold isolates the pump from the beamline so any vibration from the pump is not transferred to the beamline. It is important that the sample stays stationary and the X-ray beam path remains stable.

Two Edwards active Pirani vacuum gauges (APG100-XM, NW25) with a measurement range from atmosphere to 10^{-3} mbar, monitor the status of the vacuum within ± 15% at <100 mbar. A pressure gauge through one of the ports on the sample chamber is used to monitor the vacuum of the endstation, while the second pressure gauge is located at the vacuum pump. A pressure of less than 0.55 mbar (~ 0.4 Torr) is typically observed at the sample. The pressure at the vacuum pump is much less than 0.2 mbar (~ 0.1 Torr), which suggested that the endstation is not air tight.

2.3.3 Endstation Computers and Software

Three computers are used during a SAXS experiment. One controls the monochromator, and the other two are used to collect and work up the data. The monitors for the computers have auxiliary connections that allows for cameras and the X-ray eye to be connected to them. A Dell Precision 650 computer with Intel® Xeon™ 3.2 GHz CPU, 2 GB of RAM, and NVIDIA Quadro NVS 8 × AGP video card is the primary computer for the endstation. A PCI card from FAST ComTec is used to interface the detector with the computer. All the motors for the endstation and the detector controls are accessed through a LabView 6.1 program, SAXS.vi, supplied by Molecular Metrology. The LabView program runs FAST ComTec MPant subroutines for displaying the data collected by the detector. The Hewlett-Packard Pavilion Media Center m8100n desktop computer is used to work up the data and can record video as well. It has an AMD Athlon™ 64 X2 5600+, 2.80 GHz Dual-

Core processor, with 3 GB of RAM and a NVIDIA GeForce 6150SE nForce 430 integrated graphics accelerator chipset.

Once the data have been saved, they are transferred to the HP computer where several programs are used to evaluate the MPant data files. SAXSGui by Rigaku is used to convert the 2-D data from the detector to 1-D data of I vs. q. Then the file is converted to a comma-separated values (CSV) file that can be imported and further manipulated by Excel, Irena v2.36 (a macro package for Wavemetrics Igor Pro to evaluate scattering data distributed free of charge by the Advanced Photon Source, Argonne, IL),[60] or any other program a user would like to use.

The Molecular Dynamics image plate reader is also connected to the HP computer through a SCSI interface and the software for scanning the plate and extracting the data is installed. FIT2D v12.012 (copyright A. P. Hammersley/European Synchrotron Radiation Facility, 1987-2004) is used to evaluate the 2-D data from the image plate. The program allows for many standard mathematical data manipulation routines and can convert to many common file types i.e. CSV.

2.3.4 Sample Preparation

The sample chamber and accessories provide many possibilities for inserting material in the X-ray beam path. Special glass capillaries from Charles Supper Company, Inc. are favored for liquid samples while powder samples are often sandwiched between pieces of Kapton® tape. The glass capillaries can be sealed by melting the glass in the flame of a candle and/or sealing with hot candle wax. If the sample cannot be prepared in such a way to allow for it to be placed under vacuum, vacuum tight Kapton® windows can be added to the front and rear of the aluminum sample chamber to maintain the vacuum before and after the sample. This has the disadvantage of introducing an air gap of about a 30 cm that will attenuate and scatter X-rays. Unconventional experiments can be run in this manner such as flame experiments perform by Beaucage et al in 2008 to investigate the dynamics of nanoparticle growth in a flame.[61,62]

2.4 Evaluating the Data

Some thought must be given to evaluating the X-rays collected by the detector. It is important to know the sample to detector distance which can be determined using a standard such as silver behenate (AgBe) with a d_{001} = 58.38 Å and Bragg's law below in order to calculate the *q* values. SAXGui will automatically determine the q values from AgBe and the file can be save to use until the sample to detector distance changes.

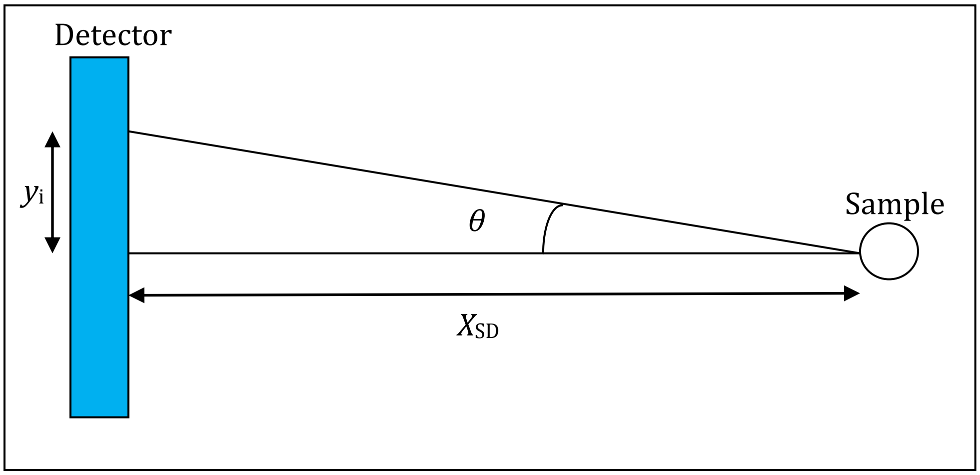

Figure 2-4 Geometry of SAXS endstation used to determine the exact distance between the sample and the detector in order to calculate the *q* space.

$$n\lambda = 2d_{\mathrm{Bragg}}\ \sin\frac{\theta}{2} \approx 2d_{\mathrm{Bragg}}\ \tan\frac{\theta}{2}$$

Equation 3

$$\theta = \tan^{-1}\frac{y_{\mathrm{i}}}{X_{\mathrm{SD}}}$$

Equation 4

The particular method used to work up the data depends on the experimental parameters of each beamline but, generally, the scattering spectra obtained is proportional to the scattering from the sample , solvent, sample holder, stray light and the dark count for the detector.

$$C \sim E + B + P + D$$

Equation 5

C is the photon counts in a given pixel, E is the excess scattering, B is the background scattering, P is the parasitic scattering, and D is the dark count. For the background, E is zero to indicate the absence of sample. Flux (F), acquisition time (t), and transmission (T) must also be taken into account, so the new equation for the sample is:

$$C_{\mathrm{S}} = t_{\mathrm{S}}T_{\mathrm{S}}F_{\mathrm{S}}(E + B + P) + t_{\mathrm{S}}D$$

Equation 6

The equation for the solvent and sample holder or background is:

$$C_{\mathrm{B}} = t_{\mathrm{B}}T_{\mathrm{B}}F_{\mathrm{B}}(0 + B + P) + t_{\mathrm{B}}D$$

Equation 7

The flux is the initial X-ray intensity, I_0, integrated over time, τ, and the transmission is similar to Equation 1:

$$T = \frac{I_t}{I_0} = e^{-\mu X}$$

Equation 8

To obtain the corrected C for the sample and background, the dark count should be subtracted from both sides of the equation and divide by *t*, *T*, and *F* to get:

$$C_{\mathrm{S,corrected}} = \frac{C_S - t_{\mathrm{S}} D}{t_{\mathrm{S}} T_{\mathrm{S}} F_{\mathrm{S}}} = E + B + P$$

Equation 9

and

$$C_{\mathrm{B,corrected}} = \frac{C_B - t_{\mathrm{B}} D}{t_B T_{\mathrm{B}} F_{\mathrm{B}}} = B + P$$

Equation 10

SAXSGui automatically normalizes the data to counts per pixel per sec so Equation 9 and Equation 10 do not need to be divided by *t*. For SAXS at CAMD, the term *TF* is proportional to the integrated photodiode reading.

$$PD_{\mathrm{int,corrected}} = PD_{\mathrm{int}} - PD_{\mathrm{dark}} = TF$$

Equation 11

E can be obtained by substituting the recorded $\mathrm{PD}_{\mathrm{int,\ corrected}}$ for sample and background into Equation 9 and Equation 10 and subtracting.

There are a variety of ways to introduce errors when obtaining excess scattering. *B*, *P*, and *D* are presumed to be constant in the aforementioned equations. Even small errors in *T*, *F*, *B*, *P*, and *D* can wreak havoc in the resulting intensity plots. This is especially true for weak scatters such as solutions where C_{S} may only be as much as 1% larger than C_{B}.

The consequence of such errors when analyzing spectra often results in noisy data and/or negative *I* values over some of the *q* space.

2.5 Results and Discussion

Silver behenate (AgBe) is a white crystalline silver salt of a 22 carbon carboxylic acid, $AgC_{22}H_{43}O_2$, and is used to calibrate the *q* space of SAXS, X-ray diffraction (XRD),[63-65] and small angle neutron scattering (SANS) instruments.[66,67] It has been shown to be a low- and mid-angle calibration material with (001) spacing of 58.38 Å and 13 evenly spaced reflections.[63,64] SAXSGui allows the user to select 3 points that lie on the first order ring of AgBe and relates the pixels of the detector to the appropriate *q*. The center must be defined so the software will automatically calculate it or allow the user to select one. Once these parameters are obtained, they are used to form an I vs. *q* plot for subsequent spectra manipulations such as background subtraction. For this reason, AgBe was one of the first samples inserted in the X-ray beam path.

The AgBe was purchased from The Gem Dugout (State College, PA), and the powder was placed between 2 layers of Kapton® tape. Early scattering spectra from CAMD did not exhibit the increased flux expected from a synchrotron source. In fact, it was not as good as a rotating anode which should be dimmer though new generators from Rigaku are advertised as synchrotron class X-ray sources. Figure 2-5 and Table 2-1 show the small angle scattering spectra of AgBe from CAMD on different dates and from a rotating anode X-ray generator from Zimei Bu's laboratory at the Fox Chase Cancer Center in Philadelphia,

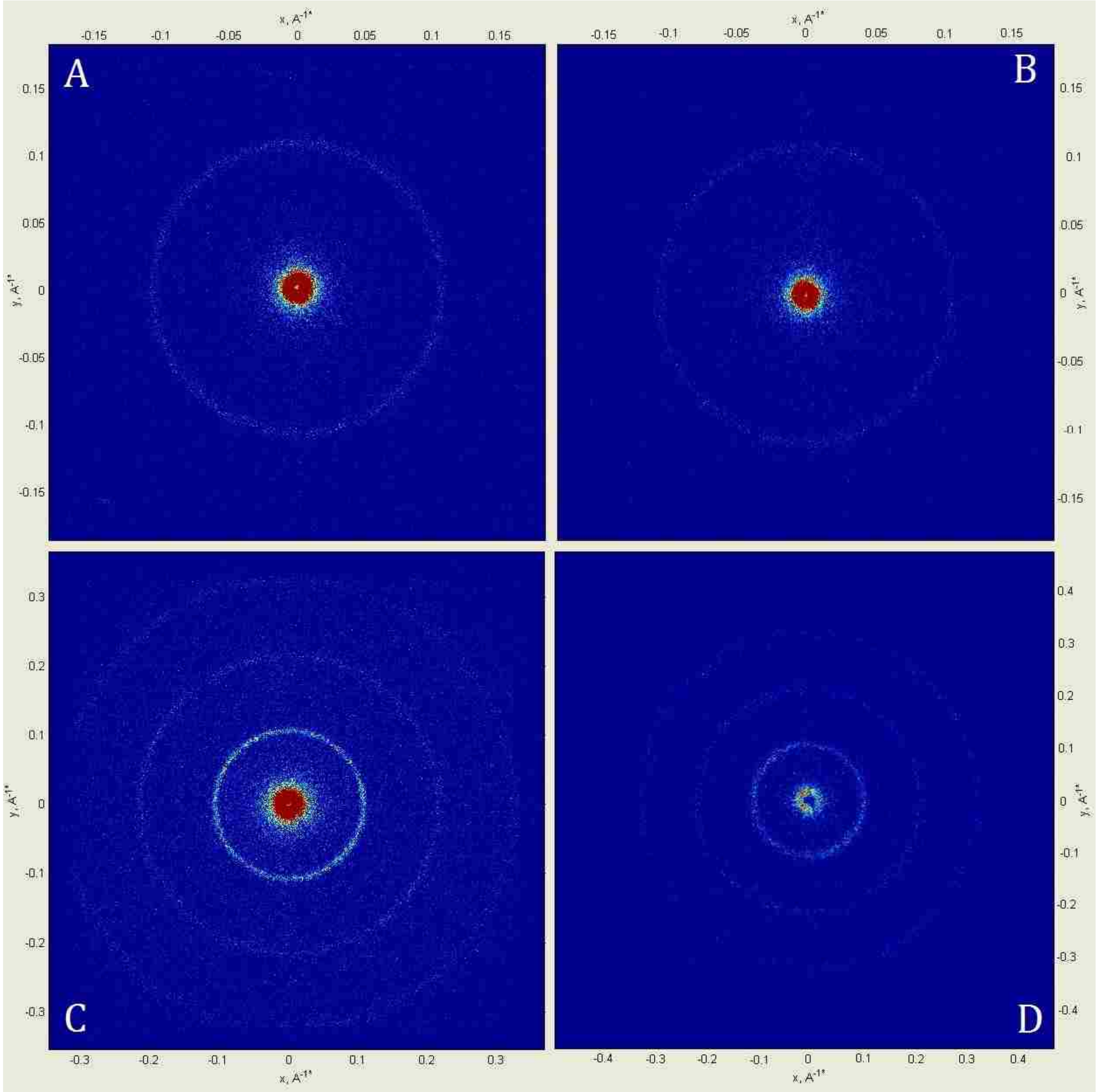

Figure 2-5 Silver behenate scattering spectra at different dates and sample to detector distances. The *q* space along the axes is calculated from AgBe with d_{001} = 58.38 Å. A) AgBe spectra from SAXS at CAMD on Feb. 13, 2003. B) AgBe at CAMD SAXS on Aug. 13, 2009. C) AgBe spectrum from a rotating anode X-ray generator in the lab of Zimei Bu at the Fox Chase Cancer Center. D) AgBe spectra from SAXS at CAMD on July 22, 2008.

PA. Though there are several other factors to consider like sample to detector distance and the sample path length, the data from the Bu is 3 times brighter than the first AgBe spectra obtained at CAMD. Witnesses at the FCCC stated that the rings of AgBe were immediately recognized when the sample was irradiated. This was not originally the case at CAMD SAXS but is today after all the improvements. The AgBe 2009 sample spectra (Figure 2-5 B, Table 2-1) when compared to the 2003 AgBe sample (Figure 2-5 A, Table 2-1) shows almost 10 times more photons scattered, and the ring of AgBe was observed after mere seconds in the 2009 samples as opposed to about a minute in the 2003 sample. Though not quantitative, this supports how the improvements and optimization of the beamline since 2003 have made a difference in the quality of results.

Table 2-1 Comparison of AgBe spectra from SAXS at CAMD's synchrotron and a rotating anode X-ray generator at the Fox Chase Cancer Center in Zimei Bu's laboratory.

AgBe Sample and Date	**Total Counts**	**Time, sec.**	**Counts per sec.**	**Number of Visible Rings**
CAMD Feb. 2003	131965	200	659.8	1 (**Figure 2-5** A)
FCCC Zimei Bu	213759	94.7	2258	3 (**Figure 2-5** C)
CAMD June 2008	252421	93.7	2695	3 (**Figure 2-5** D)
CAMD Aug. 2009	91651	14.3	6408	1 (Figure 2-5 B)

Samples of bovine serum albumin (BSA) have proven the capabilities of SAXS at CAMD. BSA typically forms a small aggregate of 3 BSA molecules and can be used as a size standard. A 6 % sample of BSA by weight was performed in 2007, and it took over 19 minutes to collect approximately 300,000 counts. The counts collect faster around the beamstop due to parasitic scattering. This information is often discarded because the background or solvent cannot be adequately subtracted from the sample. The data in Figure 2-6 show the radial average I vs. q for a 6 weight percent (wt%) BSA sample in a phosphate buffer solution (PBS). The first 4 data points are within the beamstop, and the next 6 points are due to parasitic scattering. The shoulder is an artifact of the background subtraction and should be discarded as well. In Figure 2-7 the erroneous data have been removed, and the high q data are ignored to produce a Guinier plot of the natural log of I vs. q. The R_g of a trimer of BSA is determined from the slope of the linear fit and calculated to be 27.8 ± 3.3 Å. In 2009, a 1% BSA sample was run and shown in Figure 2-8 plotted in Irena, the Igor SAXS macro package from APS. An R_g of 27.9 ± 0.1 Å was obtained automatically using the built in Guinier function provided with Irena. The calculated R_g was similar to the 6% BSA but lower than the literature value of ~30 Å.[68,69]

The functionality of SAXS at CAMD has been explored by several individuals. Some of the data obtained by students at CAMD during a SAXS class (Chem 7780) taught by Professor Russo is used to evaluate the equipment. Cristina Stefanescu used SAXS to investigate collagen fibrils found in chicken tendons from the leg and breast of the bird. This work was compared to results from Rigaku on turkey tendons[70] and suggests that chicken tendon could be used as a calibration material. It is important that the tendon stay moist in order to provide the proper d-spacing. The d-spacing from the different collagen fibrils was similar, differing by approximately half of a percent. The lack of baseline resolution from the CAMD sample is likely due to not subtracting the background.

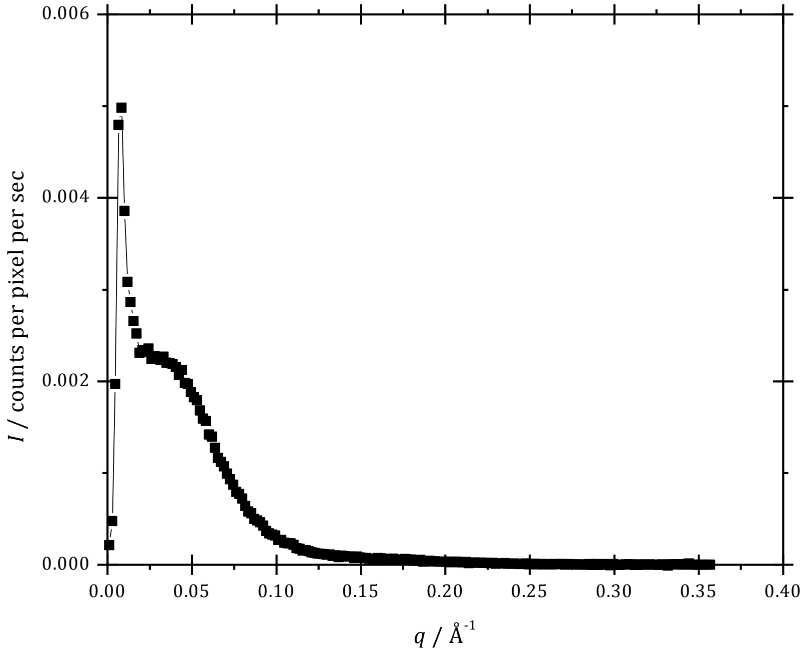

Figure 2-6 SAXS of 6% BSA. The first 4 data points are within the beamstop, and the next 6 points are most likely due to parasitic scattering. The shoulder is an anomaly of the background subtraction and should be disregarded also.

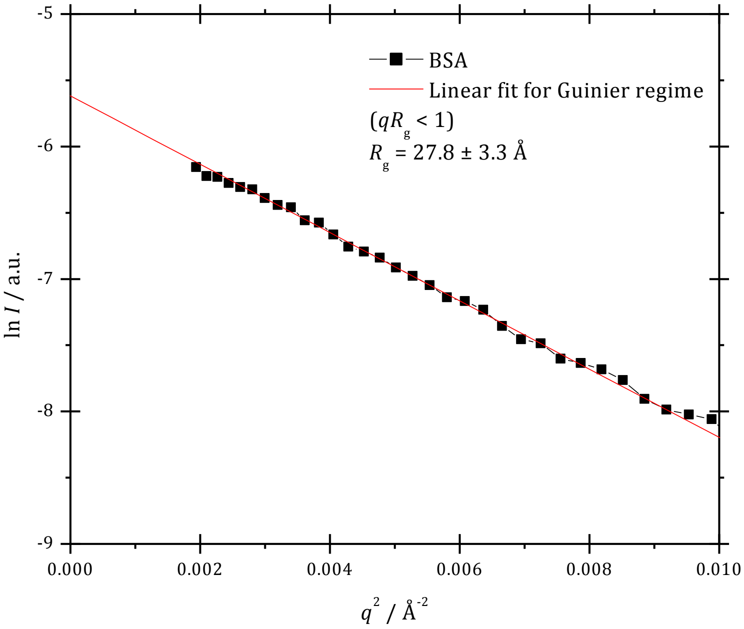

Figure 2-7 Guinier fit of 6 wt% BSA data with a calculated Rg of 27.8 ± 3.3 Å.

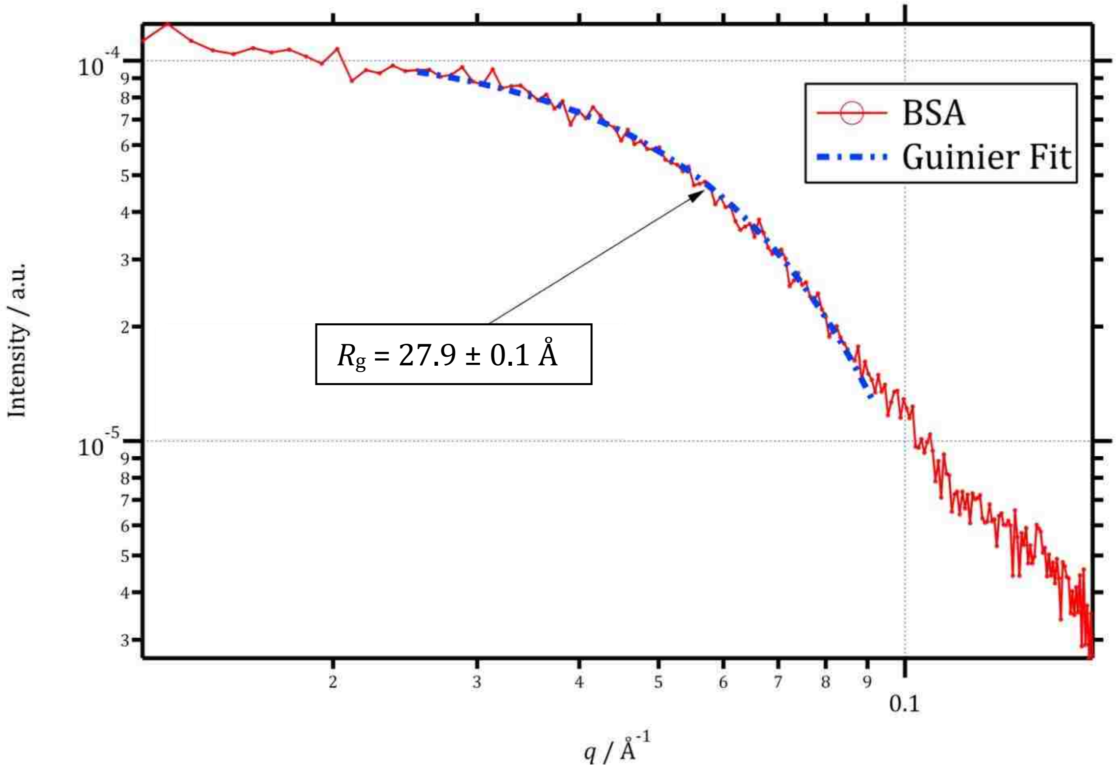

Figure 2-8 Guinier fit of 1 wt% BSA performed automatically by Irena macros for IGOR.

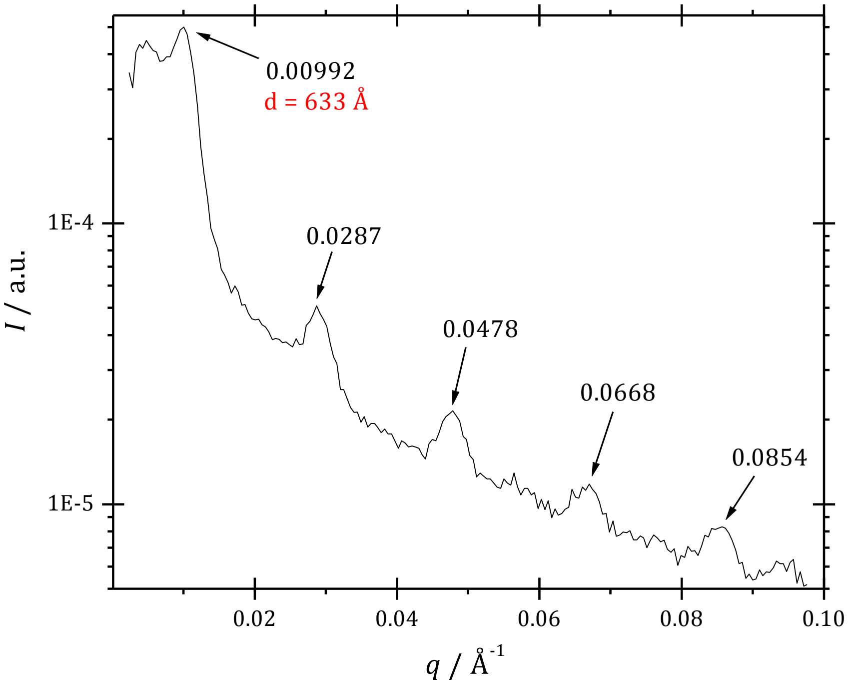

Figure 2-9 The *I* vs. *q* for chicken breast tendon from SAXS at CAMD.

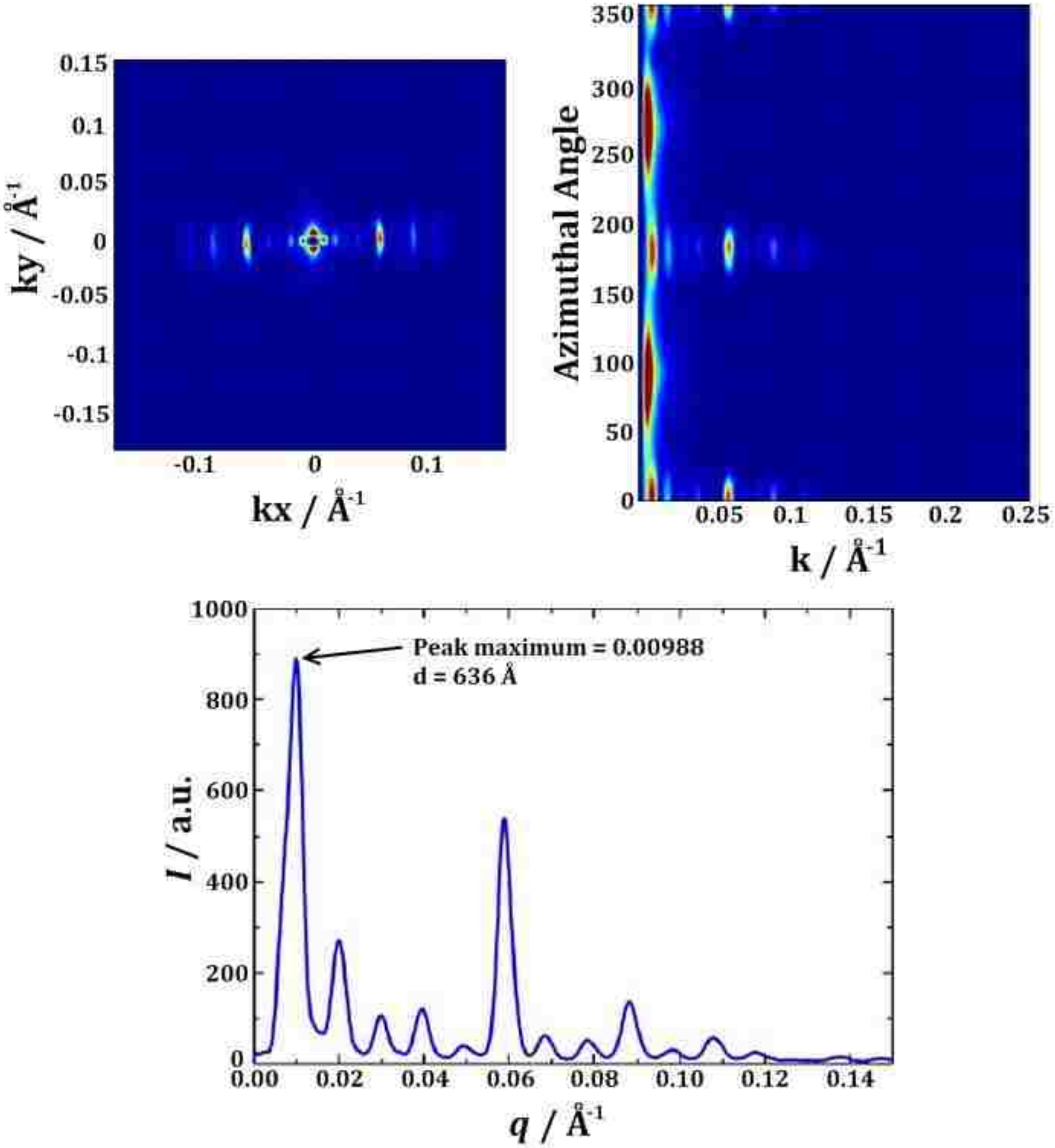

Figure 2-10 SAXS pattern for turkey tendon adapted from Rigaku experiment on a S-MAX3000 standard 2D SAXS system in the Polymer Science and Engineering Department of the University of Massachusetts, Amherst MA.[70]

2.6 SAXS of Hexagonal Terpyridine-Ruthenium Macrocyclic Complexes

Newkome's hexagonal terpyridine-ruthenium macrocyclic complexes (HexRu) have been evaluated before and a cyclic arrangement consisting of six Ruthenium ions complex with the terpyridine structure was projected (Figure 2-12).[71] Using the proposed positions of each atom in the structure and the form factor for SAXS (Equation 12), a theoretical plot for the HexRu complexes can be calculated (the red line on Figure 2-11). SAXS work performed by Jason Campbell at LNLS covering a q range from 0 to 0.3 Å^{-1} is shown overlain on the calculated form factor and shows the lack of enough experimental data to determine if HexRu behaves as expected.

$$P(q) = \frac{\sum_{i=1}^{N} \sum_{j=1}^{N} \frac{f_i f_j \sin qR_{ij}}{qR_{ij}}}{\sum_{i=1}^{N} \sum_{j=1}^{N} f_i f_j}$$

Equation 12[72]

An additional trip to LNLS SAXS was performed to acquire the missing data. Figure 2-13 is the background corrected data plotted with the theoretical P(q) for comparison. The experimental data seems to support the initial theoretical curve; but at q = 0.3 Å^{-1}, the intensities become negative due to the background subtraction. Aggregation dominates and is apparent by the initial downturn in the HexRu intensity marked by a black arrow in Figure 2-13. This is also observed in the previous work (Figure 2-11). Much of the q data is lost when the scattering of the solvent and sample cell (background) is subtracted from the sample. This is a common problem with solution SAXS and may result from errors associated with accurately determining X-ray flux and transmission. The background should not scatter more than the sample; so, in an attempt to correct for this, the intensity data from the HexRu sample is multiplied by an arbitrary factor of 1.2 before the background is subtracted and plotted in Figure 2-14. 1.2 was chosen because it is the smallest number that the data can be multiplied by to force the majority of the HexRu data to be larger than the background intensity values. The resulting curve does not have the same shape as the theoretical, but a small peak in the experimental data (marked by a black arrow) corresponding to a peak in the theoretical curve is interesting. It is not surprising that the experimental data differs from the theoretical calculation. The theoretical curve is the calculated form factor, P(q), from one molecule in the configuration shown in Figure 2-12; therefore, solvent and interparticle interactions are completely ignored. The experimental data suggests large aggregates are forming in solution which is not taken into account by the theoretical structure calculation.

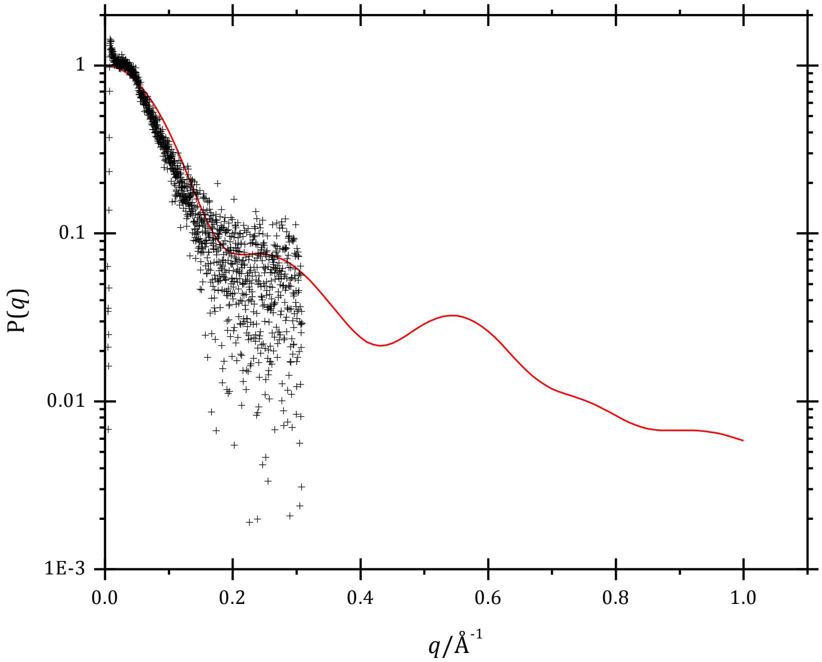

Figure 2-11 LNLS SAXS experiment of di-t-butylphenylalkynyl substituted HexRu complex. The red line represents the P(q) calculated using molecular modeling coordinates.

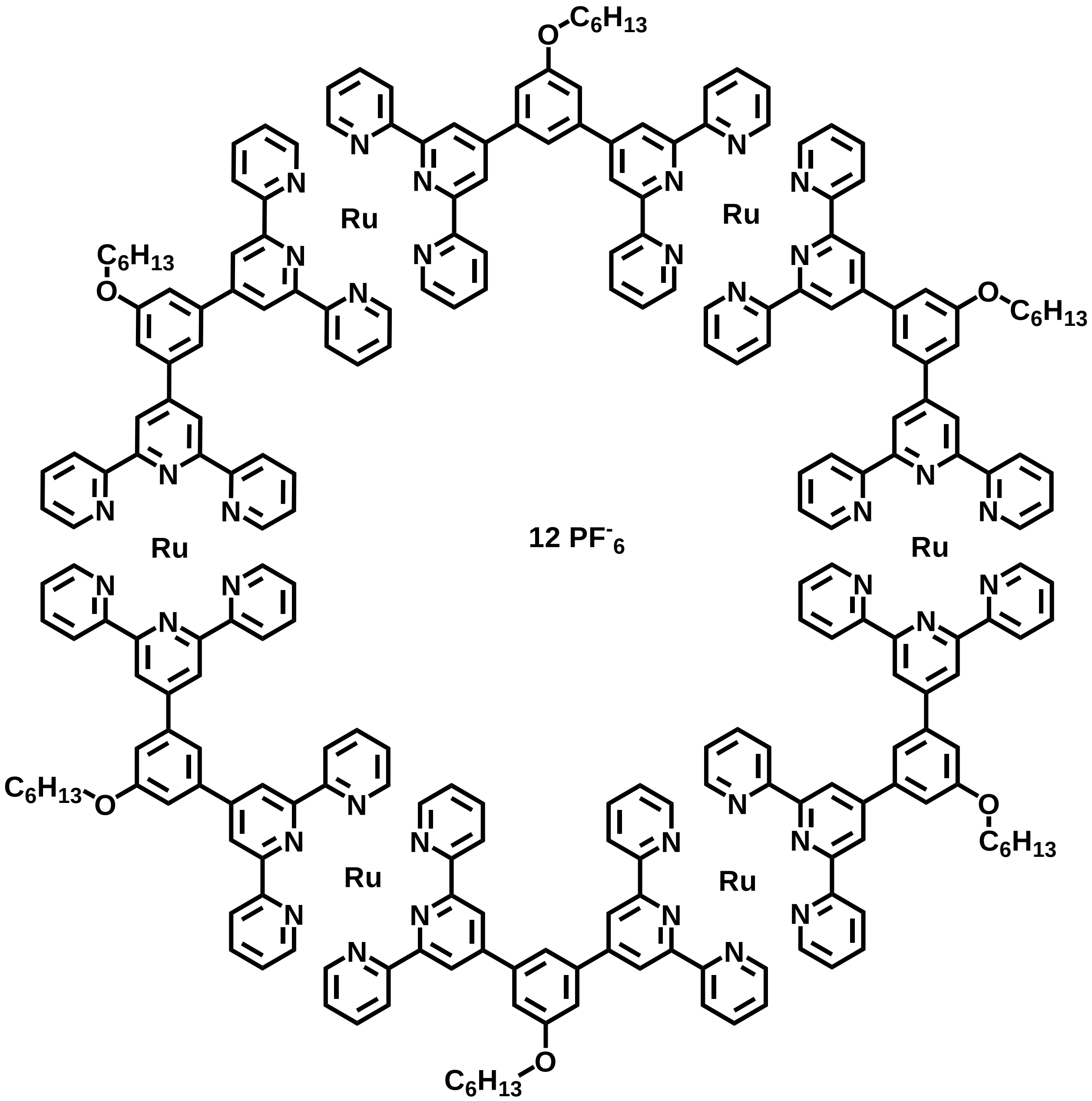

Newkome Lab Notebook No.: wps088

$C_{252}H_{216}F_{72}N_{36}O_6P_{12}Ru_6$

Exact Mass: 6192.77

Mol. Wt.: 6190.64

Best Solvent: Acetonitrile

Figure 2-12 Chemical structure of hexagonal terpyridine-ruthenium macrocyclic compound (HexRu).

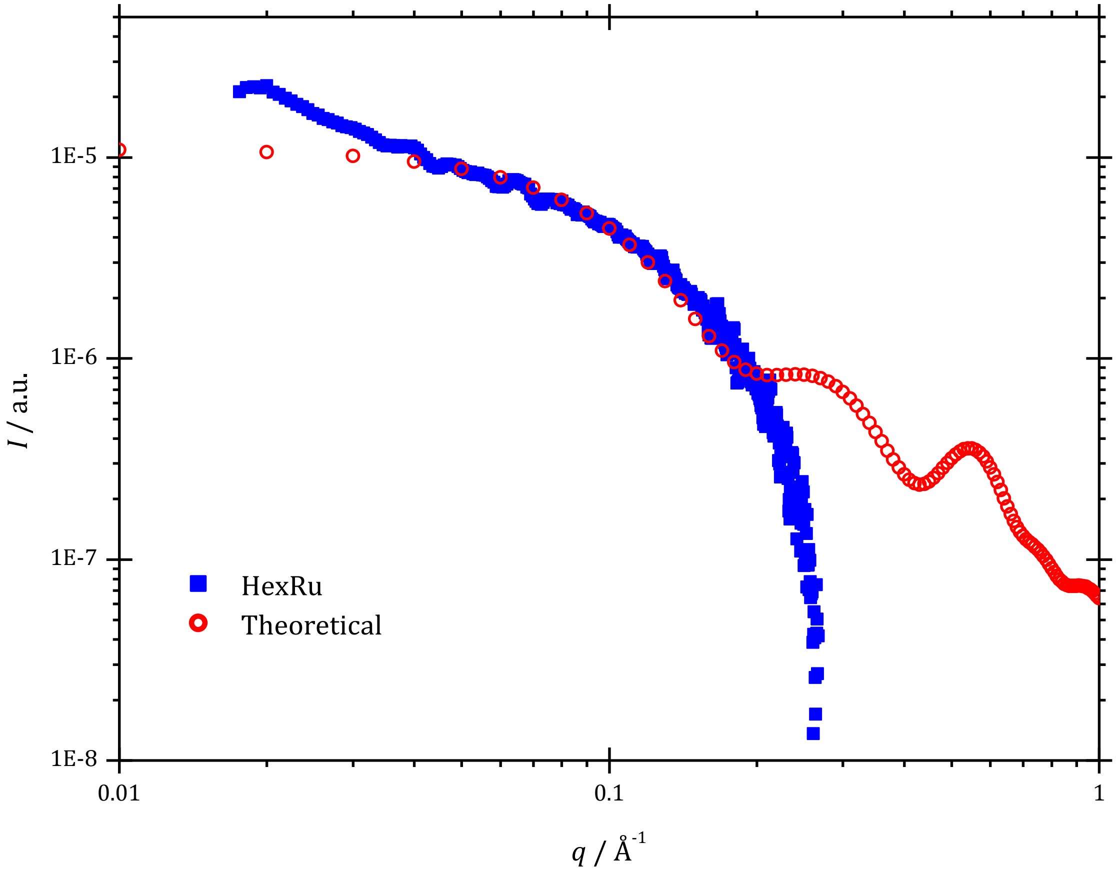

Figure 2-13 10 mg/ml HexRu experimental data from LNLS with calculated P(q). The background subtraction has generated negative values beginning at q = 0.3. The positive portion of the experimental data roughly matches the theoretical spectrum. This may be improved by trying to normalize the background to the sample data before the subtraction.

The HexRu sample has been studied at CAMD with SAXS and WAXS and similar data was obtained (Figure 2-15). The WAXS data has a peak at 1.5 Å^{-1} from the glass capillary sample holder. Ideally, this would be removed by subtracting the background (solvent and capillary) from the sample. Improvements to WAXS should make it easier to perform the required measurement such as an image plate with a hole cut in the center to allow simultaneous SAXS and WAXS data collection and increased stability with the image plate reader. Unfortunately, the true structure of HexRu complexes is still obscured by less than perfect data and the inability to subtract the backgrounds cleanly. The Newkome conjecture is not yet proven in dilute solution by SAXS

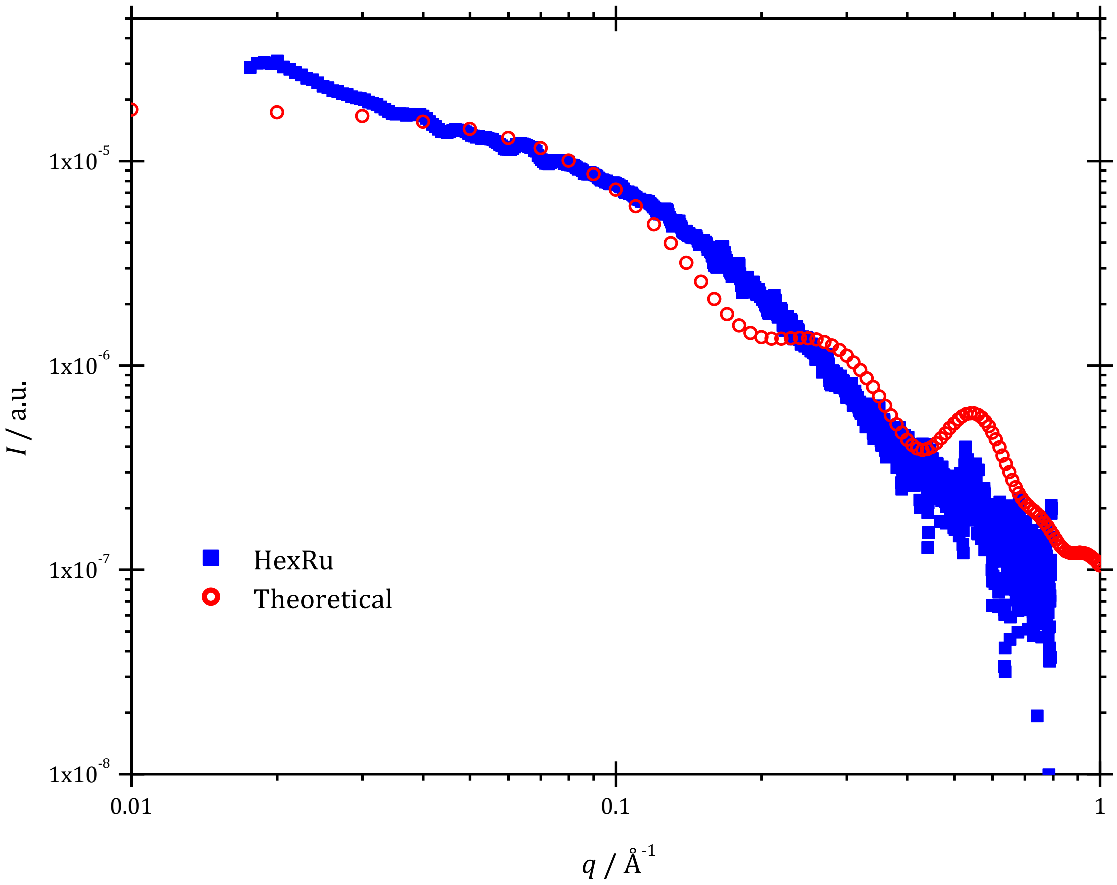

Figure 2-14 The HexRu scattering data has been multiplied by 1.2 before the background is subtracted to force the solution to have higher intensity than the solvent. The theoretical curve does not match in this log-log plot well but a small peak (black arrow) on the experimental data corresponds to a peak in the theoretical.

2.7 Conclusions

SAXS at CAMD has matured to become a powerful tool available to users, now numbering 14. Experiments are showing solution SAXS can be performed effectively, if not quickly, at CAMD. The flux has been an issue in the past, but optimizations over the last 3 years have improved the situation with more on the way, such as mirrors and plates.

Increased flux will result in more scattering but obtaining accurate flux and transmission measurements may be more important. Improved flux and transmission data should reduce the complications that arise from subtracting the solvent from the sample. Software for data reduction is already helping the quality of SAXS results but it is still necessary to arbitrarily guess flux and transmission factors for some samples in order to make C_S be greater than C_B.

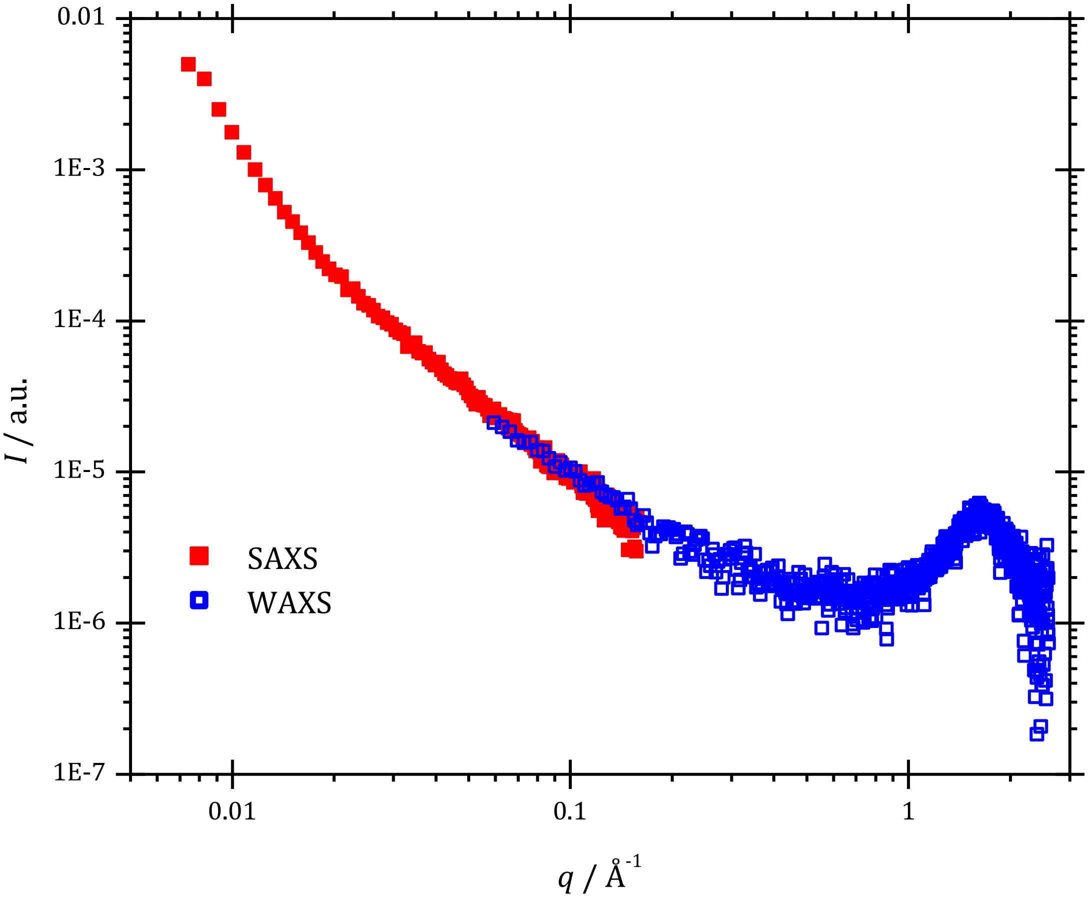

Figure 2-15 SAXS and WAXS data for 10 mg/ml HexRu in acetonitrile. The glass capillary could not be subtracted from the sample and causes a large peak near 1.5 Å^{-1}.

CHAPTER 3 FREEZE FRACTURE: BALZERS BAF 400 AT THE SCHOOL OF VETERINARY MEDICINE

3.1 Introduction

The use of freeze fracture or etching to prepare electron microscopy samples began in the 1950s with Hall.[73] The technique was noticed by cell biologists[74,75] and scientists began improving the procedure; for example, Moor et al in 1961 reported the use of a vacuum evaporator with a precision microtome for fracturing.[76] In 1965, Balzer AG (Liechtenstein) began selling the first commercially available FF equipment modeled after Moor's design.[77] Supporting information on FF was obtained largely from Severs[78] and the manuals supplied with the Balzers BAF 400.

Freeze fracture replication is a useful tool to image samples in a frozen state. The technique provides a way to image samples without staining or removing supporting matrix, i.e. solvent. It is most often done for aqueous systems, but can be performed on other systems as long as the solvent can be rapidly frozen or vitrified. The method employs high vacuum and cryogenic temperatures to vitrify samples in order to fracture along a plane through the sample. The sample can be etched by raising the internal temperature of the vacuum chamber. This process can increase contrast by exposing more sample through the removal of a small amount of the supporting matrix (the frozen solvent). The deposition of a metal such as platinum and a supporting layer of carbon yield a replica that can be viewed in a transmission electron microscope (TEM). The metal is deposited at a 45° angle to create a shadow that will provide the contrast needed to interpret the TEM images. Figure 3-1 shows the cross section of a hypothetical frozen sample to be fractured along the dotted line in A. The result of depositing Pt is depicted in D where the dark areas lack Pt. In the TEM, the areas with the most Pt will block the most electrons so they will appear the darkest and the lighter areas have less Pt, so the TEM images will have white shadows in areas where the Pt is blocked by structures protruding from the fracture surface.

3.2 Balzers BAF 400

The Balzers BAF 400 (Figure 3-2) is, basically, a large vacuum chamber with insertion ports, a microtome blade/knife, and 2 evaporation sources or guns. The vacuum is, perhaps, the most important part of the system. It takes a mechanical or roughing oil pump and a cryo pump to achieve the high vacuum required to use the electron guns. The mechanical pump evacuates air from the vacuum chamber and the 2 interlocks. The interlock system on the left side of the chamber allows for the insertion of the specimen table while the on top grants access to the carbon gun, which requires reloading 3 times more often than the platinum-carbon gun.

A low pressure liquid nitrogen tank (20 psi) is attached to the BAF 400 to cool the knife and stage that holds the samples on the specimen table. The system is vented using the $N_2(l)$ as well. This is preferable to air because it avoids introducing water vapor and other contaminates to the system that will decrease the efficiency of the cryo pump, ultimately resulting in more downtime. A cylinder of $N_2(g)$ regulated at 80 psi is used to open and close the valves associated with the interlock and vacuum system. The valves are controlled by the ALC 101, which will be discussed further in Section 4.2.1.

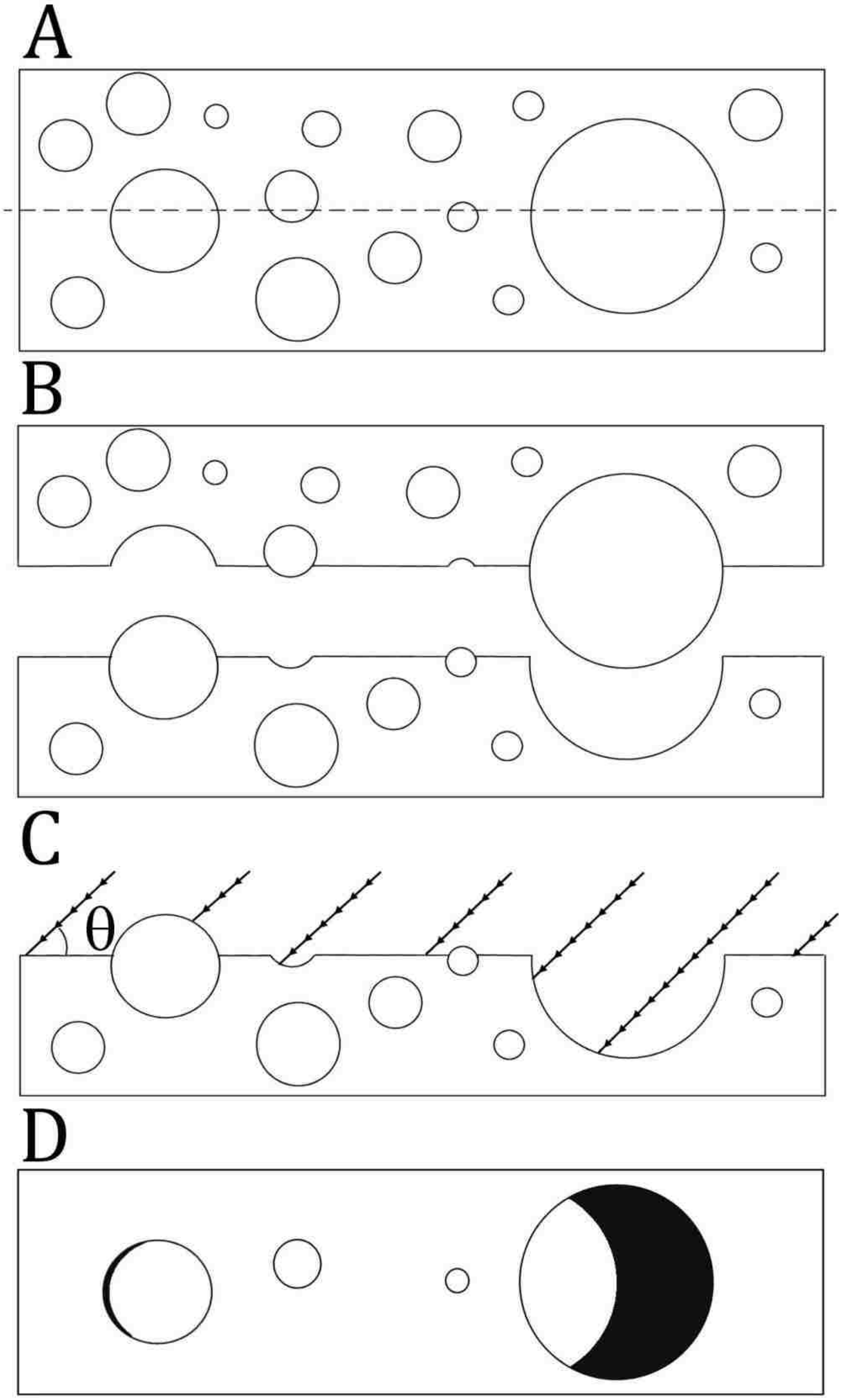

Figure 3-1 Depiction of steps during sample fracture and replication. A) This is the representation of a vitrified sample ready to be fractured. The dashed line represents the fracture plane. B) Possible fracture outcome. C) The platinum is deposited at angle θ most often 45°. D) Resulting replica as viewed in the microscope. The schematic was adapted from Egelhaaf et al.[79]

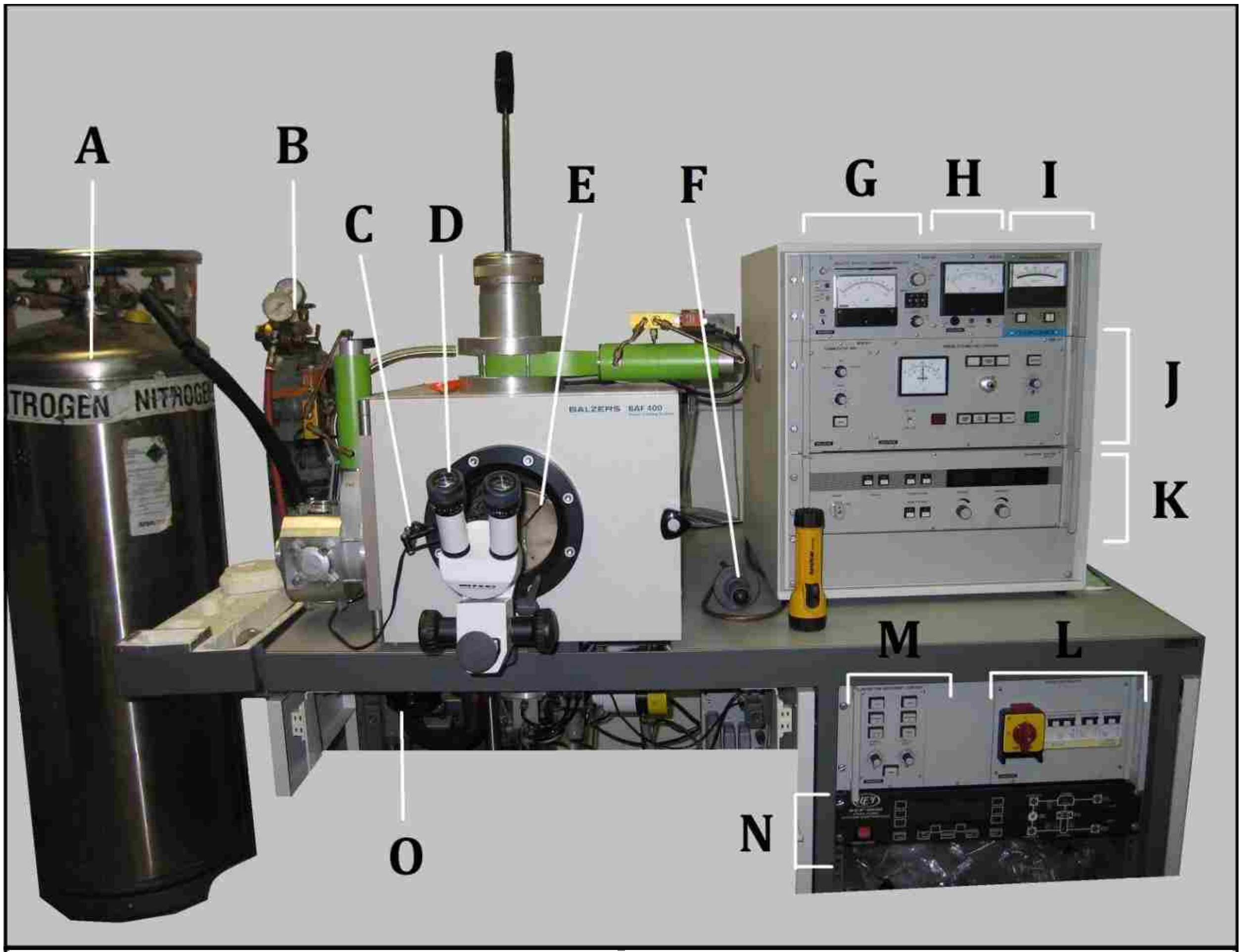

A. Nitrogen Tank, 22 psi
B. Nitrogen Cylinder
C. Lamp
D. Binoculars
E. Viewing Window
F. Grounding Probe
G. Quartz Crystal Thickness Monitor
H. Pressure Gauge
I. Cryo Temperature Gauge
J. Freeze Etching Unit Control BMS 101
K. Evaporation Control Unit EVM 030
L. Main Power Switch
M. Microtome Movement Control BMB 101
N. Key ACP-3000 Cryo Pump System Controller
O. Manual Microtome Horizontal Movement Control

Figure 3-2 Balzers BAF 400 freeze etching equipment.

3.2.1Vacuum Pumps and Controls

A cryo pump supplied by CTI-Cryogenics is used to maintain a vacuum of 4 mTorr in the vacuum chamber where replicas are produced. The cryo pump chills a cold head with a matrix attached to it for increased surface area and heat uptake. Gases remaining after a partial vacuum is formed by a mechanical pump are condensed and frozen on the matrix thereby reducing the pressure in the chamber. The temperature increases at the cold head as more gases freeze to the matrix. Eventually, the ice must be removed to return the cold head to its optimal temperature of 11 K by regenerating the matrix. This is accomplished by turning off the cryo pump, allowing the frozen gases to sublimate, and pumping off these gases with the mechanical pump. The cryo pump's helium compressor produces heat so the system is cooled with a Haskris refrigerated water chiller. House water could be used to dissipate the excess heat but wastes large volumes of water which is not sufficient during Louisiana summers.

Figure 3-3 Key ACP-3000 Cryo Pump System Controller.

The cryo pump is controlled by the Key ACP-3000 Cryo Pump System Controller (Figure 3-3), which interfaces with the cryo pump, mechanical pump, and valves that regulate the pressure in the vacuum chamber. It was added in January 2008 to replace the original inoperative controller. The diagram on the right side of the controller shows the state of the pumps and valves with a green LED (indicating open or on). Three preprogrammed modes of operation are available. Automatic mode runs a subroutine that turns on the pumps and opens the valves in the appropriate order to prevent damage to the cryo pump. Manual mode allows the user to circumvent safety measures and control each valve individually. Extreme caution should be used when in manual mode since it will allow the valve to the mechanical or roughing pump to be opened even if the chamber is under vacuum. This would result in pump oil entering the vacuum chamber. Vent mode is used when the chamber must be opened. The supervisor mode should only be accessed by a trained repair technician to program the controller and other modes.

The LCD screen provides information on the operation of the cryo pump and the pressure of the vacuum chamber. The mode of operation is displayed directly under the date and time and is followed by the pressure measurements of two thermocouple vacuum gauges (TC1 and TC2). TC1 is located in the vacuum chamber and should read 4 mT (mTorr) when the system is ready to produce replicas. TC2 is the pressure gauge associated with the cryo pump and should read 1 mT under normal operation. There is a temperature displayed on the screen labeled CRYO that is not an actual measurement but manually programmed into the controller. This temperature should be disregarded; instead, use the CTI-Cryogenics Tempurature Indicator on the upper right hand corner of the control panel to monitor the temperature of the cryo pump. The optimal temperature for the cryo pump is 11 to 12 K; however, if the temperature goes above 15 K, replicas should not be attempted and the ACP-3000 will automatically close the valve between the cryo pump and the vacuum chamber to prevent damage to the cryo pump (if in automatic mode). The temperature will slowly increase over time since the vacuum is maintained by freezing gases to a cold head. The cryo pump will have to be regenerated before the optimal temperature can be achieved.

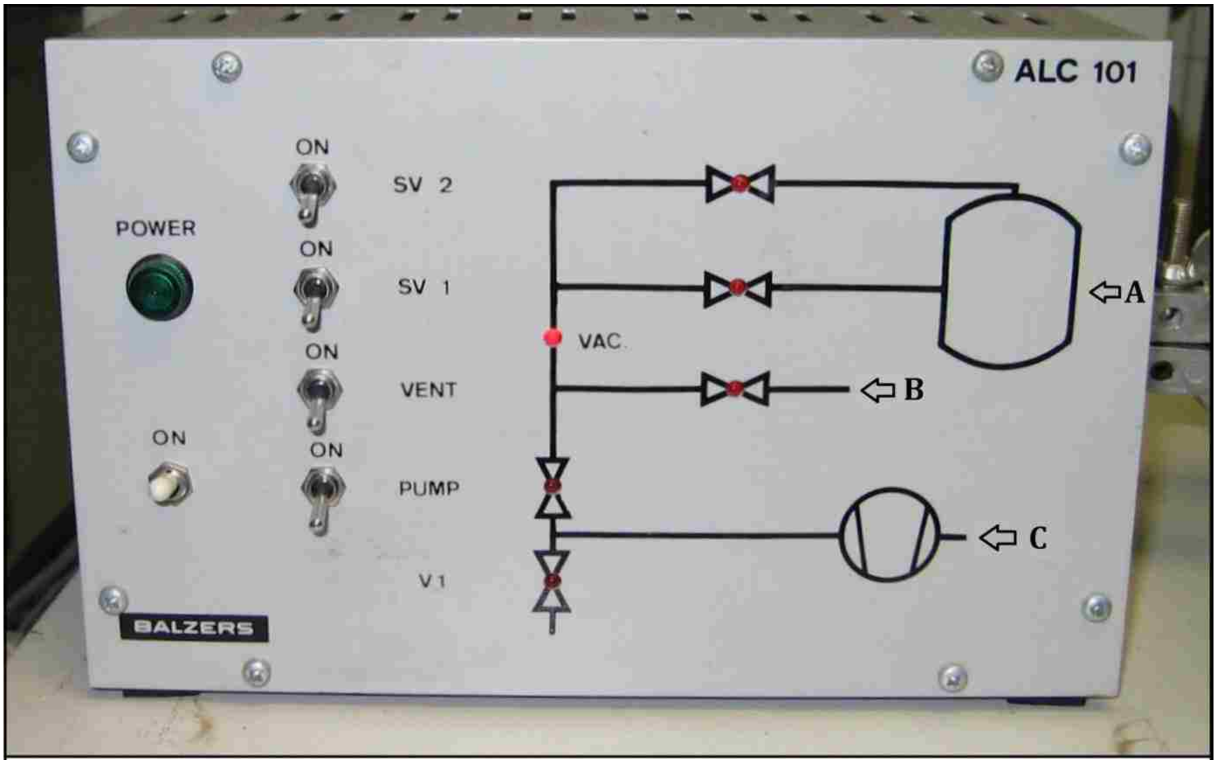

A. Vacuum Chamber B. To Atmosphere C. Pump

Figure 3-4 ALC 101 control unit for the vacuum interlock system. The switches open and close the corresponding valve written next to it. Flipping the switch to the on position opens the valve and a red LED lights up on the adjacent schematic indicating which valve is open.

The ALC 101 (Figure 3-4) valve control unit sits on top of the vacuum chamber and is used to control the valves that grant access to the vacuum chamber. The unit must be turned on and attached to 80 psi of $N_2(g)$ before any of the valves will open, including the valves that are controlled by the cryo pump controller. There are 5 labeled switches on this control unit; 1 power switch and 4 that open and close valves. In the case of the valve switches, the word "ON" is used to indicate that the valve is open. A red indicator light corresponding to the valve illuminates on the adjacent schematic that depicts where the valve is located in reference to the vacuum chamber (Figure 3-4 A). When the valve is opened, the corresponding red indicator light will be lit up. The indicator light is off when the valve is closed and the switch is in the down position. To prevent damage to the cryo pump, it is important that only one valve be open at a time. The red light next to the word "VAC" indicates that the interlock system including the locks is under vacuum. SV1 controls the specimen lock allowing for the insertion of the specimen table and SV2 works the evaporator lock for the reloading of the carbon gun. Incidentally, the abbreviation, SV, is German for *sperr-ventil*, which roughly translates to lock valve.

3.2.2 Sample Preparation

Replica making is a tedious process that starts with vitrifying liquid samples, fracturing the samples, replicating by depositing a metal, and ends with recovering the replicas by placing them on microscopy grids. This multistep process is vulnerable to countless pitfalls, often resulting in unusable replicas. Sample preparation is time sensitive so best performed quickly. It is important to make sure all of the components needed to run the experiment are readily available, clean, and dry before starting. It is very important that the specimen table is dry before use since any water will freeze and obstruct the moving parts. Preparing the *mise en place* beforehand will reduce the amount of liquid nitrogen necessary to keep the samples frozen and minimize the formation of condensation and frost contamination on the samples.

Aqueous samples are well suited for freeze fracture experiments since water can be vitrified. This is important since the formation of large ice crystals would disrupt the structures of interest. Many methods have been developed for rapidly freezing samples including expensive accessories such as a propane jet freezer. The easiest way (which was used to make the samples imaged here) is to use Freon at liquid nitrogen temperature. The sample is quickly submerged in the Freon then placed on the specimen table under liquid nitrogen. Essentially, the faster the sample freezes, the smaller the ice crystals and the better the resolution down to the grain size of the metal deposited to form the replica, which is about 5 nm for platinum.[80]

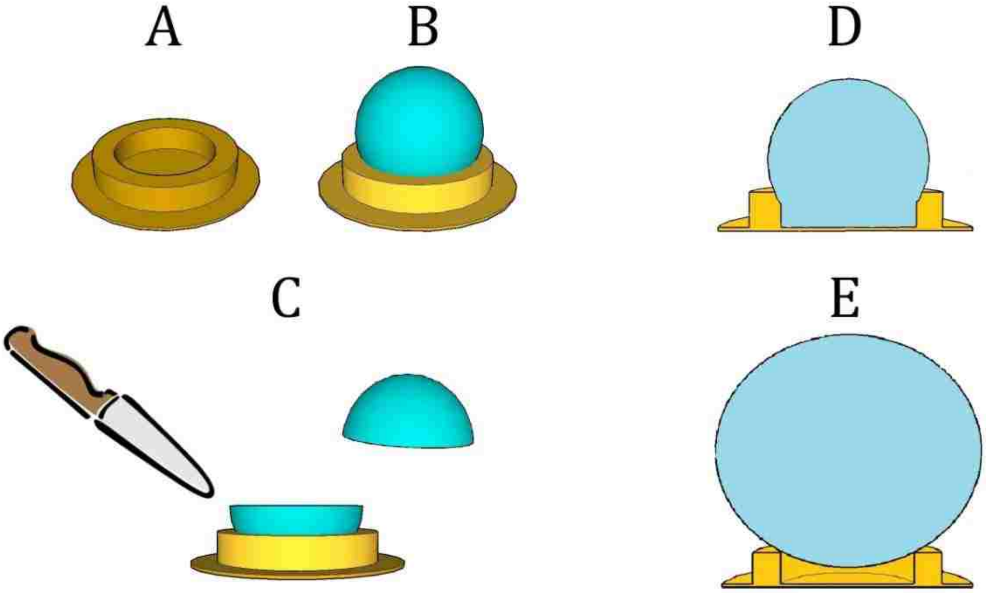

Figure 3-5 Making a good sample for freezing and fracturing. A) Gold stub with well. B) Shows the appropriate sample amount. C) The sample after fracture with the microtome knife. D) A good sample should fill the well completely. E) Adding the drop before filling the well can create an air pocket preventing good adhesion with the gold stub.

Gold stubs with a well (Figure 3-5 A) are used to hold a droplet of sample and, once frozen, are placed on the specimen table. The same amount of sample should be placed on each gold stub so they can be fractured simultaneously. The droplet applied to the gold stub must sit in the well as in Figure 3-5 B and D. Too much sample, Figure 3-5 E, can cause inconsistent fractures where the sample crumbles leaving a jagged surface or the sample is knocked off the gold stub completely. The specimen table (Figure 3-6) holds 3 gold stubs under tines that are raised with a removable lever. Once the samples are frozen and placed on the specimen table under liquid nitrogen, it is time to insert the specimen table into the BAF 400.

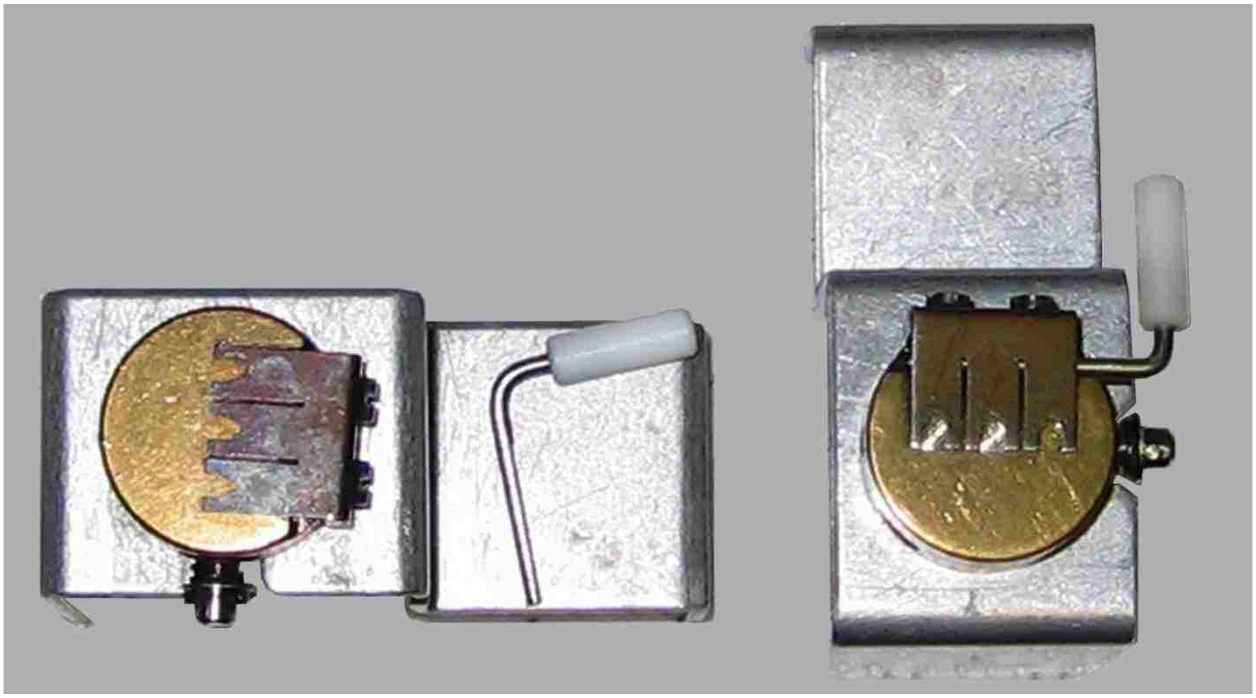

Figure 3-6 Specimen tables on holders. The specimen table on the right has two gold stubs in place with the right most sample position empty. The L-shaped lever with the plastic grip is used to raise and lower the tines that hold the gold stubs to the specimen table. The lever must be removed before the specimen table can be inserted into the vacuum chamber for replication.

3.2.3Fracturing using a Microtome Blade

Fracturing is performed in a vacuum chamber using a liquid nitrogen cooled microtome blade and stage under a cold shroud so the sample does not sublimate upon contact. The BAF 400 is equipped with a viewing port with a pair of binoculars mounted outside the chamber for positioning the knife on the microtome behind the samples. The knife should be moved so it is directly behind the samples in position to cut all three samples on the specimen table simultaneously. Once the knife is in a satisfactory location, rotate the microtome in a smooth clockwise motion to make the fracture. It is optional to etch the newly fractured samples to expose more of the structures for replication. A deep etch can be achieved by raising the temperature of the stage to -100 °C for 3 to 10 min. After fracturing, the samples can be protected by placing the back of the microtome over the specimen table.

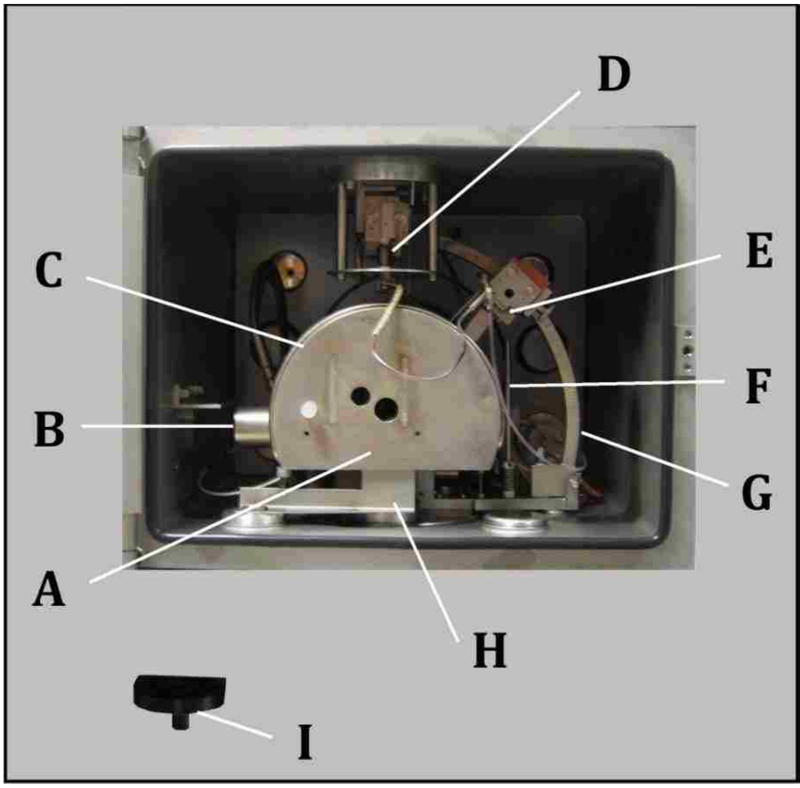

A. Quartz Crystal Microbalance (QCM) (Underneath Cold Shroud)
B. Port for Specimen Entry
C. Cold Shroud
D. Carbon Electrode Beam Gun
E. Platinum Electrode Beam Gun
F. Support for Cold Shroud When Raised
G. Gun Mounting Arc
H. Cold Stage
I. Microtome Horizontal Movement Control

Figure 3-7 BAF 400 vacuum chamber with components labeled.

3.2.4Electron Beam Evaporator

Two guns are used to produce replicas, one for evaporating platinum (from a carbon rod with a Pt pellet inserted in the tip) at a 45° angle to the specimen table and one for depositing a carbon backing located above the samples. The voltage and current are different for each electron beam evaporator. The Pt gun uses 1.6 kV and 60 amps current while the carbon gun requires 1.9 kV and 90 amps. A quartz crystal microbalance (QCM) is used to monitor the thickness of the Pt and carbon film deposited. It is prudent to check that the guns are functioning prior to preparing a sample by firing the guns and verifying that the QCM detects some material accretion. Start out using the aforementioned values; if the QCM does not show deposition, the voltage and current can be increased. The carbon gun can be safely increased to 2.1 kV and 100 amps, but it is not suggested to go any higher. The Pt gun is more reliable, so it is rarely necessary to increase the voltage or current when depositing Pt. It takes a few seconds for the correct voltage and current to be reached after the gun is turned on. Covering the samples with the back of the microtome arm will prevent any material accumulation before the gun has attained the correct bias. When the gun is ready, move the microtome back to expose the samples and deposit 2 nm of Pt followed by 150-200 nm of carbon. Carefully watch the QCM to know when to turn off the gun.

The QCM is composed of a quartz crystal resonator that is positioned next to the specimen table and is coated along with the samples. As the thickness of the deposited coating increases, the resonate frequency of the crystal changes, the quartz crystal thickness monitor converts the oscillation from Hertz to nanometers, and displays the result. The reference frequency must be set to zero before each gun is used. If the density is set to 2.0 $g{\cdot}cm^{-3}$ and the scale range to red ×1, stop depositing material when the needle reaches 20 nm on the red scale for both Pt and carbon guns. Depositing any more platinum or carbon can result in replicas that are too thick to view in the TEM. The density of the deposited material should be accounted for in order to obtain the true thickness. The value obtained from the quartz crystal thickness monitor must be divided by 10 for Pt and multiplied by 10 for carbon to obtain the desired 2 and 200 nm, respectively.

The platinum-carbon gun can be used up to 6 times before maintenance is required. Typically the filament (or cathode) should be replaced at the same time as the Pt-C rod. In order to remove the Pt-C electron gun, the sample chamber must be vented. Liquid nitrogen is not necessary to replace either of the guns; however, the vacuum and interlock chambers are vented through the pipe that connects the BAF 400 to the liquid nitrogen tank visible in Figure 3-2. If $N_2(l)$ is available, connect the pipe to the $N_2(l)$ tank and open the valve slightly to vent the vacuum chamber and purge the system with N_2 in order to minimize moisture and room particulate matter contamination; otherwise, the pipe should not be attached to the tank. The ALC 101 valve controller must be on to open the valve necessary to vent; this requires compressed $N_2(g)$ regulated to 80 psi. Venting the vacuum chamber will be done by the cryo pump controller.

The platinum-carbon rod consists of a carbon rod with a hole drilled on each end and a platinum insert. The Pt insert is loose and must be fused with the carbon rod. Although the Pt-C gun tends to be more reliable than the carbon gun, it is crucial that the Pt insert is properly set. A common setback occurs when the Pt insert falls out of the predrilled carbon rod. Hopefully the user realizes this before replication is attempted. It is suggested that the guns be degassed and tested prior to preparing any samples for replication.

It is important to follow the steps to fuse the Pt insert with the carbon rod. The Pt insert should be melted to the carbon rod by passing current through the gun. The Pt-C gun must be inserted with the Pt-C rod pointing up since the Pt insert is loose. The sample chamber has to be under vacuum in order to pass current through the gun (less than $1 \times 10^{-}$

^{4} mbar). The cryo pump does not need to be on to fuse the Pt to the carbon rod. It only takes 4 seconds to sufficiently melt the Pt insert to the carbon rod. Unfortunately, this method requires that the Pt-C gun be inverted, so the chamber will have to be vented and the gun repositioned before it can be used to make replicas. Alternatively, the Pt insert can be squeezed out of round with a pair of pliers to help it fit snuggly in the carbon rod. This does not work every time and there is a chance of losing the Pt insert while trying to deform it; however, the gun will not have to be inverted and repositioned to fuse it. If all goes well, the Pt-C gun will be ready for use once it is degassed.

A hundred times more carbon is deposited each time replicas are made, so the carbon rod should be replaced after every other use. Sometimes it is possible to get as many as 3 depositions from the carbon gun, but it is not worth risking if the samples are valuable. The filament (or cathode) can last up to 6 depositions, but becomes brittle once an electrical current has been applied. It may be possible to get a couple more depositions out of the filament; but since it gets so fragile, it usually needs to be replaced after 6 times. The filament should be inspected each time the carbon rod is replaced for signs of fatigue such as warping or stress cracks. If the filament shows either, replace the filament as well. The filament can be used longer if it is still in good shape and it has been used less than six times, but be careful not to damage it while replacing the carbon rod and cleaning carbon residue from parts.

The BAF 400 allows the carbon gun to be removed without venting the vacuum chamber by extracting it through an interlock system. In order to remove the carbon electron gun, the sample chamber must be under high vacuum. This means the cryo pump controller must be on and working correctly. Removal of the carbon gun also requires the same conditions necessary to replace the Pt-C gun, but the vacuum chamber remains closed. A special attachment on the carbon gun allows an extraction rod to be used to pull it out.

The evaporation sources should be degassed before use. This is especially important after replacing the rods or any time the vacuum chamber is vented to the atmosphere. Degassing will prevent pressure spikes in the vacuum chamber and reduce arc overs at the evaporation sources. The voltage and emission current for degassing is preset on the EVM 030 Evaporation Control Unit and specific for each gun. The carbon gun uses 1.5 kV and 50 mA while degassing and should be degassed for 5 minutes after the carbon rod is replaced. The platinum-carbon gun should be degassed for 2 minutes after the rod is replaced at 1 kV and 50 mA. The guns may not require the full degassing time and the control unit will terminate the degassing process when the voltage and current stabilizes early.

Before the EVM 030 will allow material deposition or degassing to occur, the vacuum chamber must be under high vacuum conditions. The cryo pump controller should be in automatic mode and operating within normal parameters. Anytime the vacuum chamber is vented, both guns should be degassed. When servicing the carbon gun, only it will need to be degassed once it is replaced in the vacuum chamber. A step-by-step, standard operating procedure has been included in the appendix of this document on sample prep, replication, gun maintenance, and degassing.

3.2.5 Replica Mounting

Getting a clean replica mounted on a microscope grid is the last phase of sample preparation. Cleaning depends on the sample properties and may require several days and multiple rinses. Biological samples, such as yeast, should be cleaned in bleach followed by washing the replica in deionized (DI) water. If the sample is easily dissolved, the original solvent can be used with subsequent washes in DI water. The replicas can be left in the cleaning solution overnight as long as they do not dry out and the cleaning solution is very mild i.e. DI water. Use a well plate to wash the replicas by filling the first column of wells with cleaning solution and the remaining wells with water. Use an inverted Petri dish to cover the well plate to prevent the replicas from drying out.

The replicas are delicate and the challenge is to keep them intact. The gold stub with replica should be added to the cleaning solution carefully. Hold the gold stub with a pair of tweezers along the edge of the well just in contact with the solution. When the sample thaws, release the gold stub, which will slide down the side to the bottom of the well, and the replica should float on the surface of the liquid.

Several tools are necessary when washing replicas and transferring them to a microscope grid. These include wire loops, glass pipettes with a beaded tip, and an eyelash brush (Figure 3-8). The loops and glass pipettes are used to pick up the replica to place it in a clean bath for washing. If the replica breaks apart, make sure to wash everything since even the smallest piece can be imaged. If the replica sinks, it can still be recovered using the eyelash brush and glass pipettes. The replica may roll up and can be flattened back out on a grid using the eyelash brush and a pair of binoculars.

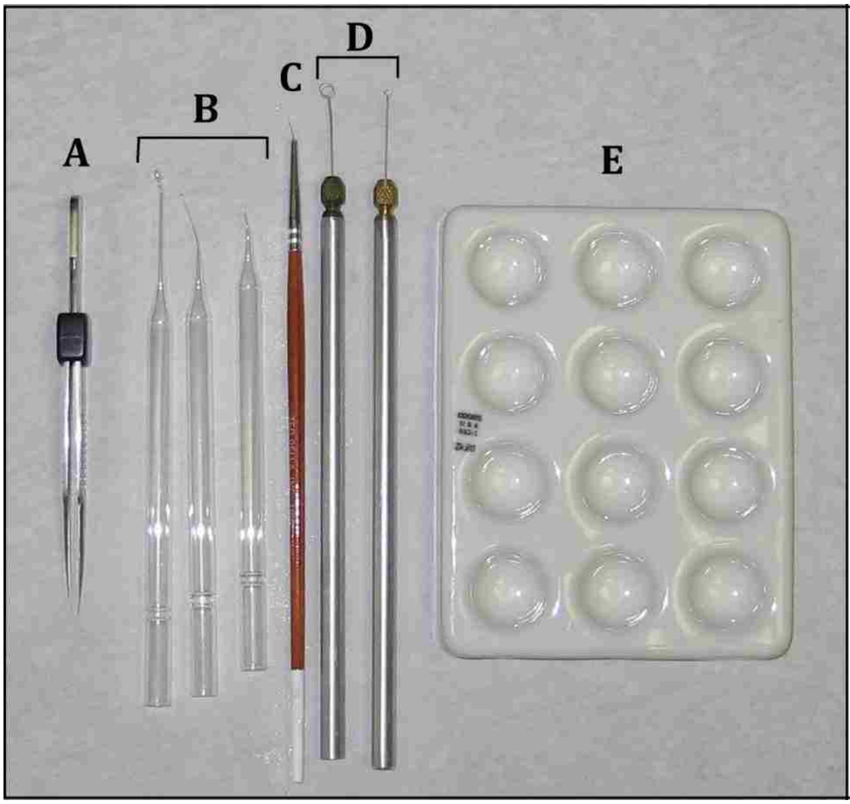

A. Tweezers
B. Glass Pipettes with Beaded Tips
C. Eyelash Brush
D. Wire Inoculating Loops
E. Ceramic Well Plate

Figure 3-8 Tools for manipulating replicas during washing in a well plate and placement on a grid.

The type of microscope grids used is up to the microscopist. Collodion-coated copper grids are often used; but if the holes in the grid are small enough, they can be used bare. The coating helps the replica stick to the grid; otherwise, the grid tends to repel the replica. Dipping the uncoated copper grid in 10 ml of water with 2 drops of ammonium hydroxide will encourage the replica stick making it less hydrophobic. The replicas can be scooped up with a grid from underneath or can be dabbed directly off the top of the water from above. It is important to note the side of the grid on which the replica is placed. Using the shiny side of the grid is suggested and ensures that the grid will be placed in the microscope correctly: replica pointing up.

Blot the grids on a filter paper or a tissue wipe to remove the water. Always blot from below; otherwise, the replica could be wicked off the grid by capillary forces. It is also necessary to remove the water from between the tips of the tweezers by sliding a tissue between the two prongs. This will make it easier for the grid to be released in the container or surface of choice. A good choice for storage is a grid holder, but a covered Petri dish lined with filter paper will suffice. The filter paper can be taped down and the edge of the tape can be used to lightly secure the grids. If the tape is too sticky or too much of the grid is in contact with the tape, it may be difficult to extract the grid from the tape and damage may occur. Allowing the grids to dry for a few minutes then transferring the grids to a grid holder works best.

3.3 Results and Discussion

Transmission electron microscopy (TEM) is used to image the replicas since one side is coated with carbon. Interpreting TEM images of replicas requires understanding 3 possible fracture outcomes: concave fracture, convex fracture, and cross-fracture. Platinum is deposited at a 45° angle to create a shadow cast by protruding structures. The shadow is white, showing the absence of Pt in the TEM image. Orienting the image so that the dark Pt areas are below the white shadows will make the images easier to evaluate. Concave fractured objects will appear light to dark and the shadow will remain within the structure cavity. Convex fractured objects will be dark to light and the shadow will often extend outside the margins of the structure. Cross-fractured objects are uniform in contrast with little to no shadowing. It is also important to know the sample's composition and what structures are expected. Biology textbooks can provide much of the information a microscopist needs to analyze images of cells.[81,82]

Yeast is a common biological reference for size and was used to test FF equipment and practice technique. The first FF images of yeast were performed by Moore et al in 1963 and his work has been invaluable in understanding FF experiments performed in this dissertation.[75] The image of yeast in Figure 3-9 shows 4 yeast cells in the fracture plane. Two of the cells are cross-fractured exposing the intercellular structures and the bottom 2 cells are convex fractured. Clearly visible in the cell in the upper left is the nucleus, some vacuoles, and the cell wall of the yeast. The bottom 2 cells show the inner structures of the cell wall with rod-like invaginations in the protoplasm face. Invaginations are common ultrastructural elements of the cytoplasmic membrane of yeast cells and their size and quantity depends on the species of yeast, culture media, and age.[75,83,84] Between the invaginations are an hexagonal arrangement of particles with a lattice period of approximately 180 Å (Figure 3-10) that was also observed by Moor et al.[75] These structures can be used as an internal scale due to their regularity.

Figure 3-11 is an image of a young yeast cell in the final stages of dividing from the parent cell in the lower right hand corner. The high water content of the cell is observed through the formation of small ice crystals giving the cytoplasm a rough texture. There is further evidence of ice in the form of damage along the cell wall where the protoplasmic membrane has ruptured into the cytoplasm and areas along the exterior of the cell are irregular.

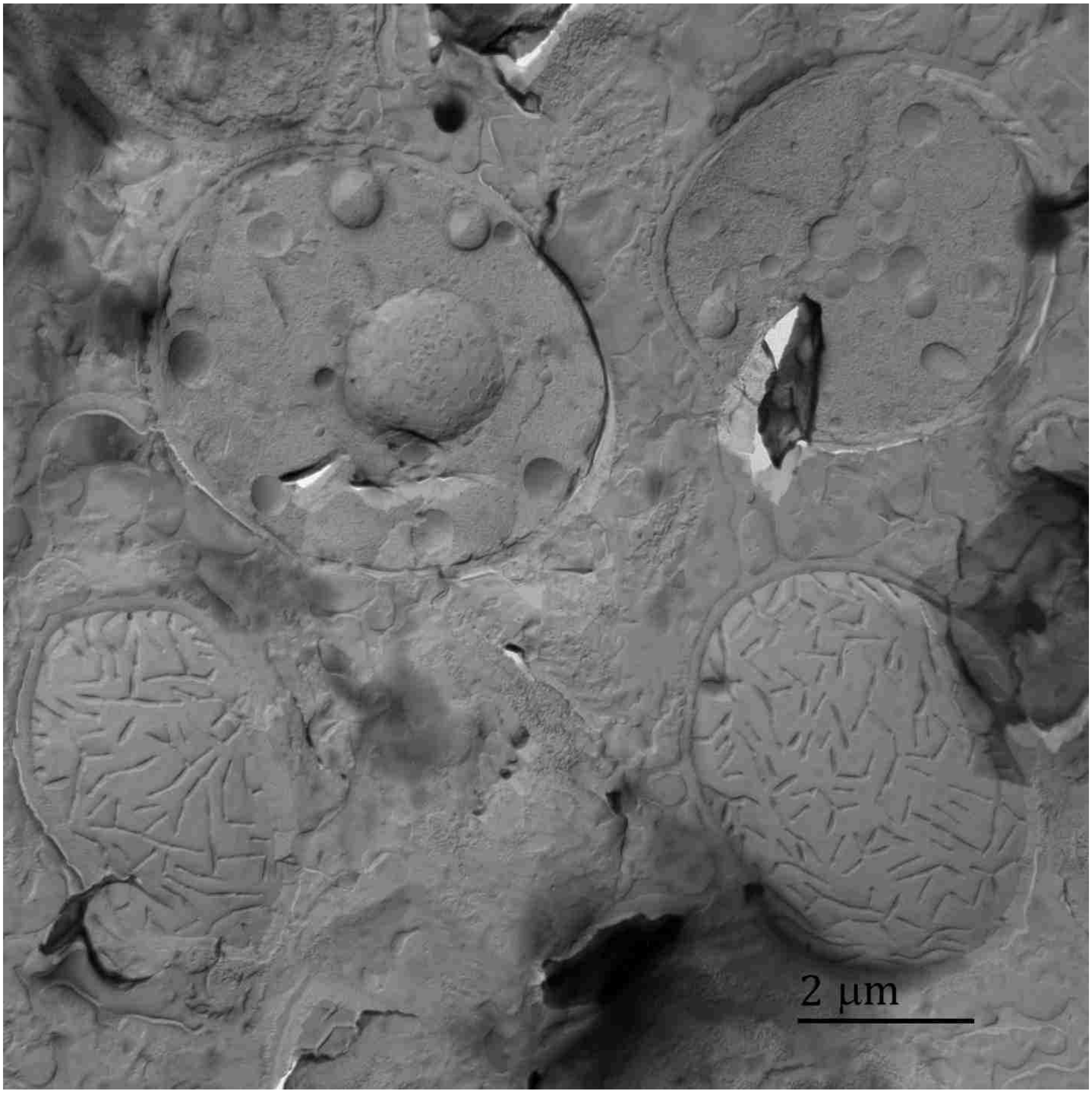

Figure 3-9 FF-TEM of 4 yeast cells that were at different heights in the matrix when the fracture plane was created. The 2 cells at the top were cross-fractured through the yeast cell while the bottom 2 were convex fractured through the cell wall.

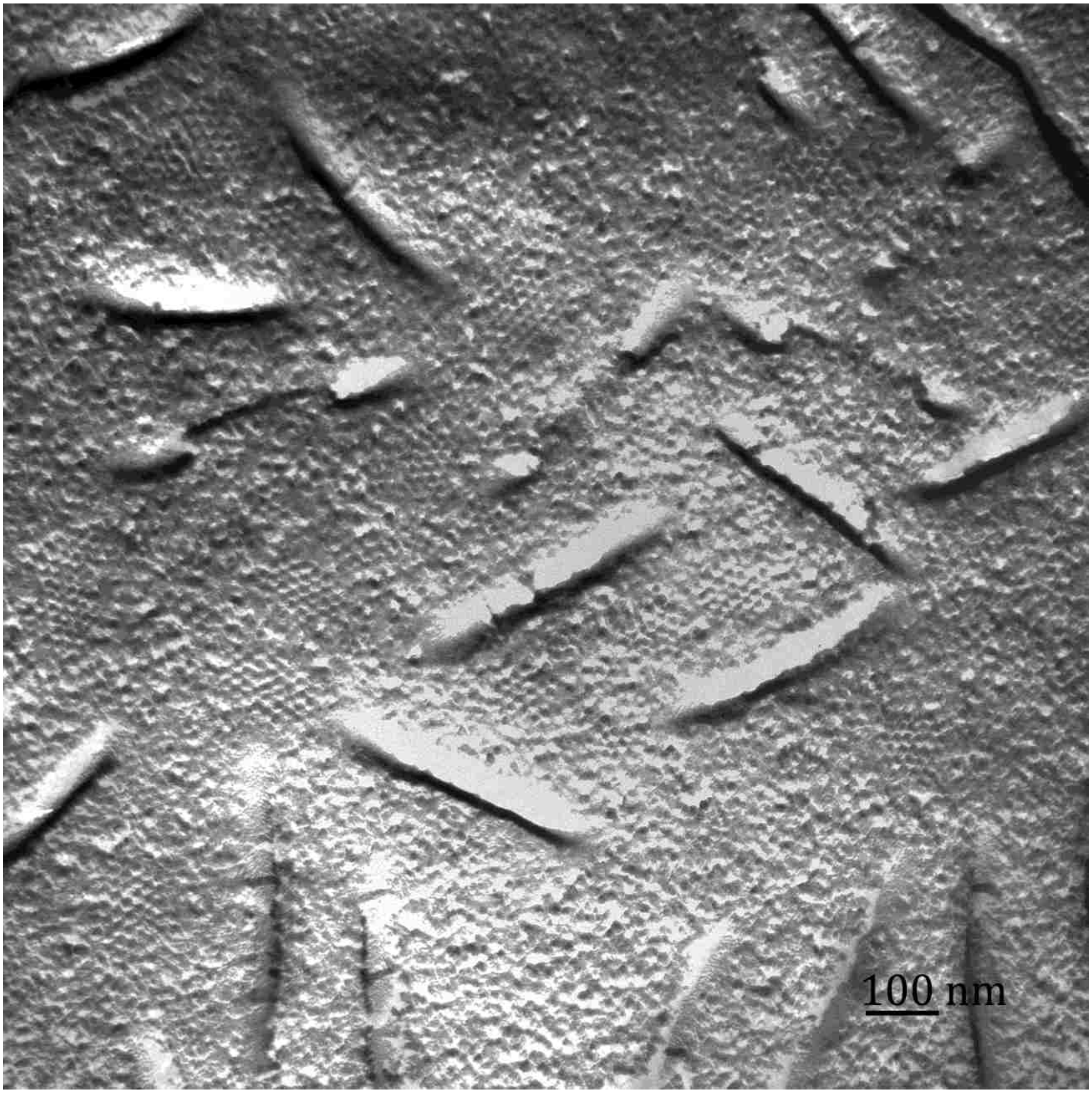

Figure 3-10 Magnified view of protoplasm face of a yeast cell showing the hexagonal arrangement of particles between the invaginations with a lattice period of 180 Å.

Figure 3-11 FF-TEM of a cross-fractured yeast cell where the fracture plane cut the yeast in half exposing the interior of the cell.

Figure 3-12 is an image obtained when latex spheres were replicated. The dark circles are latex particles remaining on the surface. Some of the particles appear to be embedded in the surface of the replica since they cast a white shadow while others are unwashed particles contaminating the surface. This indicates that the replica was not thoroughly cleaned and requires a more stringent washing protocol. Acetone could be used to dissolve the polystyrene spheres while leaving the replica intact, but would require repeated washings in water to remove all the solvent.

3.4 Conclusion

"Practice makes perfect" is the motto of the FF experimentalist. Over time, reading the images will become second nature and the technique will yield striking pictures.

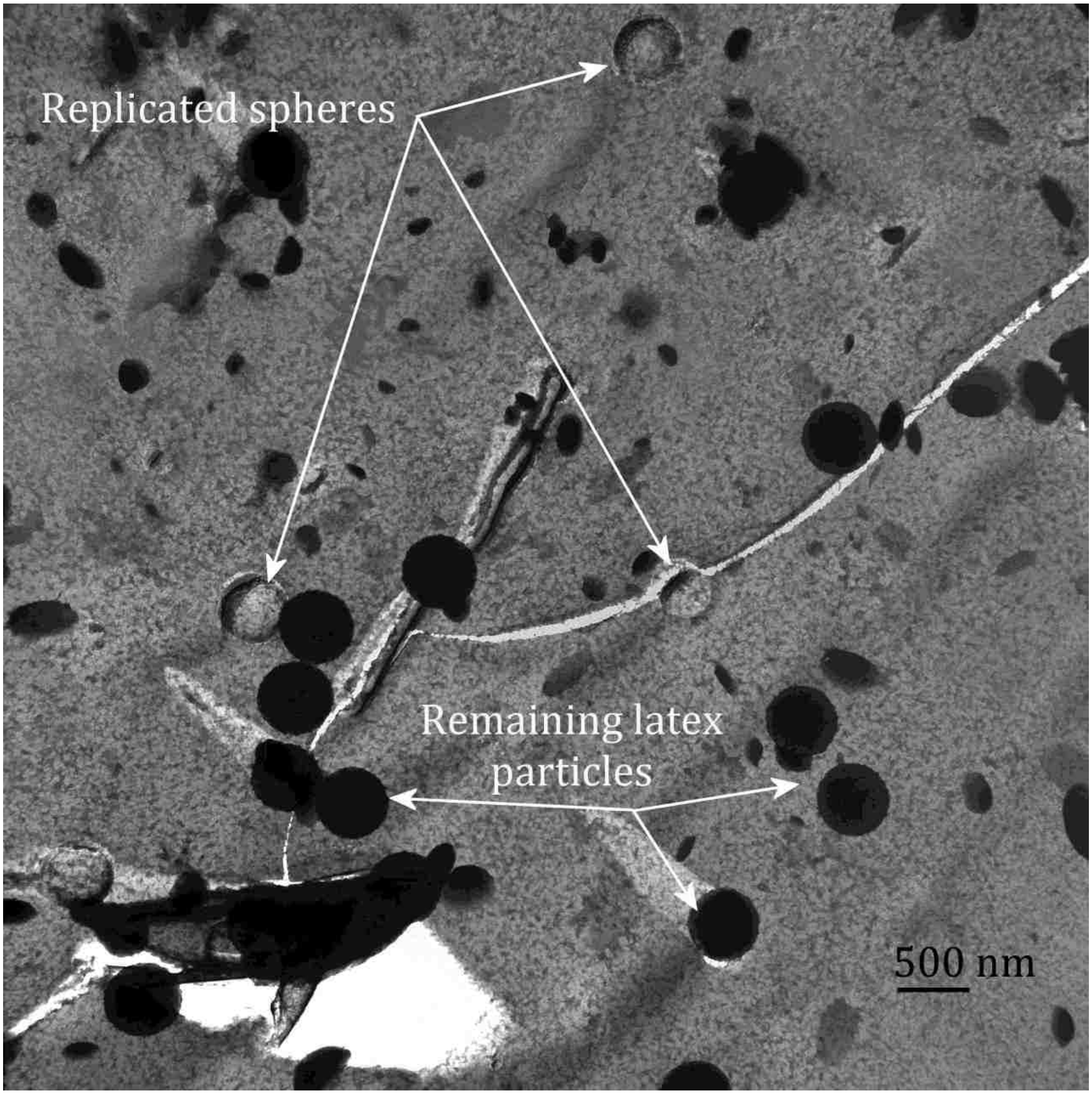

Figure 3-12 TEM image of latex spheres that were replicated using the Balzers BAF 400. The dark circles are latex particles that remain on the replica surface.

CHAPTER 4 LIPOSOME AND DENDRIMER INTERACTIONS

4.1 Introduction

Tracking the size change of the liposomes will be accomplished predominately with SAXS and FF-TEM. The general nomenclature for two lipid bilayers, Figure 4-1, is the lamellar repeat spacing (D), the Luzzati thickness (D_B), the water thickness (D_W), the steric thickness (D'_B) and the steric water thickness (D'_W).[85] Distances from literature vary from 60-64 Å[86-89] for D and 35.9-36.1 Å[86,90] for D_B depending on temperature, pressure, and hydration. These conditional variations could pose a problem when trying to determine if the size change is a result of the addition of dendrimers or some environmental factor.

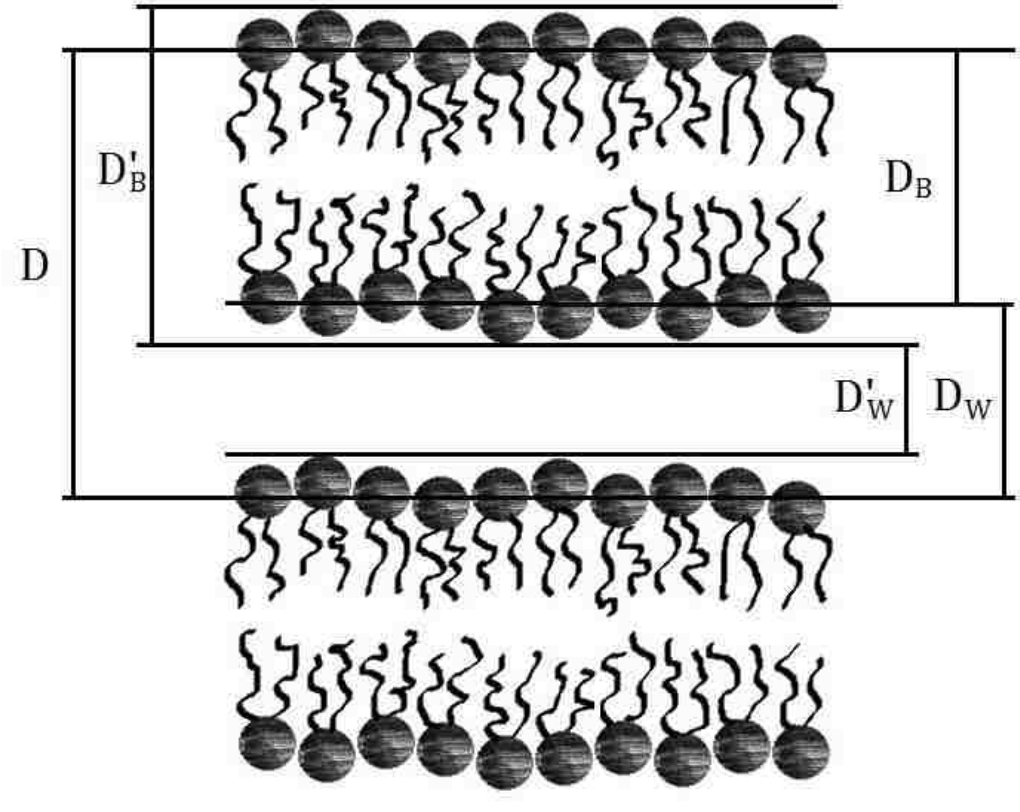

Figure 4-1 Schematic of two lipid bilayers adapted from Petrache et al.[91] D is the repeat spacing for the stack of the bilayers; the bilayer thickness is indicated by subscript B and the water space by subscript W.

Part of understanding the interaction of dendrimers and vesicles is the hypothesis that the dendrimers will interact with the surface of the liposome slightly increasing its diameter. This represents a small change in the structural features of the system, which requires measurements at high *q* due to the inverse nature of scattering experiments. Figure 4-3 relates the liposome structure to the bilayer nomenclature of Figure 4-1. The lamellar repeat spacing (D) is equivalent to the radius of the liposome while DB is synonymous with the thickness

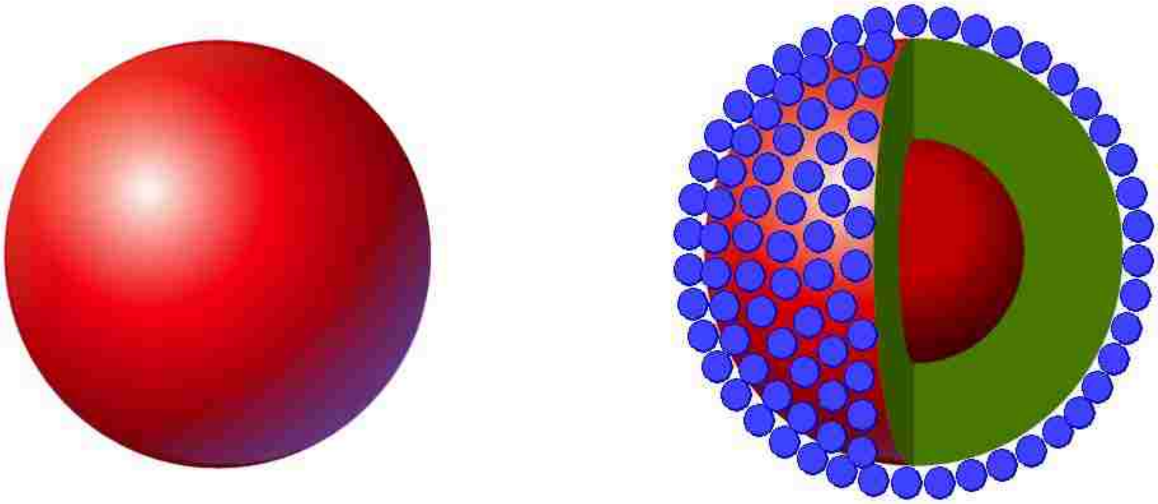

Figure 4-2 Possible interaction where dendrimers (blue spheres) associate with the surface of the liposome (large red bubble). The radius of the system will change.

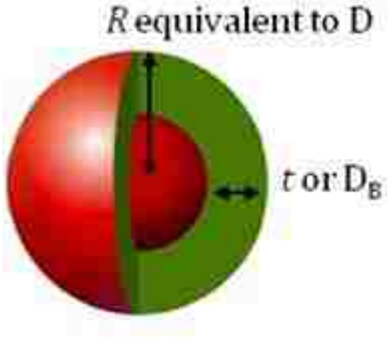

Figure 4-3 The parameters that will be used to discuss the size changes observed. The lamellar repeat spacing (D) is equivalent to the radius of the liposome while D_B is synonymous with the thickness.

4.2 Materials and Methods

4.2.1 Materials

4.2.1.1 Lipids and Liposomes

There are many types of lipids to chose from, but the research discussed herein predominately uses 1,2-dioleoyl-*sn*-glycero-3-phosphocholine (DOPC). This lipid is zwitterionic and has a gel transition at -20°C, so heating of the lipid solution during liposome formation is not necessary. The DOPC was purchased from Avanti® Polar Lipids, Inc. dissolved in chloroform at 10-20 mg/ml.

4.2.1.2 Liposome Preparation

Liposomes are prepared in a multi-step procedure designed to produce a narrowly distributed solution of unilamellar vesicles. The lipid must first be dried into a film. This is accomplished by placing the chloroform and lipid solution in a round bottom flask (RBF) and then drying under vacuum on a rotary evaporator. Within an hour, all the chloroform has evaporated and a multilamellar film is left on the bottom of the RBF. To assure all the chloroform is removed and that no moisture is present, the flask is placed in a vacuum oven for several hours (4 or more hours, but less than 24 hours) at room temperature. The next step is to form multilamellar vesicles. MLVs are formed by placing glass beads in the bottom of the flask, adding a couple milliliters of a phosphate buffer solution (PBS), and rotating on a rotary evaporator under nitrogen purge for an hour. The PBS used to hydrate the lipid film consists of 2.5 millimolar (mM) Na_2HPO_4, 10 mM NaCl, and 1 mM NaN_3 and was adjusted to pH ~7.0 with 1 normal (1 molar) hydrochloric acid. The NaN_3 is added to inhibit any biological growth and increase the shelf life of the PBS and solutions. A freeze-thaw procedure is used to help create uniform vesicles once the dry lipid film has been hydrated. In each cycle of the procedure, the flask is placed in liquid nitrogen and then thawed in warm water. The freeze-thaw cycle is repeated 10 times before the resulting MLVs are extruded. In order to make the vesicles smaller, the mixture is sonicated for approximately 10 seconds in between thawing and refreezing after the 3rd, 6th, and 9th thawing cycle. Finally, the MLVs are extruded using an Avanti® Mini-Extruder through a 100 nm in diameter pore size polycarbonate (PC) filter membranes. These PC membranes are purchased from Avanti® Polar Lipids Incorporated, and feature uniform channels that go straight through the membrane. Two PC membranes are used in the mini-extruder both as a precaution and to form more uniform liposomes. The filters are carefully placed with special tweezers designed to prevent scratches or tears. The solution of MLVs is then passed through the filters 41 times. This results in monodispersed, unilamellar vesicles with a diameter of 100 nm.

4.2.2 Dendrimers

Research on dendrimers has exponentially increased since Vögtle and coworkers first reported their synthesis in 1978.[92] Dendrimers are uniform particles with narrow molecular weight distributions and offer a wide array of surface functionality through endgroup modification. Dendrimers can be synthesized by two methods: convergent and divergent. Vögtle used the later while convergent synthesis appeared in 1990 from Fréchet.[93,94] Divergent dendrimers are synthesized by the sequential addition of monomer starting with a central initiator core.[95] With each addition of monomer, the dendrimer increases one “generation” or layer at a time and the resulting molecule grows larger in diameter, has twice as many surface groups, and the molecular weight roughly doubles.

4.2.2.1 Polypropylenimine Dotriacontaamine Dendrimer (DAB-Am)

Polypropylenimine dotriacontaamine dendrimer (DAB-Am) was purchased from Sigma-Aldrich and used as received. The DAB-Am used herein will be further described by the number of surface groups present; for example, DAB-Am-32 has 32 amine functional groups and is a 4th generation dendrimer.

4.2.2.2 One-Directional Arborol Dendrimer

One-directional arborols are amphiphilic dendrimers with hydrophilic head group composed of 9 hydroxyl groups and a short alkyl chain for the hydrophobic tail. The dendrimers ([*m*]-*n*) were synthesized by Dr. Jirun Sun[96] using methodology perfected by Newkome et al.[97] They are described by the number of terminal hydroxyl groups and the carbons in the alkyl chain, i.e. [9]-10.

4.3 Methods

4.3.1 Dynamic and Static Light Scattering

Dynamic Light Scattering is useful to measure the motion of particles in solution. This is accomplished by monitoring the intensity fluctuations of the scattered light with a correlator to obtain an autocorrelation function. This function, $g^{(1)}(\tau)$, can be used to determine molecular size, shape, and diffusion from the distribution of the relaxation rate. The decay of the autocorrelation function follows an exponential profile:

$$g^{(1)}(\tau) = e^{-\Gamma\tau}$$

Equation 13

where Γ is the decay rate and is proportional to the diffusion coefficient by:

$$\Gamma = q^2 D_{\mathrm{m}}$$

Equation 14

where q is the scattering vector magnitude:

$$q = \left(\frac{4\pi n}{\lambda_0}\right) \sin\left(\frac{\theta}{2}\right)$$

Equation 15

where n is the refractive index of the solution, λ_0 is the in *vacuo* incident light wavelength, and the scattering angle is θ.

The Stokes-Einstein equation can be used to obtain size information by the apparent hydrodynamic radius, $R_{\mathrm{h,app}}$:

$$R_{\mathrm{h,app}} = \frac{kT}{6\pi\eta D_{\mathrm{app}}}$$

Equation 16

With a Guinier plot, the radius of gyration can be solved using the following relationship.

$$\ln\big(I(q)\big) = \ln\big(I(0)\big) - \frac{q^2 R_{\mathrm{g}}^2}{3}$$

Equation 17

The DLS measurements were performed on a custom apparatus equipped with a He-Ne laser at 632.8 nm and EMI-9863A/100 PMT selected for low dark count (~5 s^{-1} at room temperature) and low correlated after-pulsing. A Pacific Precision Instruments wide-range photometer/preamplifier/discriminator drives an ALV pulse shaper, which in turn feeds an ALV 5000 correlator. The samples were maintained at 25°C and measurements were recorded at scattering angles of 30°-135°. The data were analyzed with CONTIN software.[98,99] The program chose the solution automatically. The apparent mutual diffusion coefficient was extracted from a linear relationship between Γ and q^2, where Γ is the decay rate and q is the magnitude of the scattering vector. In case of a poor linear relation, the apparent mutual diffusion coefficient was estimated from Γ/q^2 at five measured angles by linear fitting of Γ/q^2 versus q^2, taking the intercept zero q. The apparent mutual diffusion coefficient, $D_{\mathrm{app}} = \Gamma/q^2$ can be computed and a plot of D_{app} vs. q^2 should be flat for monodispersed and spherical molecules i.e., LUVs.

4.3.2 Small and Wide Angle X-ray Scattering

Small/wide angle X-ray scattering will give insight on the structural features of our system. This is accomplished by detecting the coherent scattering pattern that is caused by inhomogeneities in the electron density of the sample. The form factor for a sphere is:

$$\mathrm{P}(q) = \left[\frac{3}{x^3}(\sin x - x\cos x)\right]^2 \quad \text{where } x = qR$$

Equation 18

The form factor for spherical shell is called the Rayleigh-Gans-Debye (RGD) formula[100,101] and is given by Equation 19 below.

$$P(q) = \rho^2 \left[\left(R + \frac{t}{2}\right)^3 \left(\frac{\left(j_1\left(q\left(R + \frac{t}{2}\right)\right)\right)}{q\left(R + \frac{t}{2}\right)} - \left(R - \frac{t}{2}\right)^3 \right) \left(\frac{j_1\left(q\left(R - \frac{t}{2}\right)\right)}{q\left(R - \frac{t}{2}\right)} \right) \right]^2$$

Equation 19

R is the vesicle radius, ρ is the average contrast, t is the membrane thickness, q is the scattering vector, and $j_1(x)$ is given by Equation 20.[101]

$$j_1(x) = \frac{\sin x}{x^2} - \frac{\cos x}{x}$$

Equation 20

4.3.3 Freeze Fracture and Electron Microscopy

Freeze fracture or etching (FF) is a specialized technique for preparing liquid samples where solutions are rapidly frozen, fractured, and coated with platinum to form a replica for imaging with an electron microscope. This equipment is located at the LSU School of Veterinary Medicine.

Electron microscopy will be used to provide real space images of liposome and dendrimer. Most of the transmission electron microscopy (TEM) images were obtained at the School of Veterinary Medicine on a JEOL JEM 1011 using the AMT XR-60 digital camera. Some images were taken at the Louisiana State University Department of Biological Sciences in the Socolofsky Microscopy Center on a JEOL 100CX using photographic negatives that are digitized on a high resolution scanner.

4.4 Results and Discussion

The formation of ULV was verified using DLS and SLS. The size was determined and the hydrodynamic radius ranged from 46-66 nm while the R_g was 52-62 Å. Comparing these two radii provides a means of evaluating the uniformity of spherical liposomes and is called the axial ratio where t is the bilayer thickness. The closer the axial ratio is to 1, the more monodisperse and spherical the liposomes.

$$\text{Axial Ratio} = \frac{R_\mathrm{g} + \frac{t}{2}}{R_\mathrm{h}}$$

Equation 21[102]

Table 4-1 contains the cumulants analysis of DLS and the Guinier analysis of SLS for several DOPC ULV samples including a mixture of liposomes and [9]-6 arborol with a 10:1 ratio. The liposomes only contain DOPC lipid and are monodisperse, roughly the same size, and spherical. The 5 day study showed the liposomes begin to deteriorate after a couple of days and are probably not ULV by day 5. The addition of other lipids or cholesterol should increase the stability[103-106] of the liposomes but was avoided in order to work with the simplest system possible.

Table 4-1 Size determination of extruded liposomes and stability test. The R_h, R_g, and axial ratio of liposomes are similar, but begin to change the day after they are extruded.

Sample	R_h (nm)	R_g (nm)	Axial Ratio
DOPC 1 Day 1	46.2 ± 0.2	52.6 ±0.6	1.18
Day 2	64.8 ± 2.3	87.1 ± 9.8	1.37
Day 5	66.5 ± 3.4	15.6 ± 26	0.26
DOPC 2	57.5 ± 0.6	61.0 ± 0.8	1.09
DOPC 3	58.3 ± 0.8	62.9 ± 0.5	1.11
DOPC 3 and [9]-6 (10:1)	53.0 ± 0.5	56.1 ± 1.5	1.09

The addition of the 1-directional arborol decreased the size of the liposome, but did not affect the axial ratio. This result was unexpected since the 1-D arborol was predicted to interact with the surface of the liposome increasing the overall size. It was hoped that the hydrophobic tail would insert into the liposome and the hydroxyl groups remained at or near the outer surface of the liposome. It is possible that the arborol is entering the bilayer causing some of the water molecules to be expelled thus reducing the thickness of the bilayer and radius. Other concentrations should have been tried to verify this but so much attention was focused on creating a functioning SAXS beamline at CAMD, and later FF-TEM, that many DLS experiments were overlooked and the technique was underutilized.

DLS study on DAB-Am-32 shows a good linear fit of the D_{app} vs. q^2 (Figure 4-5) which indicates that the instrument is aligned. A hydrodynamic radius of 13 ± 0.2 Å was calculated for DAB-Am-32 using the Einstein-Stokes equation. After determining a few basic parameters for liposomes and dendrimers, the research continued using SAXS and FF-TEM.

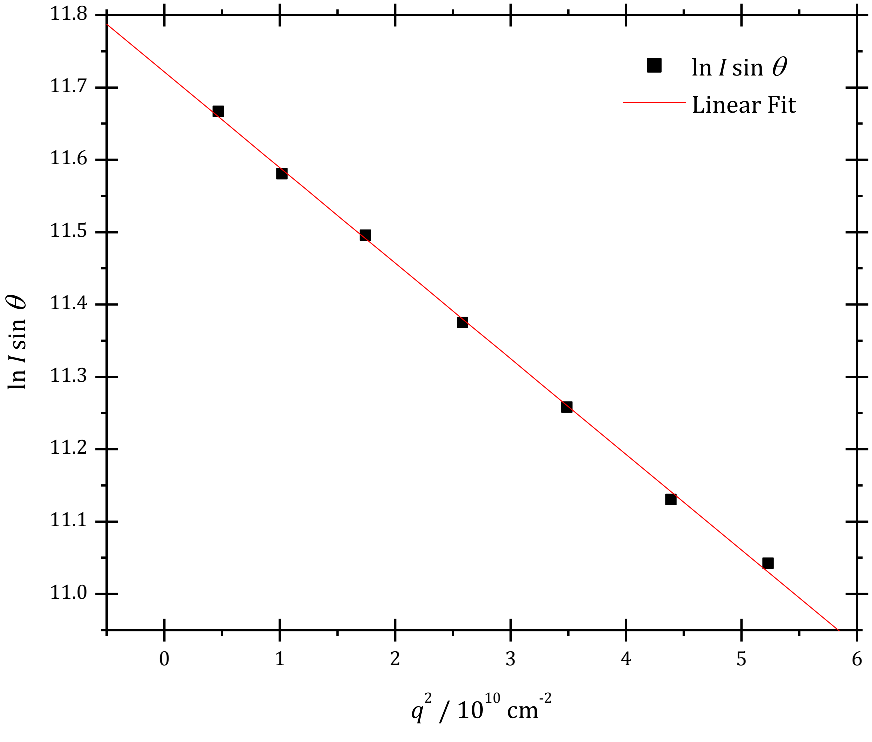

Figure 4-4 The Guinier plot of 0.29 mg/ml DOPC ULV formed using a polycarbonate filter with 100 nm in diameter pore size suggests that the R_g is 62.9 ± 0.5 nm.

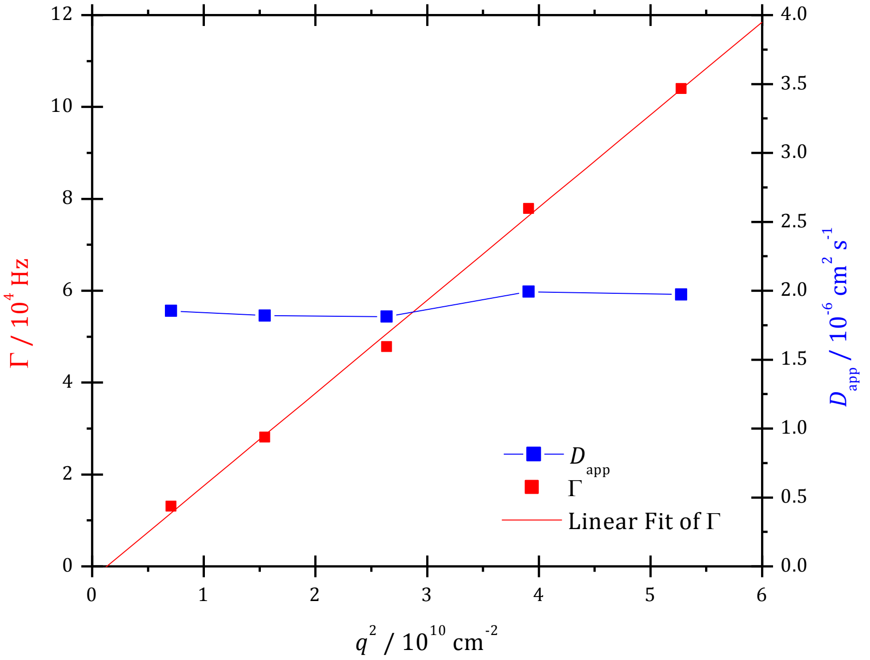

Figure 4-5 5 mg/ml DAB-AM-32 Γ and D_{app} vs. q^2.

4.4.1 SAXS of Dried Lipid and Dendrimer Films

Solution SAXS of liposome and dendrimer mixtures was not feasible the first couple of years after the beamline was installed at CAMD. This was due to low counts of scattered X-rays and problems with background subtraction including inaccurate X-ray flux and transmission measurements. In order to maximize the amount of scatted X-rays, the concentration of lipids were increased to form films. The films of DOPC and dendrimers were produced on Kapton® tape wrapped around a plastic frame. When a DOPC lipid solution is allowed to dry on a surface, it forms bilayers. The layers have a characteristic d-spacing corresponding to the distance between the layers that appears as rings on SAXS spectra, which is a consequence of averaging randomly oriented bilayers. The dissolved lipid and lipid-dendrimer mixtures in chloroform with a 10 to 1 ratio were added to the frame drop-wise and allowed to dry between applications. A total of 10 drops were added to form multilamellar bilayers. Unfortunately, this method introduced some areas where the film did not dry uniformly due to the film redissolving upon the addition of the next drop. These films were some of the first non-standard materials run on the SAXS beamline at CAMD and are summarized in Table 4-2.

Table 4-2 Peak locations from Figure 4-6 of dried DOPC and dendrimer films. For comparison, the d-spacing for bilayer staking (D) and Luzzati thickness (DB) reported by (*) Costigan et al,[87] (#) Rand and Parsegian,[86] and (§)Tristram-Nagle et al[90] are shown and the corresponding q value calculated in the second column.

Sample film	*q* of Ring (Å^{-1})	d-space D and D_B(Å)
Literature	0.098-0.103 / 0.174-0.175	60*-64# / 35.9#-36.1§
DOPC	0.112 / 0.169	55.2 / 37.1
DOPC + [9]-8	0.169	37.3
DOPC + [9]-10	0.170	36.9
DOPC + DAB-Am-32	0.144	43.7
DOPC + DAB-Am-64	0.139	45.1

The arborols and DAB-Am dendrimers insert in the layers of the lipid film and alter them. The first peak at 0.11 Å^{-1} completely disappeared as the dendrimer was added. The secondary peak at 0.17 Å^{-1} decreased in intensity until it was barely visible. It is possible that the peaks are being shifted to the right upon the addition of the dendrimer meaning the second peak of DOPC has moved outside of the *q* range of the SAXS experiment. A WAXS study could provide the support for this hypothesis and is currently underway.

4.4.2 Solution SAXS

SAXS of liposomes and dendrimers has been performed at SSRL, LNLS and CAMD. The solutions are run as soon as possible since DLS results suggest that the liposomes deteriorate with age. Complications that arise during background subtraction make solution SAXS difficult and result in truncated data as previously mentioned with SAXS and WAXS of hexagonal ruthenium macrocyclic complexes. The DOPC lipid bilayer peak occurs at about 0.1 $Å^{-1}$ in inverse space for dried films (Figure 4-6), MLV, and ULV (Figure 4-7 and Figure 4-8). This peak location will be tracked to discuss how dendrimers interact with the bilayer.

SAXS of DOPC liposomes and molar ratios of DAB-Am-32 are shown in Figure 4-7. The ULV curve has a peak at $q = 0.106$ $Å^{-1}$ or a d-space of 60 Å. The 1:1 molar ratio of ULV to DAB-Am peak is shifted to the left relating to an increase in the size or a d-spacing of 71.4 Å. The dendrimer does not have any discernible features except for the sharp decrease in the intensity due to the background subtraction. The molar ratios of 1:10 and 1:100 lipids to dendrimers do not have a peak. It is believed that the lipids in the ULV reorganize to form bilayers around the dendrimers making the resulting structures too small to see with SAXS as suggested by Mecke et al.[41,107]

A similar experiment was performed at CAMD using lower concentrations of dendrimers in order to see if the size change gradually increases with the addition of the dendrimer (Figure 4-8). The red vertical line indicates where the beamstop ends and the usable data should begin. Table 4-3 is a summary of bilayer thickness of DOPC ULVs from Figure 4-8 at different concentrations of DAB-Am-64 dendrimers. The bilayer thickness of the ULV is 63.6 Å; 6% larger than was found at LNLS. The bilayer thickness of the 23:1 ULV to DAB-Am-64 decreases in size to 61.0 Å and the size begins to increase to 66.8 Å for 3:1 and finally 74.1 Å for the 1:1 ratio. The 1:1 ratio liposome to dendrimer was also performed at LNLS but different dendrimer sizes were used. The smaller size of the lowest concentration of dendrimers could be due to the dendrimer inserting into the bilayer forcing out water and reducing the thickness. A similar result of a decrease in size was observed in the DLS data that was obtained for a 10:1 liposome to [9]-6 1-directional arborol dendrimer. More experiments on DLS and SAXS must be performed before this apparent trend can be explained.

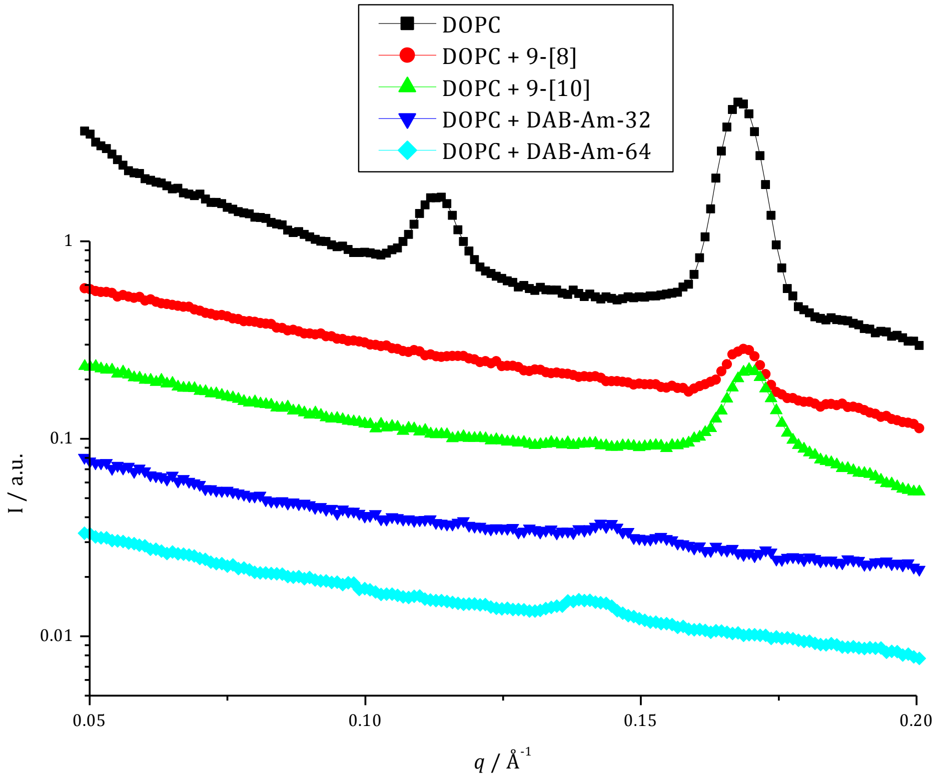

Figure 4-6 An arbitrary offset has been added to separate the plots of radially averaged SAXS data from DOPC and dendrimer films on Kapton® tape. The DOPC has two peaks before addition of a 1 to 10 molar ratio of dendrimer.

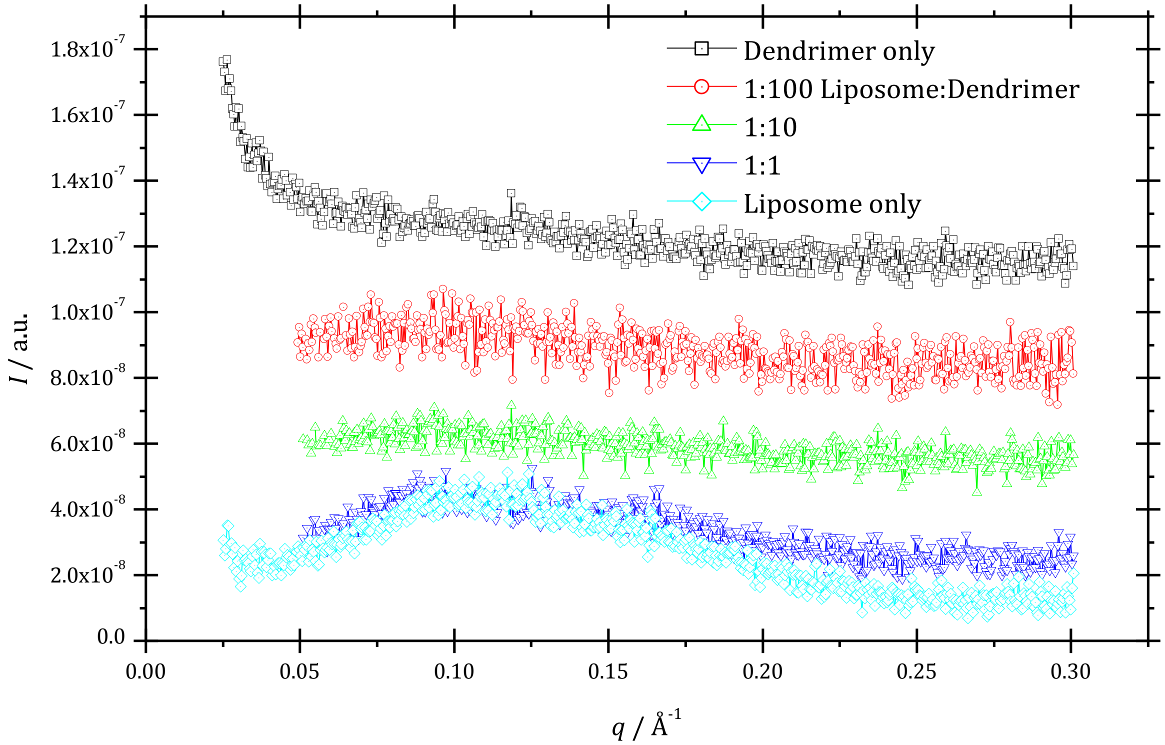

Figure 4-7 SAXS of DOPC ULV and DAB-Am-32 dendrimer performed at LNLS. The ULV spectra has a peak at 0.106 Å^{-1} and the 1:1 molar ratio of lipid to DAB-Am peak is shifted to the left at 0.088 Å^{-1}. This correlates to a d-spacing of 59.3 and 71.4 Å, respectively.

Table 4-3 Peak location in inverse space and corresponding d-space of DOPC ULVs, DAB-Am-64, and mixtures in PBS at pH 7. The 23:1 liposome to dendrimer concentration is smaller than the original ULV, but the size increases as dendrimer concentration increases.

Sample	**Peak at *q*, Å^{-1}**	**d-space, Å**
DOPC ULV	0.099	63.6
23:1 ULV to DAB-Am-64	0.103	61.0
3:1	0.094	66.8
1:1	0.088	71.4
DAB-Am-64	NA	NA

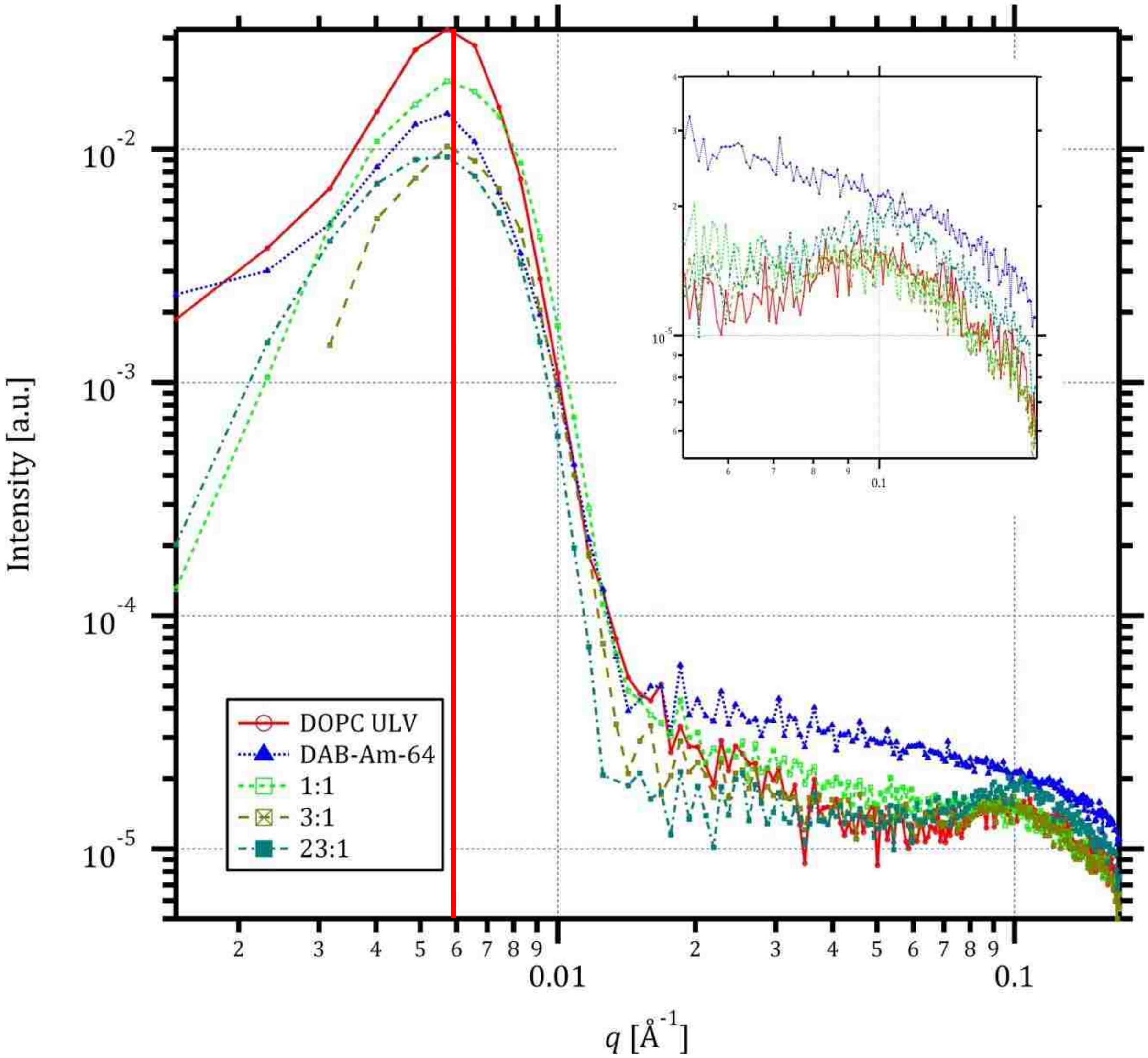

Figure 4-8 SAXS plots of background-subtracted runs of aqueous samples of DOPC ULV, DAB-Am-64, and mixtures thereof in capillaries. The red line at q = 0.006 Å^{-1} is the minimum q allowed due to the beamstop. Parasitic scattering contributes to the large initial slope of the scattering curve.

4.4.3FF-TEM of Liposomes and Dendrimers

Initial attempts of imaging liposomes using FF-TEM at the LSU Vet School were unsuccessful with replicated samples resulted in images of ice or a smooth surface of vitrified PBS, but no ULVs. To verify the presence of liposomes, even though DLS had already confirmed this, a TEM sample of ULVs was prepared by staining with 0.5% uranyl acetate. The TEM images showed the once spherical liposomes formed disc-shaped structures after drying. The average diameter of the discs was 120 nm, which seemed appropriate for spheres of 100 nm diameter that were allowed to dry.

The stained TEM images proved the presence of liposomes in the sample and it seemed that the concentration of vesicles in the sample was too low to acquire a FF image. Multilamellar vesicles were made since they provide a larger target and the sample was centrifuged for 30 seconds at 1000 RPM to form a pellet at the bottom of the sample vial. A sample from the concentrated MLVs was used to make a FF replica and was successful. Figure 4-10 shows a MLV with several bilayers visible.

The use of more concentrated samples increased to probability that ULVs would be visible along the fracture plane created by the FF technique. One concern with raising the concentration is inducing vesicle fusion and aggregation. Fortunately, this did not occur and many images of liposomes were attained. The ULVs in Figure 4-11 have an average diameter of 90 nm. The addition of DAB-Am-64 to form a 10:1 liposome to dendrimer solution (Figure 4-12) caused the size to decrease to about 70 nm. The decrease in size for 10:1 ratio of liposome to dendrimer solutions was previously observed in DLS and SAXS measurements. Increasing the dendrimer concentration to a 1:1 molar ratio forced the liposomes to aggregate as shown in Figure 4-13.

The micrographs of DOPC liposomes with DAB-Am appear rougher. In Figure 4-14, the three images are compiled for comparison with the ULVs at the top (A), 10:1 molar ratio of ULVs to DAB-Am-64 in the middle (B), and 1:1 molar ratio of ULVs to DAB-Am-64 at the bottom (C). The "bumps" exhibit hexagonal packing and average 6 nm in diameter. This phenomenon could be the result of dendrimer addition or a coincidence of fracturing along the interior of the bilayer as in Figure 4-10 of the MLV. DLS could be used to track changes in D_{app} upon the addition of dendrimers. If it increases, the roughness is a result of the dendrimers and they are associating with the surface of the liposome.

4.5Conclusions

The work on SAXS and FF-TEM provides evidence of the liposome and dendrimer interaction via size changes in the lipid bilayers. The size of the liposome decreases with an addition of 1:10 or less molar ratio (1×10^{-6} moles per liter) of dendrimers. At higher concentration of dendrimers, regardless of their M_w, the liposome increases in size or bilayer thickness until aggregation occurs. The liposome maintains its spherical shape until aggregation is induced or the lipids reform bilayers around the dendrimers. Unfortunately, the dendrimers studied where too small to be observed with FF-TEM so the visual confirmation of dendrimers associating with the surface of the liposome *in situ* was not obtained. Energy dispersive X-ray spectroscopy (EDS) could be used to determine if the dendrimers are associating with the liposome in dried samples.

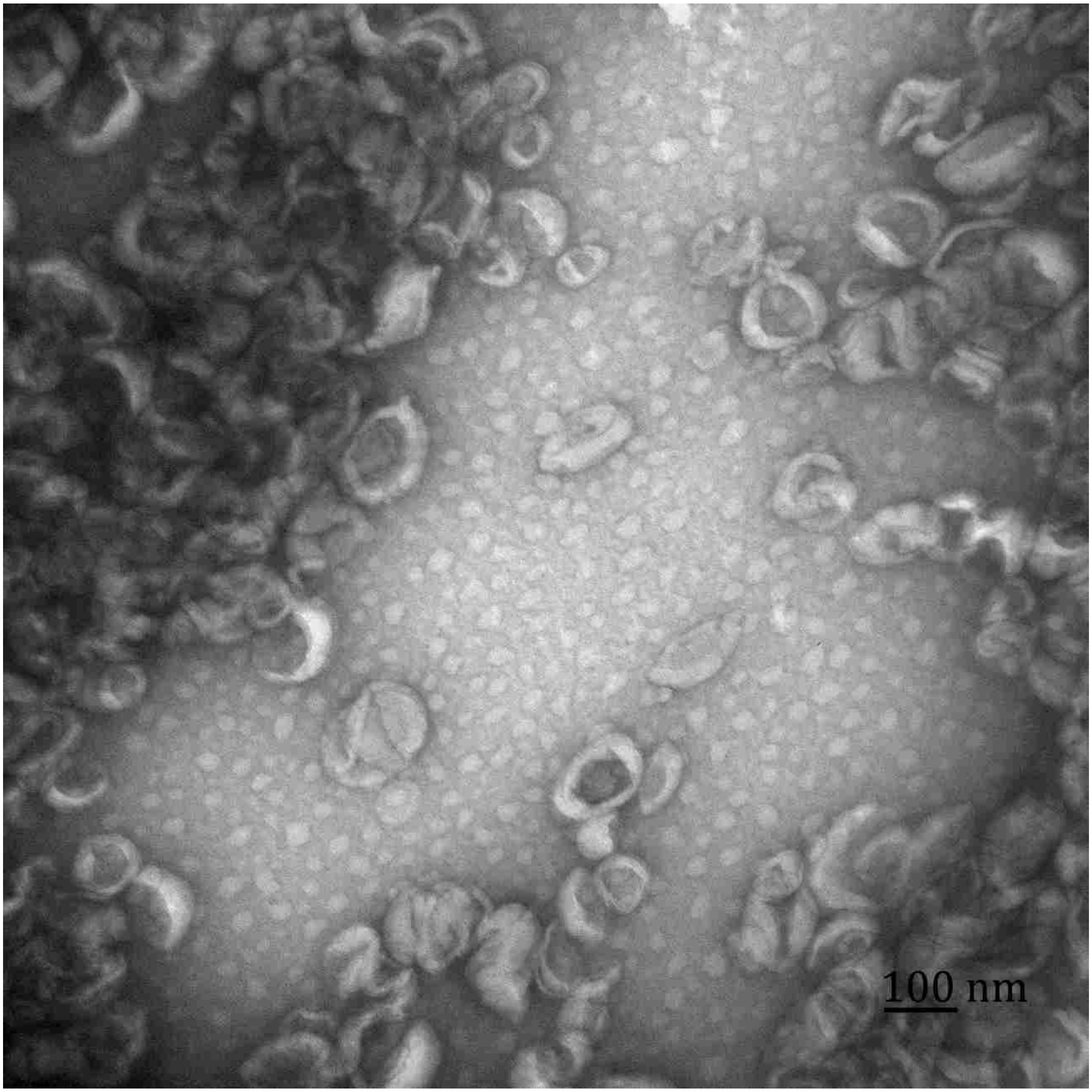

Figure 4-9 TEM of 100 nm DOPC liposomes stained with 0.5% uranyl acetate. The liposomes form discs after drying ranging from 80 to 150 nm across, an average of 120 nm.

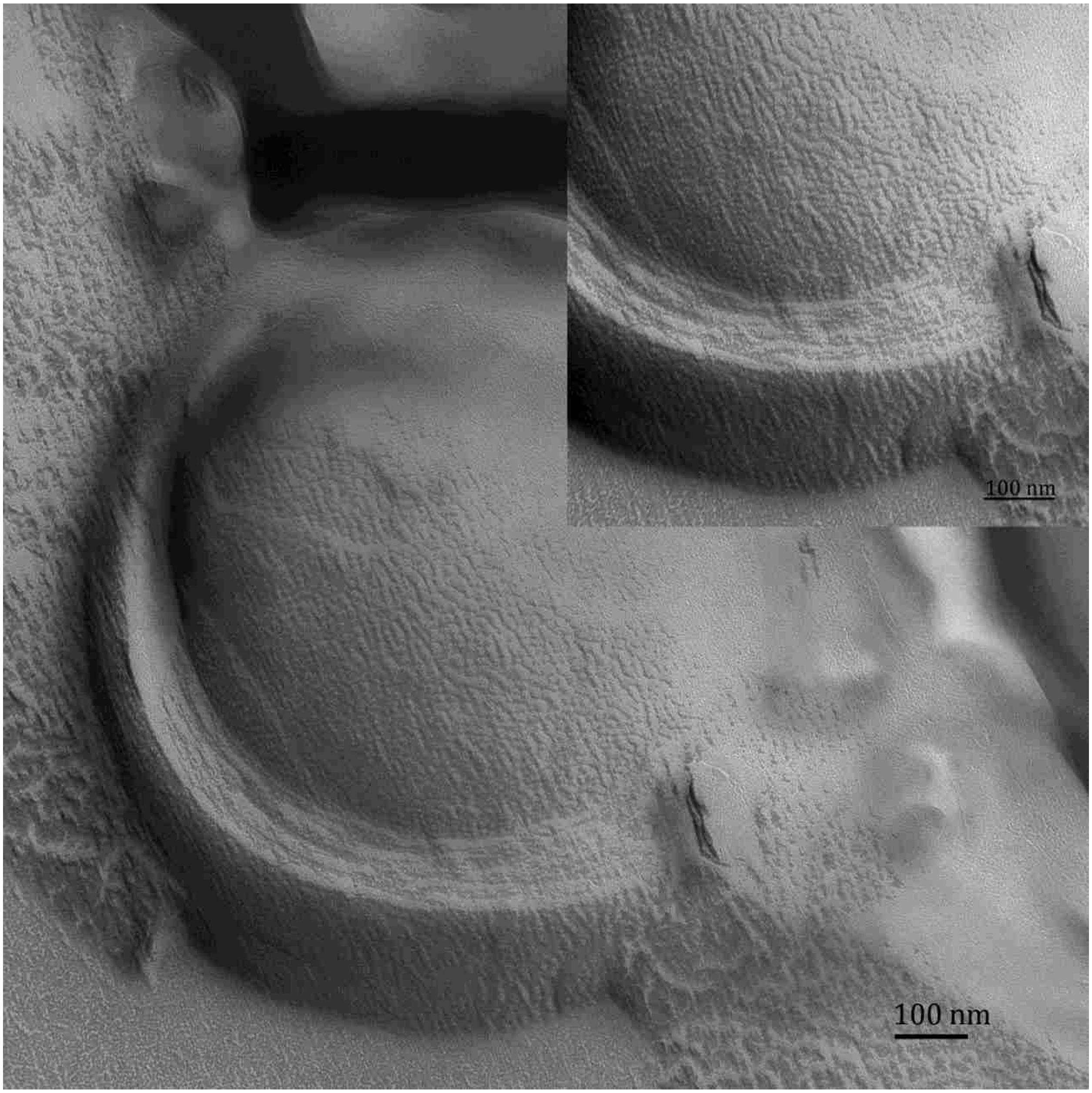

Figure 4-10 Giant multilamellar vesicles of DOPC with multiple bilayers visible. The sample was produced from the concentrated pellet of MLV that formed in the bottom of the sample vial after centrifugation.

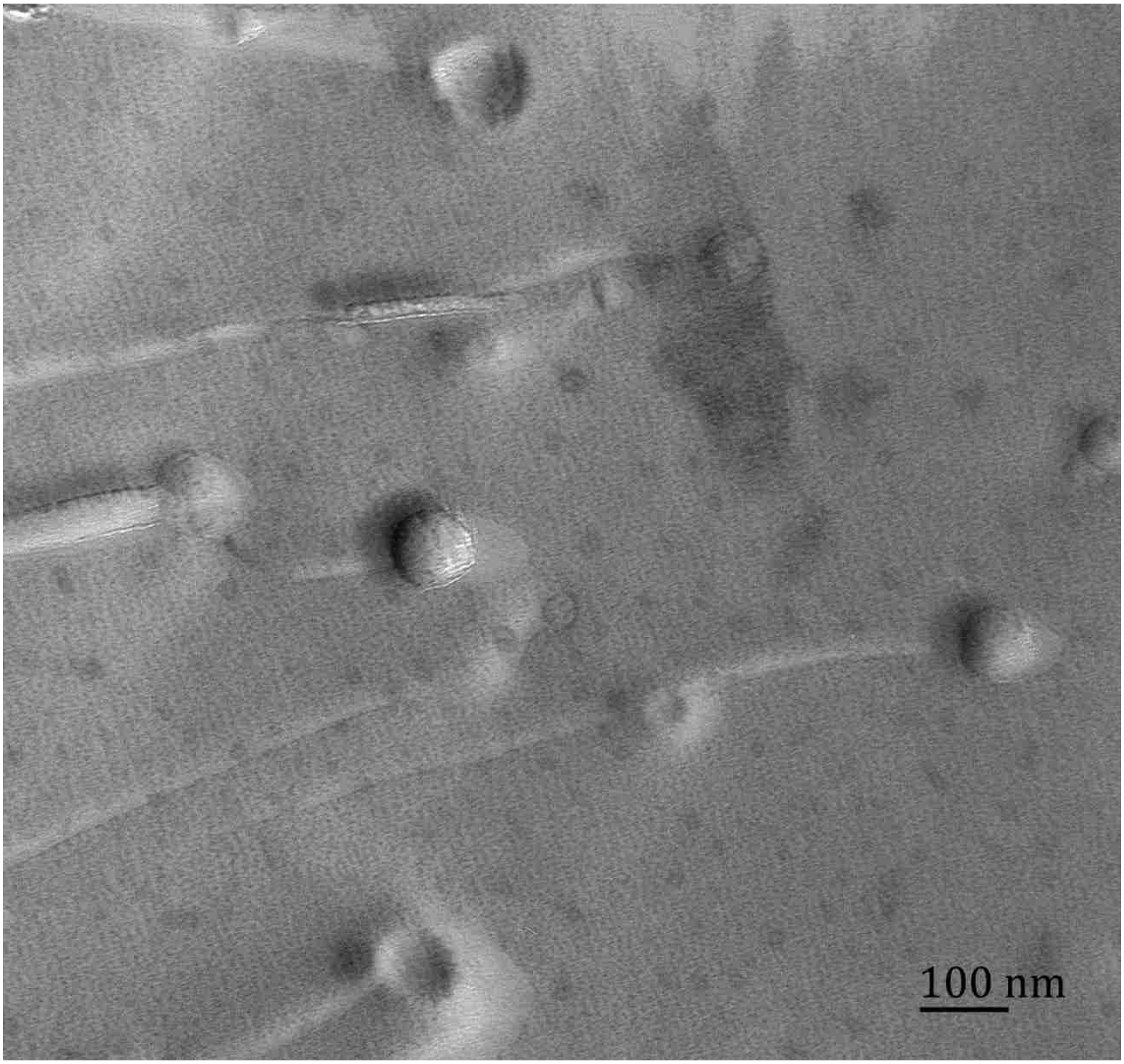

Figure 4-11 FF-TEM of 100 nm in diameter DOPC ULVs.

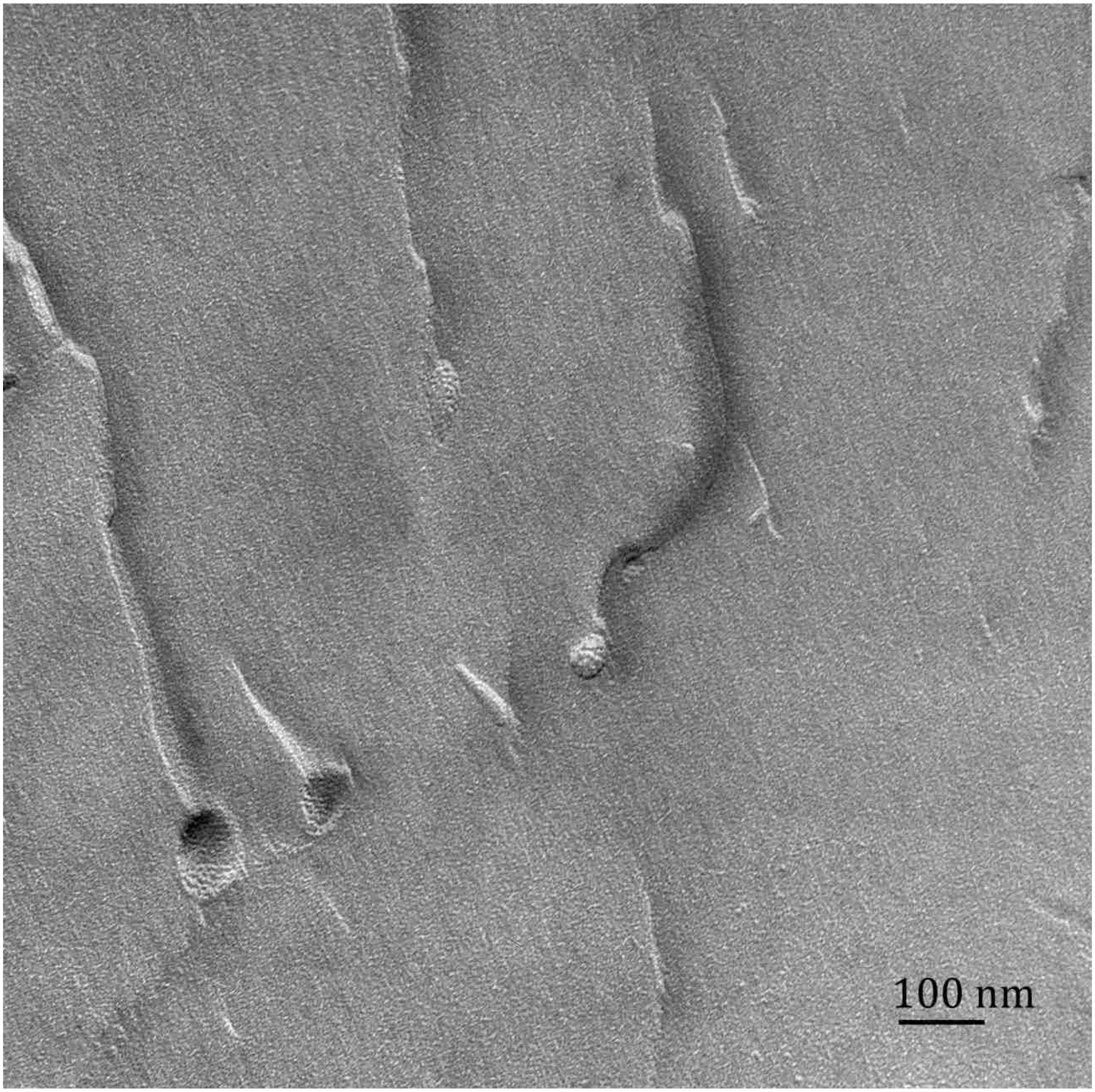

Figure 4-12 FF-TEM of 100 nm DOPC ULVs mixed with DAB-Am-64 with a 10 to 1 molar ratio.

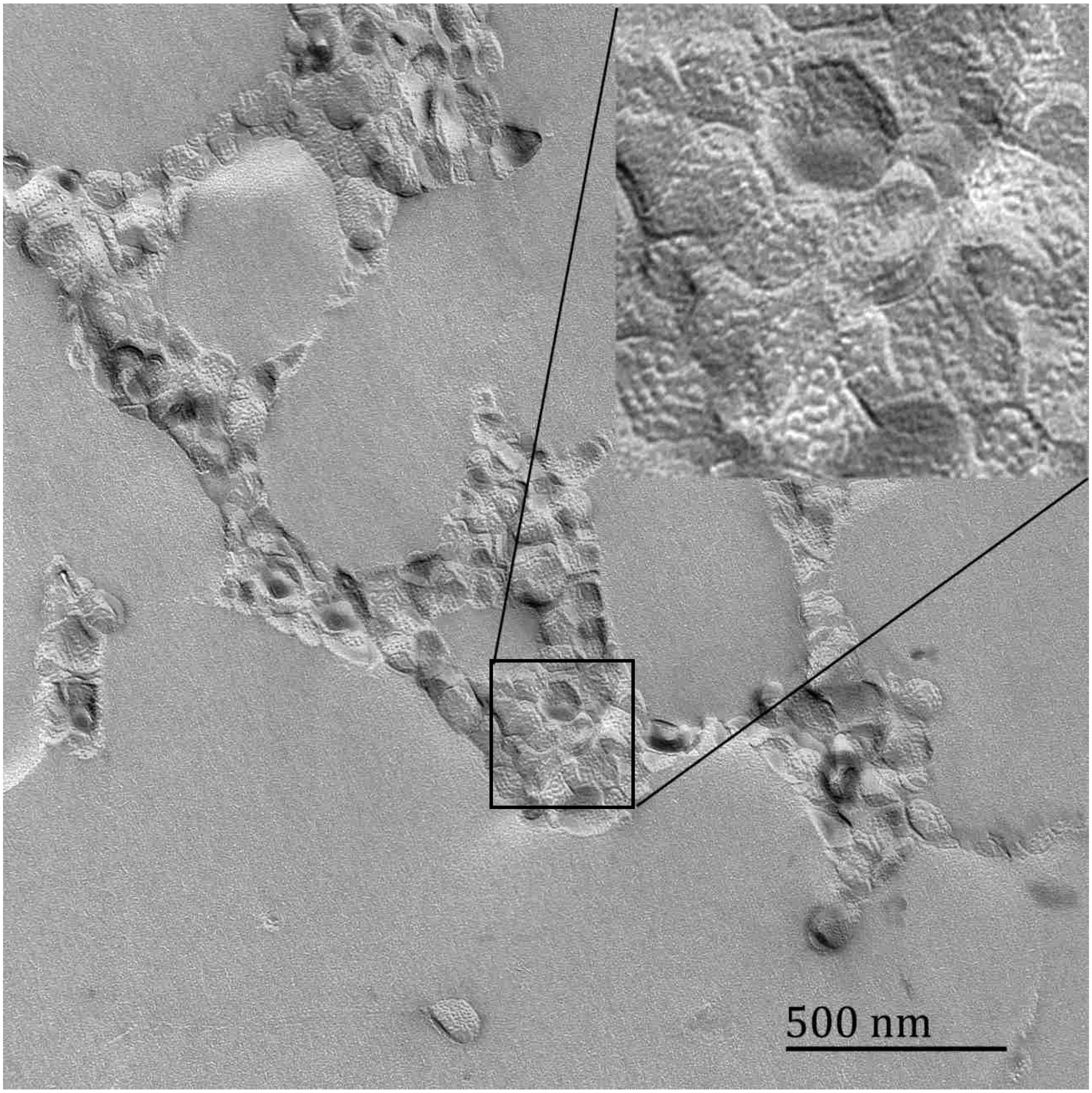

Figure 4-13 FF-TEM of 100 nm DOPC ULVs mixed with DAB-Am-64 in a 1 to 1 molar ratio. There is more aggregation but the individual liposomes can still be seen.

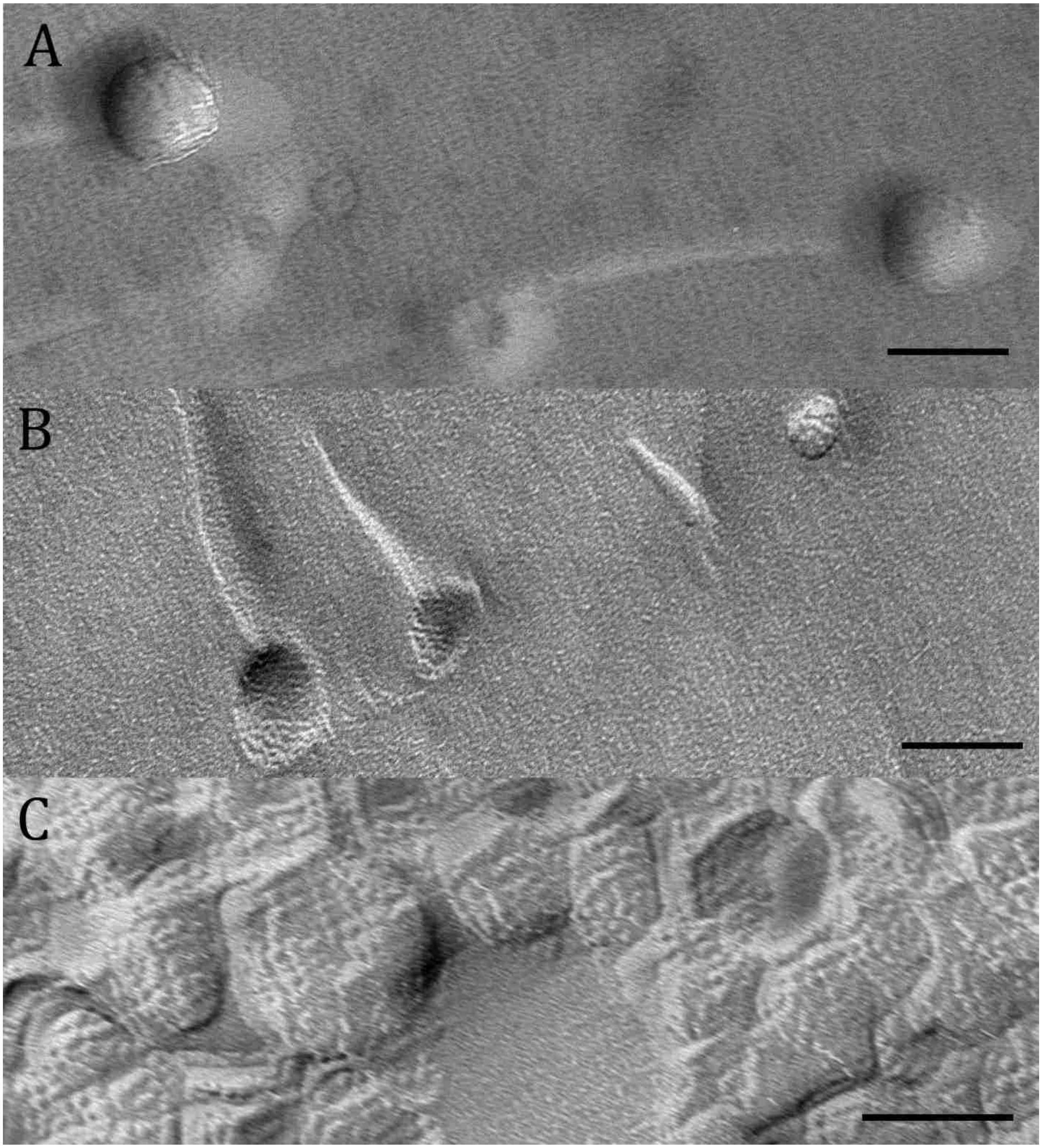

Figure 4-14 A side by side comparison of ULVs (A), 10:1 mole ratio of ULVs to DAB-Am-64 (B), and 1:1 mole ratio of ULVs to DAB-Am-64 (C). The surface of the liposome appears rough after the addition of the dendrimers. The black scale bars are 100 nm.

The decrease in liposome size at low concentrations of dendrimer is believed to be an affect of the absorption of dendrimers to the surface of the liposome as shown in Figure 4-15. The dendrimer is not completely enveloped by lipids though the extra lipids necessary to wrap around the dendrimers come from the liposome bilayer causing the liposome to become smaller. This is supported by Mecke et al[41] work showing lipid bilayers forming around the dendrimers, but this predominately occurs at much higher dendrimer concentrations. As the concentration of dendrimer increases, the dendrimers associating with the surface of the liposome cause an increase in the overall size until aggregation takes place.

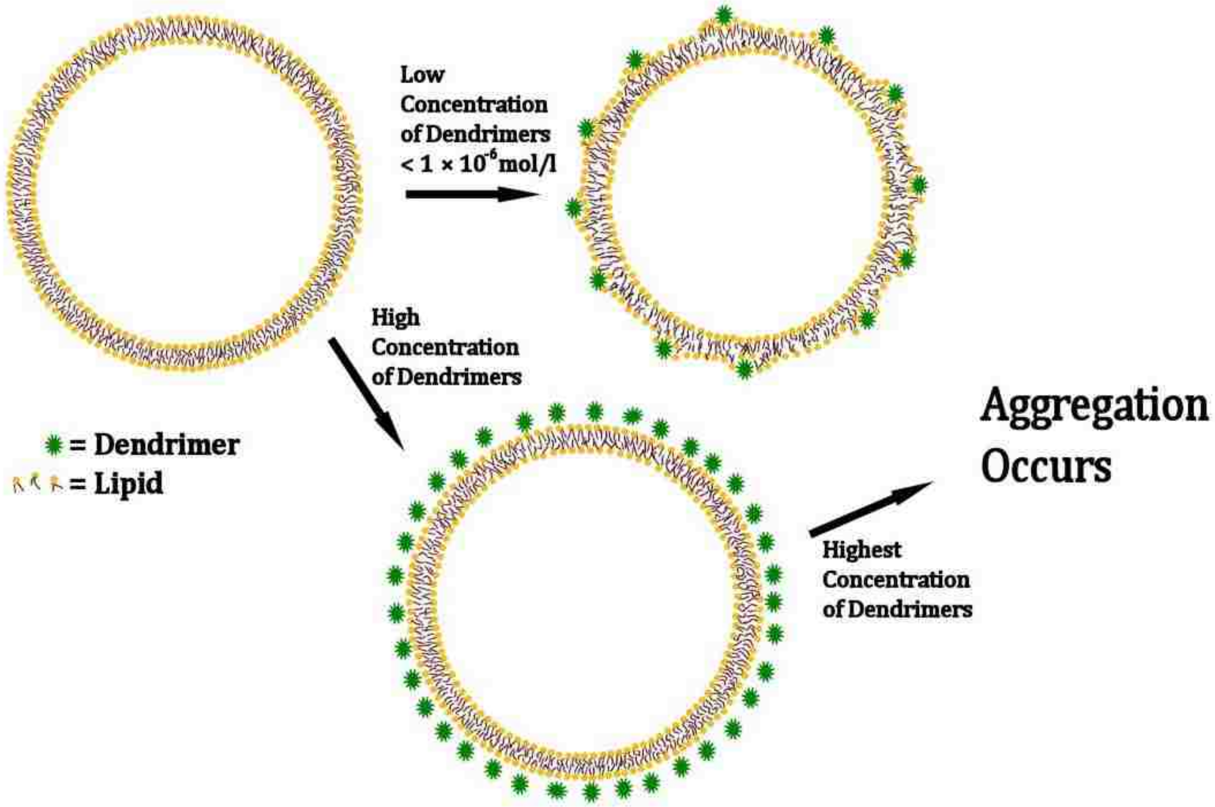

Figure 4-15 Pictogram of the interaction between liposome and dendrimers. When less than 1 × 10^{-6} moles per liter is added to the solution, the liposome becomes smaller due to lipids wrapping around the dendrimer at the surface of the liposome. As more dendrimer is added, the dendrimer populate the surface of the liposome.

A series of DLS experiments are envisioned to learn about the surface of the liposome and track other variables like temperature and what effects changes in salt concentrations could have on liposome and dendrimer interaction. Of course, obtaining the best possible SAXS spectra would go a long way in providing much of the information that has been obscured by inaccurate X-ray transmission assumptions and bad background subtraction routines. Scientists have spent lifetimes studying liposomes and there is still a cornucopia of knowledge to gain.

APPENDIX A SMALL ANGLE X-RAY SCATTERING BEAMLINE DESIGN

Several improvements to the SAXS beamline at CAMD included designing new parts that were fabricated by the College of Basic Science, Department of Physics and Astronomy, and Chemical Engineering machine shops at LSU. Most sketches of the desired part were drafted in TurboCAD or similar design program before submission for fabrication. Several views are provided with measurements for each part and the preferred materials are listed on the technical drawing.

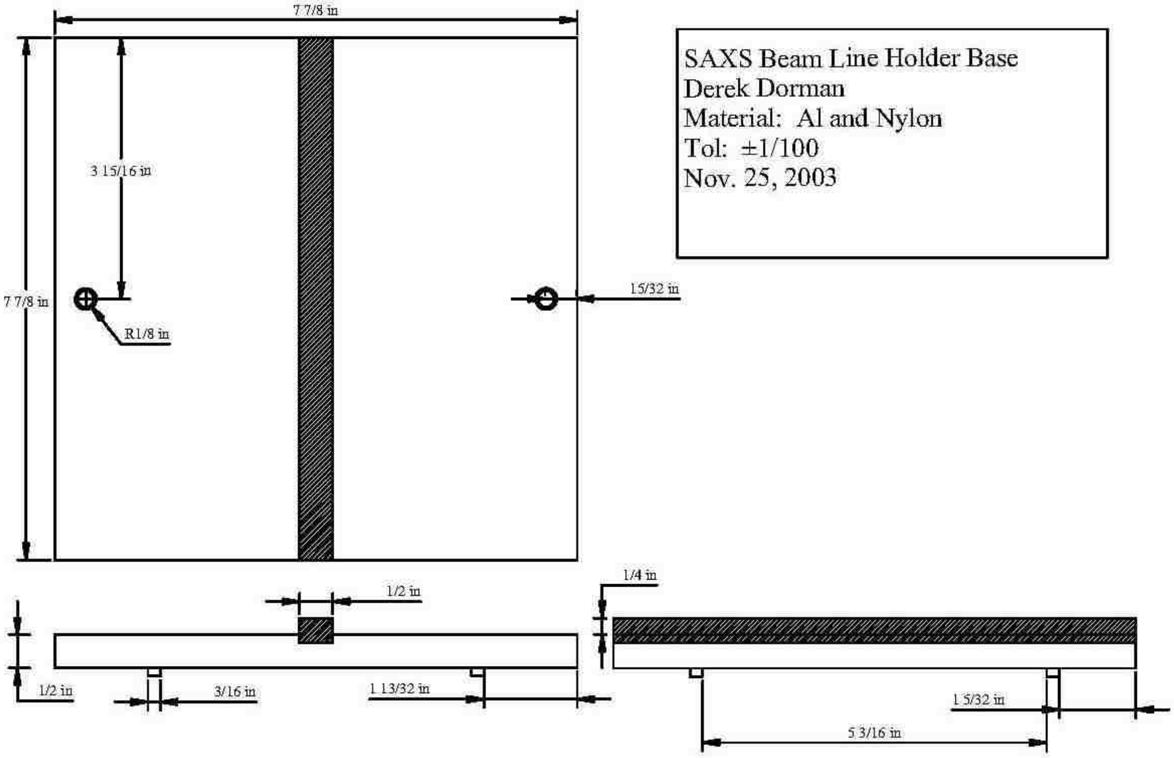

Appendix Figure A Base for beamline pipe supporter.

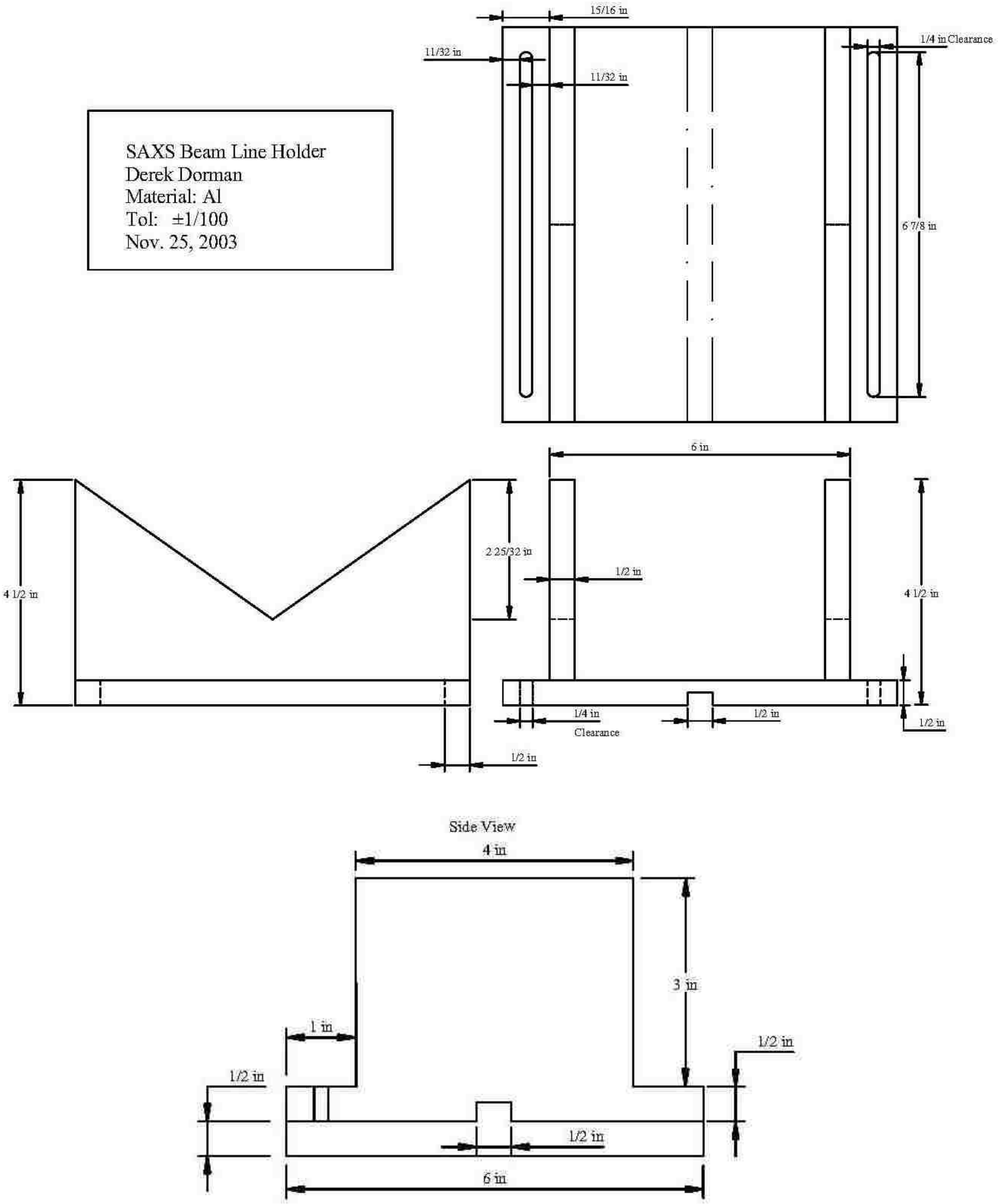

Appendix Figure B Beamline pipe support that sits on base shown in Appendix Figure A. The parts are designed to allow translation of the beamline flight tubes in the x, y, and z directions and are secured with bolts once the final orientation is achieved.

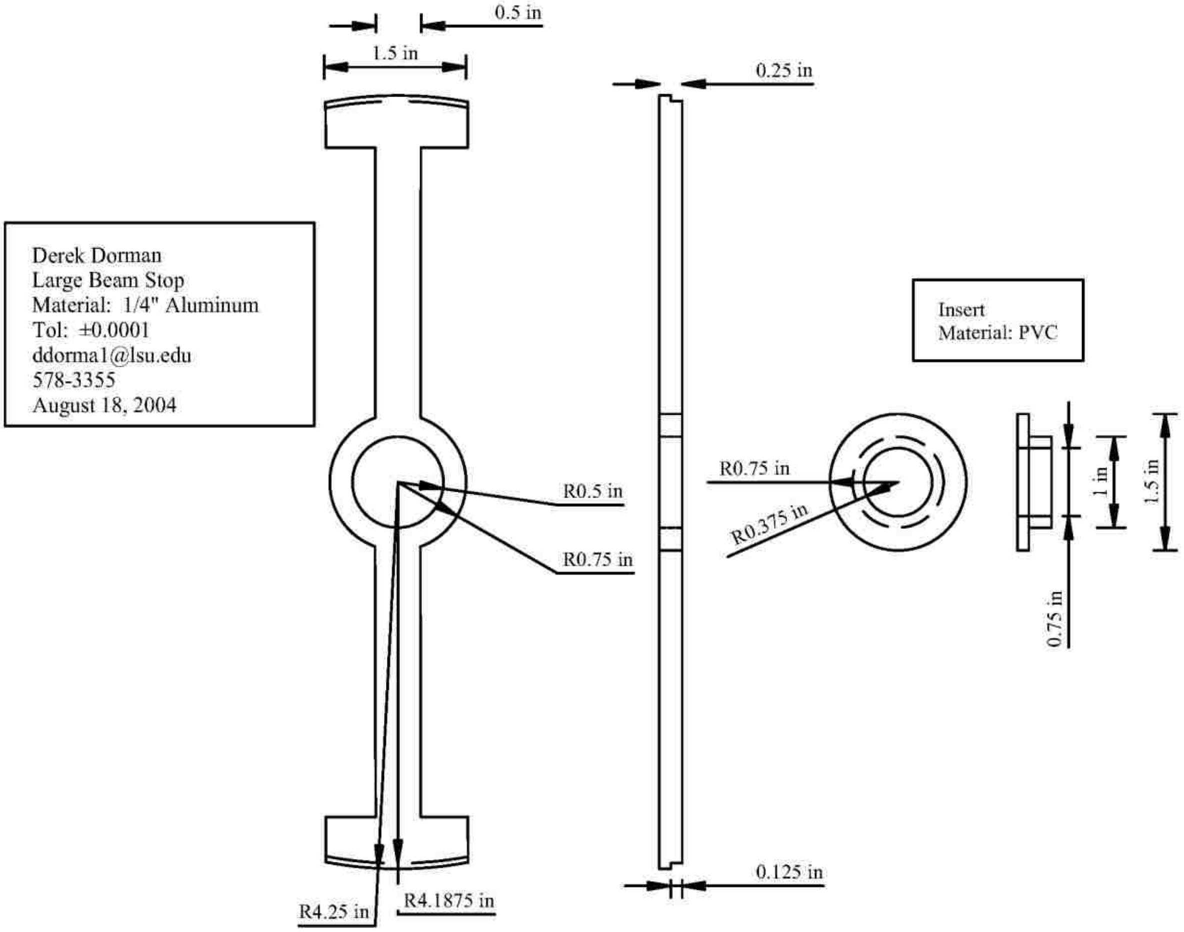

Appendix Figure C Large beamstop designed to hold samples in the center of the circular opening in the back of the sample chamber. Samples can be mounted on the PVC insert that snaps on to the Al beamstop. Several inserts were produced allowing samples or attenuation foils to be swapped out easily.

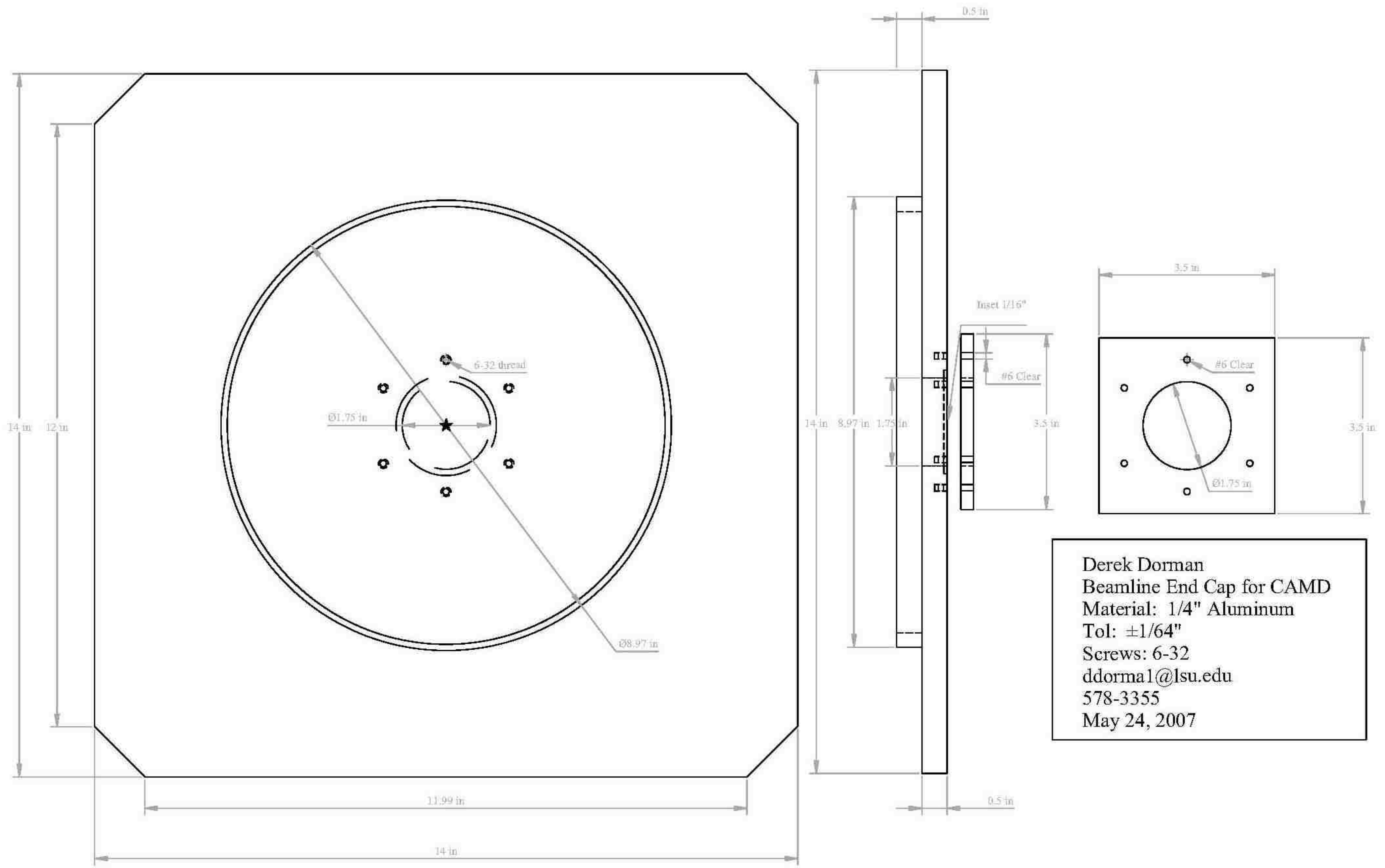

Appendix Figure D Vacuum tight cover with Kapton® window used in place of the detector while maintaining the vacuum of the beamline. This is useful to safely position the beamstop using the X-ray eye.

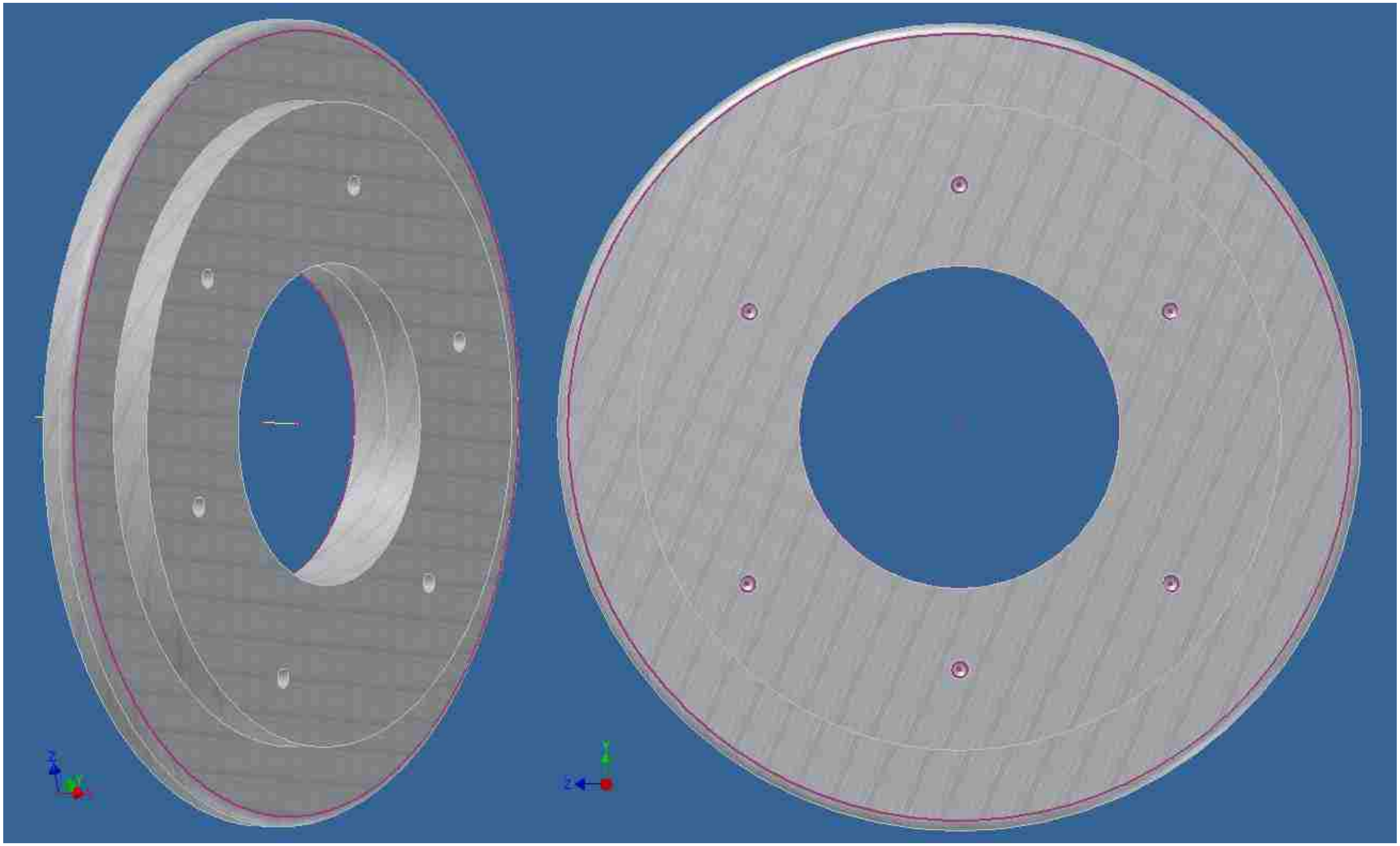

Appendix Figure E Aluminum cover with Kapton® window for the back of the sample chamber for maintaining a vacuum in the flight tubes while leaving the sample as exposed to the atmosphere.

APPENDIX B FREEZE FRACTURE REPLICATION STANDARD OPERATING PROCEDURE (SOP)

1) Fill the small Dewars, including the one containing the metal pipe with the small cryogen reservoir, from the large Dewars on the floor. If they are empty, then take liquid nitrogen directly from the low pressure liquid nitrogen tank before it is connected to the Balzers BAF 400.
2) Set up the specimen table on the table holder making sure that you tighten by turning clockwise. There is a spring with tines on the specimen table that holds the gold stubs to the specimen table. Put the lever in place and turn so that the tines are not touching the specimen table.
3) Place the specimen table attached to the table holder into the nitrogen container or Styrofoam box and fill it with liquid nitrogen.
4) Once the cryogen container in the Dewar (the pipe where the cryogen is placed) is cold enough, fill it with Freon or other cryogen and let it freeze.
5) Turn on the Quartz Crystal Thickness Monitor QSG 301 since it takes several minutes for the quartz crystal microbalance (QCM) to stabilize.
6) Turn on the main power to the Freeze Etching Unit Control BMS 101 and begin to cool the table by pressing the temperature adjust button.
7) In a Petri dish, place a piece of filter paper and the gold stub specimen carriers that will be used.
8) Fill the three gold stubs with a small drop of sample making sure that each sample is about the same height.

9) Use the metal rod to melt the Freon in the cryogen container in the Dewar enough to completely submerge the sample.

10) Grasping a gold stub with a pair of tweezers, quickly plunge the sample in the liquid cryogen (2-3 seconds), then dunk in the $N_2(l)$ in the Dewar surrounding the cryogen container, and finally place the gold stub on the specimen table, which is fully submerged in $N_2(l)$, under one of the tines.

11) Make sure that the $N_2(l)$ level in the Styrofoam box remains above the samples on the specimen table.

12) Repeat steps 9 and 10 on the remaining samples.

13) Once all the samples are on the specimen table and under the tines, remove the specimen table spring lever.

14) Move the Styrofoam box to the shelf on the Balzers BAF 400. Continue to keep the box filled until you are ready to insert the specimen table into the vacuum chamber.

15) Turn on knife cooling on BMS 101. Wait for cold stage and knife to reach the right temperature.

16) Ensure that the knife is out of the way for insertion of the specimen table by rotating the hand wheel under on the left side under the vacuum chamber.

17) Chill the tip of the manipulator rod in the Styrofoam box's $N_2(l)$. Once there is little or no boiling at the tip of the manipulator rod, it can be attached to the specimen table.

18) While working under $N_2(l)$, connect the manipulator rod to the specimen table by pressing the rod into the table and turning the rod an ⅛ of a turn.

19) Prepare to insert into the vacuum chamber, by releasing the specimen table from the table holder with a ¼ turn counterclockwise keeping the samples submerged. (Note: It is important to minimize the time that the samples are exposed to air. The next 4 steps should be performed quickly.)

20) All switches should be in the off position on the ALC 101 box above SV1. Vent the interlock by flipping the vent switch to "On" for 3 seconds then return the switch to the off position.

21) Remove the plug from the specimen interlock.

22) Quickly insert the specimen table and the manipulator rod into the interlock.

23) Open the pump valve as soon as the specimen table is inserted by flipping the switch labeled "Pump" to the "ON" position. Once the mechanical pump quiets down, close the pump valve (turn off).

24) Now you can open the SV1 valve and insert the specimen table onto the vacuum chamber and attach it to the cold stage under the cold shroud. It is imperative that the manipulator rod is kept parallel to the floor. The rod can act as a lever and any torque or twist on it while the specimen table is being inserted could break the vacuum. To protect the cryo pump, the system will shut the cryo pump valve and could require a long wait before the vacuum can be returned.

25) Rotate the rod ¼ turn clockwise to lock the specimen table on to the cold stage and ⅛ of a turn back to release the rod from the specimen table

26) Pull the rod straight back until you can see the tip through the window on top of the specimen lock chamber.

27) Once you can see the tip, close SV1 by flipping the switch to the off position.

28) Vent to remove the rod and close the vent valve.

29) Return the plug and pump down the specimen lock chamber by opening the pump valve.

30) Close the pump valve when the mechanical pump quiets down.

31) Turn on the Microtome Movement Control BMB 101.

32) Before cutting the samples with the knife, use the binoculars to place the knife edge just behind the three samples on the specimen table/cold stage by advancing the knife. There is a button for up and one for down on the microtome control unit.

33) Use the knife controls to position the knife where the samples should be cut. (Note: The samples should be cut at the same time. Make sure the knife is low enough to cut all three samples, but not so low that it will hit the gold stubs or the cold stage. You can move the knife back and forth a little to make it easier to see where the knife will cut.)

34) Once the knife is at the desired location, back up the knife and with a smooth motion, turn the hand wheel so that the knife cuts through all samples. If you don't cut them all, the knife can be lowered and another cut can be made. It is best to only cut once.

35) Continue to rotate the knife so the back of the microtome is over the samples.

36) If etching of the samples is desired, this is the time to do so. They will sublimate during the time between now and the platinum is deposited. Etching is not necessary to produce good samples, but could help with contrast depending on the type of samples being replicated. Remember that all samples are getting the same treatment.

37) Turn on the gun controls (if they are not already on) by flipping the “Mainz” switch on the Evaporation Control Unit EVM 030 to the “ON” position.

38) Degas each gun by selecting the gun and pressing the corresponding degas button. Each gun should be degassed before deposition if this has not been done previously. Degassing should be performed anytime the guns are exposed to the air. The guns should have been degassed when they were replaced and the vacuum chamber reached the desired pressure.

39) Zero the QCM in preparation of depositing metal. This takes a light touch! The zero knob is used to dial in the correct frequency needed to zero the scale. The needle on the gauge will pass through a minimum if it is being turned in the right direction. Once the needle passes through is minimum, it will begin to increase again as the knob is turned more. If the knob is turned too much, it will be difficult to determine the correct direction to turn the knob. The knob must be turned very, very slowly. It may be difficult to tell if the knob even moved but the needle on the gauge will move, so watch the gauge.

40) Make sure the platinum-carbon gun (gun 1) is selected / active by pressing the “Gun 1” button above the word “Evaporation” on the control panel. Approximately 2 nm of Pt should be deposited first followed by 200 nm of carbon. Platinum is 10 times heavier than carbon so the scale of the QCM will read 20 (on the red scale for current settings) when 2 nm of Pt has been deposited.

41) Turn the voltage to gun 1 on by pressing the “Gun 1” button under the words “High Voltage.” Remember that the back of the knife arm is covering the samples. Be ready to

move the microtome back to expose your samples once the correct voltages have been reached on the display.

42) Turn off gun 1 once 2 nm has been deposited (that is 20 on the QCM red scale) by pressing the “OFF” button below “High Voltage.”

43) Cover the samples again with the back of the knife arm.

44) Select the carbon gun by pressing the gun 2 button above the word evaporation on the control panel.

45) Zero the QCM again.

46) Turn the voltage to gun 2 on by pressing the “Gun 2” button under the words “High Voltage.” Remember that the microtome is covering your samples. Be ready to move the microtome back to expose your samples once the correct voltages have been reached on the display. Covering your sample is not as important for carbon deposition.

47) Once the QCM reads 20 on the red scale, turn off the high voltage to gun 2.

48) Replication of the samples is complete. This is a good time to make sure the supplies for washing the replicas are ready or at least nearby. The specimen table holder should be ready to receive the specimen table and the well plate should be prepared with the appropriate cleaning and rinsing solution.

49) Everything can be turned off now unless more samples are going to be replicated.

50) Vent the specimen interlock chamber and insert the manipulator rod.

51) Pump down the interlock chamber and turn off the pump once the pump quiets down.

52) Open SV1 and retrieve the specimen table with the manipulator rod.

53) Turn the manipulator rod to unlock the specimen table from the cold stage and extract the specimen table until you see it through the window on top of the specimen interlock chamber.

54) Close SV1 by flipping the switch to the off position.

55) Vent the specimen interlock chamber and remove the manipulator rod and specimen table.

56) Replace the plug and pump down the specimen interlock chamber for a few seconds then turn off the pump.

57) Attach the specimen table to its holder and remove the manipulator rod.

58) Lift the tines with the spring lever.

59) Remove a gold stub from the specimen table and place it in contact with the meniscus of the cleaning solution in the well plate. Do not submerge the gold stub yet. Only place the very edge of the gold stub in contact with the solution until the frozen sample thaws.

60) Allow the gold stub and sample to completely thaw and slowly release the gold stub into the well.

61) The goal is to float the replica on the surface of the cleaning solution. If the replica sinks, do not worry; it can be saved.

62) Repeat steps 52 through 54 until the last gold stub is in the cleaning solution. Make sure you remember which sample is in each well.

63) The replicas can stay in the cleaning solution for as long as it takes to remove the entire sample from the replica, but they are not be allowed to dry out. A Petri dish can be used

to cover the well plate to prevent the replicas from drying out. The other wells in the plate should be filled with water if the replicas are going to be left in the cleaning solution for a long time. The samples can be cleaned in bleach, which is best for biological samples, or just rinsed in purified water.

64) Several tweezers, metal hoops and glass pipettes that have been melted to form a glass bead at the tip can be used to manipulate the replicas. The eyelash brush is useful when coaxing sunken samples onto a grid or carefully unfolding replicas. It is best to use some binoculars if it is necessary to move the replicas much.

65) Once the replicas are on the grid, dry off the grids by dabbing them on a piece of filter paper. Place the grid straight down on the filter paper. The replica may move to the edges of the grid if one side touches before the other. Also use a piece of filter paper to dry the water that is between the tines of the tweezers.

66) The grids can be placed under a piece of tape across a Petri dish with a piece of filter paper in the bottom or in a grid holder. Grid holders are also a good way to store grids until imaging time.

APPENDIX C SERVICING THE CARBON ELECTRON GUN SOP

1) Check that the nitrogen cylinder is turned on and regulated at 80 psi. The ALC 101 valve controller should be turned on if it is off and all of the switches to the valves in the "off" or down position. Make sure the gun interlock chamber collar is in place, holding the cover and electron gun extraction rod securely.
2) Flip the pump switch to "ON" or up to evacuate any air from the interlock chambers. A red light next to the word "pump" will light up and the V1 light will go off. When the mechanical pump is quiet (or if it does not make any noise), turn off the pump by flipping the switch back down.
3) Open SV2 by flipping the switch to "On." The SV2 light comes on indicating that the interlock valve is open.
4) Insert the gun interlock chamber extraction rod to retrieve the carbon electron gun. The rod may have to be adjusted slightly to go all the way in. It can be felt when the rod contacts the gun holder and when it seats itself. There should only be ¼ inch of the silver rod visible when it is fully inserted.
5) Twist the rod ¼ turn clockwise to attach it to the gun holder. The rod should not turn any more. If the rod tip does not engage the gun holder within ¼ turn, then the rod is not all the way in. This should correct itself as it will fall into place as the rod is turned and adjusted.
6) Pull straight out as far as you can and hold. Use all of your might, but make sure the collar is in place so you don't break the vacuum.
7) Close SV2 by flipping the switch to its down position.

8) Vent the interlock chamber by flipping the vent switch up to its “ON” position. After a few seconds, flip the switch back down to close the valve. A hiss will be heard as room air or nitrogen from the liquid nitrogen tank breaks the vacuum. Close the vent valve when it stops. The vent valve breaks the vacuum on both interlock chambers, so the plug in SV1 should become loose or pop out as well. If it is connected to the liquid nitrogen tank and the liquid nitrogen is on, this will occur quickly. It takes longer otherwise. Of course, if you forgot to turn on the liquid nitrogen and it is connected to the tank, nothing will happen and the vacuum in the interlock chamber will remain.
9) Loosen the collar and extract the carbon electron gun. Remove the gun from the rod. A pair of cloth or rubber gloves should be worn when touching the electron guns.

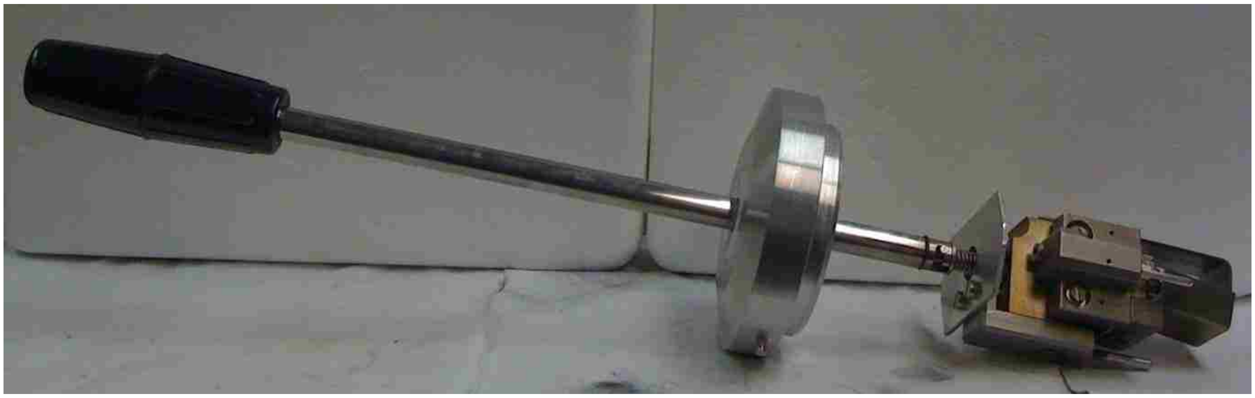

Appendix Figure F Carbon gun attached to the gun extraction rod.

10) Replace the rod and cap on the interlock chamber.
11) Open the pump valve and close once the mechanical pump quiets down.
12) Remove the gun holder from the electron gun. There is one large hex bolt holding it on.
13) Remove the Wehnelt shield with the deflector plate. Appendix Figure G shows the carbon gun (center) with the Wehnelt shield and deflector plate (right) and carbon gun holder with safety shield (left) removed.

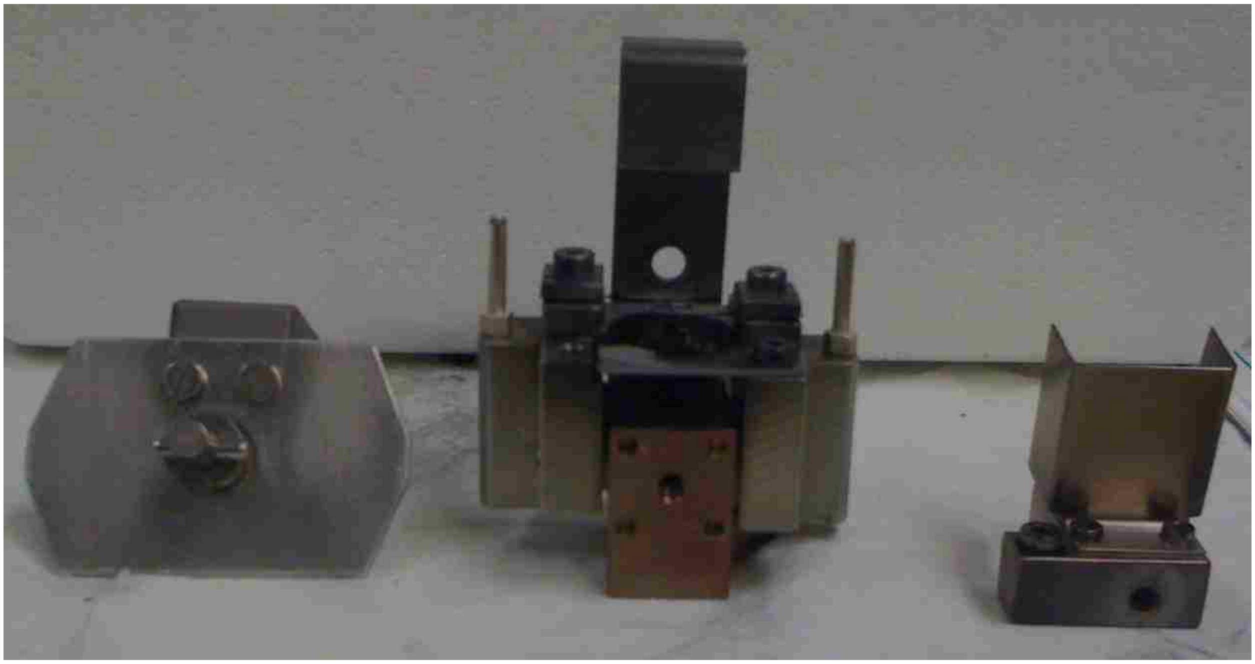

Appendix Figure G Carbon deposition gun (center) with Wehnelt shield with deflector plate (right) and the gun holder with safety shield (or extraction rod attachment) removed (left).

14) Remove the threaded insert that holds the carbon rod.

15) Remove the lower cathode cover or plate.

16) Clean all pieces of the electron gun of deposited carbon. Canned air, tape, applicator sticks, etc. can be used to remove as much deposited material as possible. Be careful when working around the filament if it is going to be reused. Once all the pieces have been cleaned, it can be put back together.

17) Replace the cathode cover or plate.

18) Replace the cathode or filament if needed. Remove the old filament (if it has not been done already). Use the setting gauge tool for centering the new cathode/filament and screw it into place under the pressure lamina.

19) Remove the carbon rod by loosening the screw on the bottom of the threaded insert to release the carbon rod from the collet chuck.

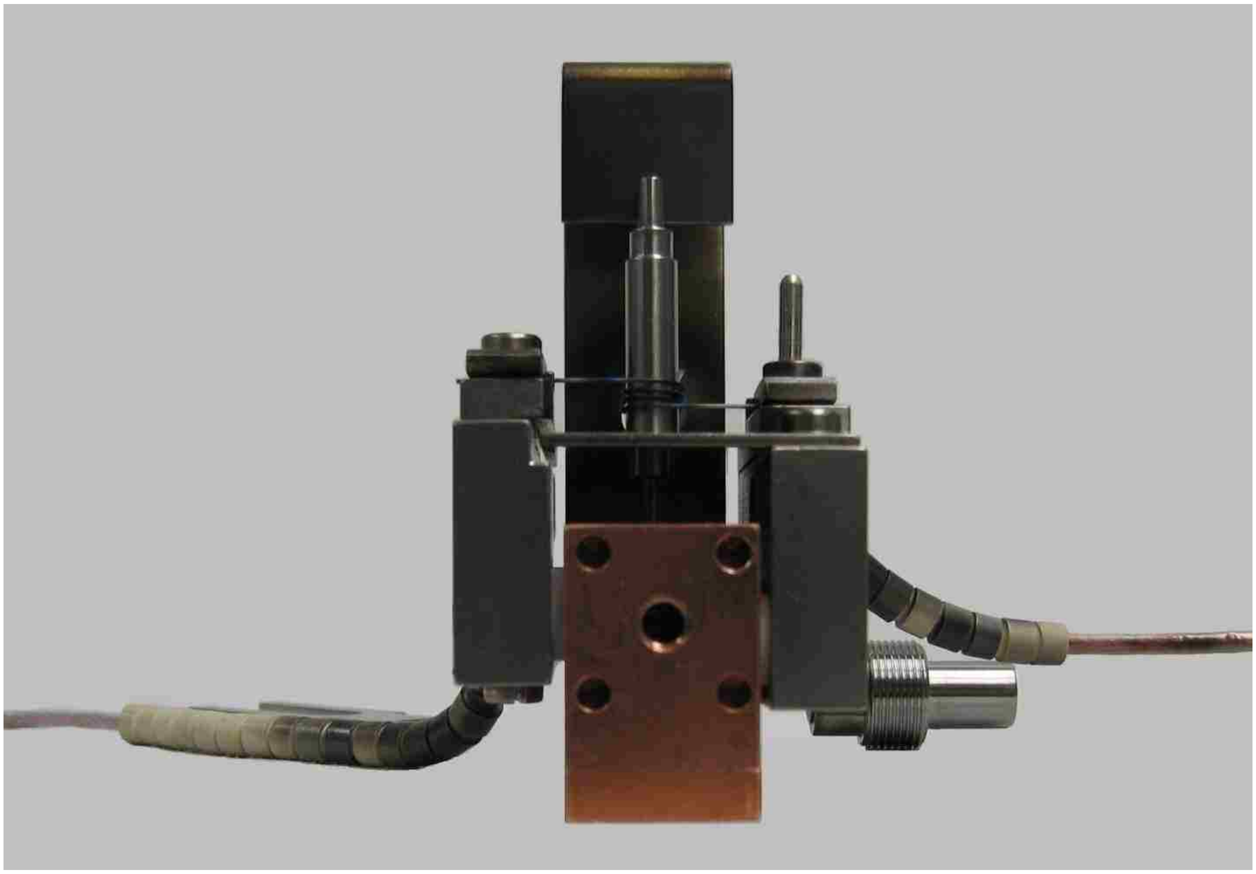

Appendix Figure H Gun with Wehnelt shield and deflector plate removed and the filament or cathode exposed. The setting gauge tool is in place; holding the filament so it can be tightened down. Notice the ceramic beads on the wires on either side of the gun. They must be free of material to prevent short circuits.

20) Insert the new carbon rod and leave the screw just loose enough to be able to move the carbon rod up and down in the collet chuck. Use the assembly tool to set the correct height of the carbon rod. The side of the tool with a “C” embossed on it must be used to set the height that the carbon rod should protrude from the chuck. Tighten the screw on the bottom of the rod holder once the carbon rod is at the correct height. Carbon rods that have been used once can be turned around and repositioned if they are long enough to meet the height requirement. New carbon should be cut in half to fit.

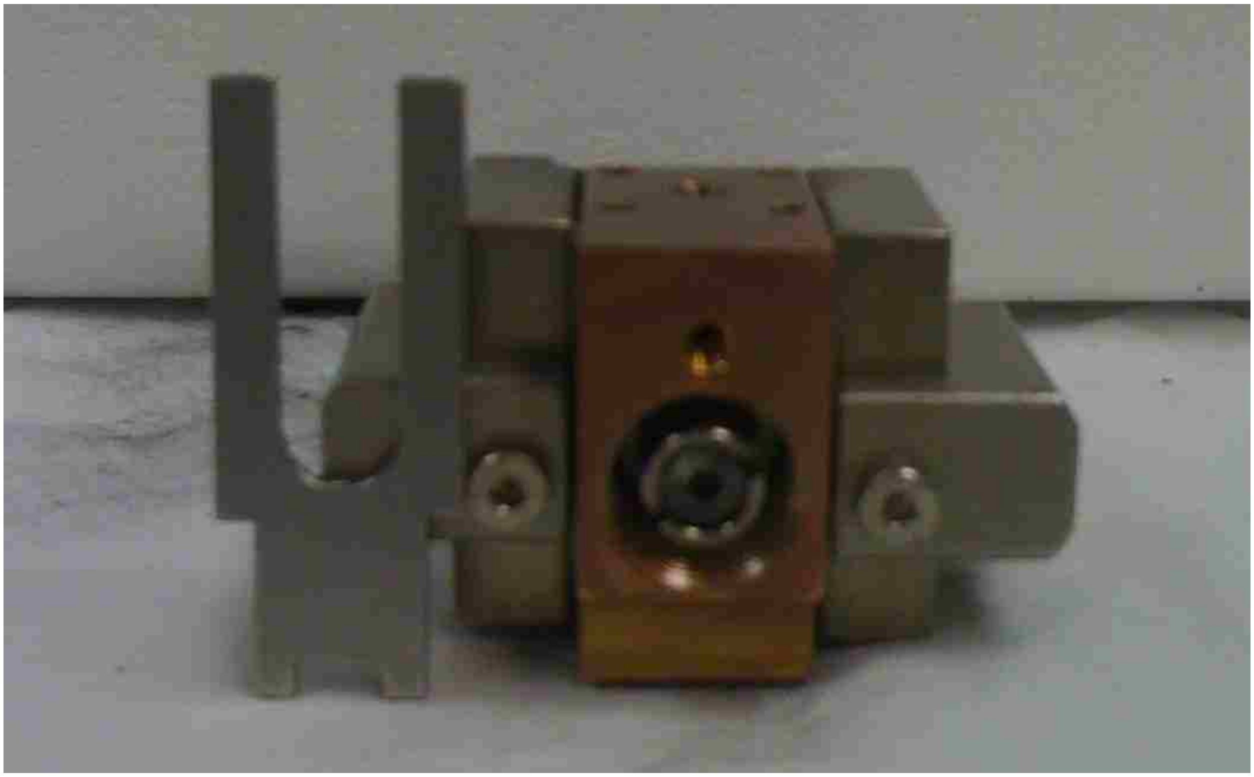

Appendix Figure I The assembly tool is used to remove the rod holder from the gun.

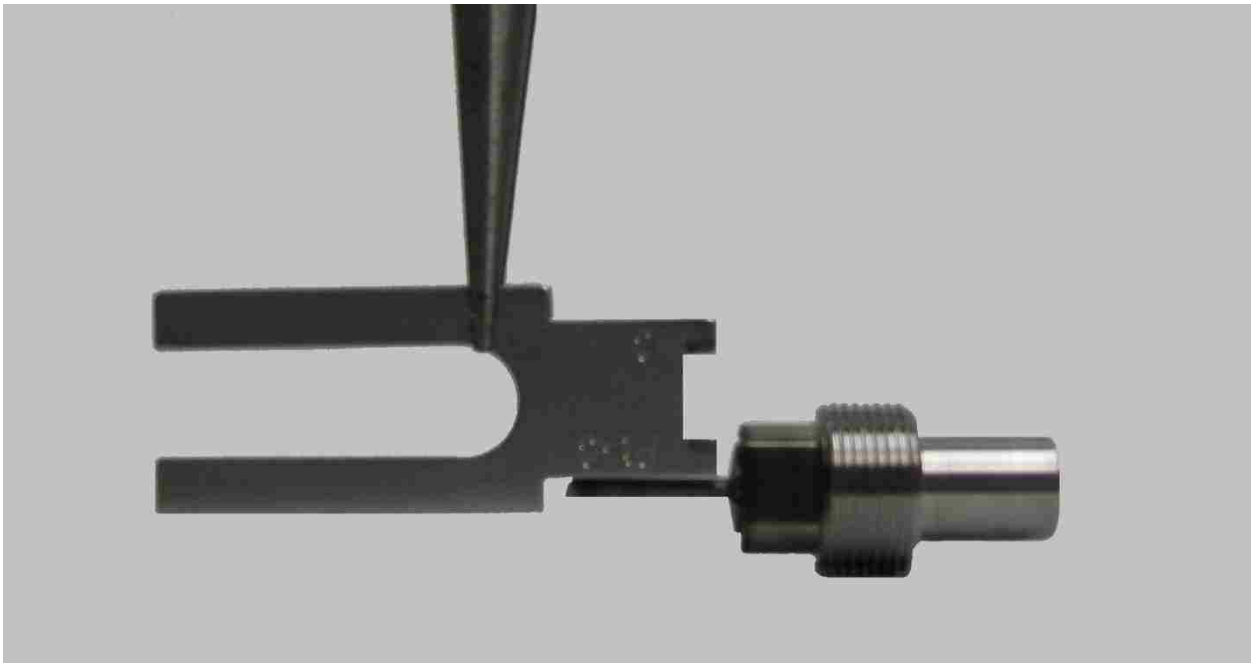

Appendix Figure J The assembly tool is also used to set the height of the rod in the collet and rod holder.

21) Screw the threaded insert for holding the evaporation rod back into the gun head. With the assembly tool, set the top of the carbon rod to be between the second and third wrung of the filament. Hold the evaporation gun up to the light and look through the hole in the collector plate or back piece of metal to set the height appropriately.

22) Replace the Wehnelt shield and deflector plate.

23) Replace the gun holder.

24) Vent the interlock chamber.

25) Connect the gun to the insertion rod.

26) Insert into the interlock chamber. The back of the collector plate or back of the gun goes to the right against a piece of metal inside the interlock chamber that acts as a guide for the electron gun.

27) Pump down the interlock chamber then close the pump valve.

28) Open SV2.

29) Insert electron gun straight into the vacuum chamber to line up the pegs with the plugs inside the chamber. The light to illuminate the sample chamber may need to be turned on to help guide the gun into place. To do this, press the “Mains” button on the Freeze Etching Unit Control BMS 101and press “Lamp.”

30) Turn the rod handle ¼ turn counterclockwise to release the rod from the gun holder.

31) Make sure the collar on the interlock chamber is in place and pull the rod straight out. Make sure it is clear of the SV2 valve.

32) Close SV2.

33) The carbon gun should be degassed before continuing. Refer to Appendix D on how to degas the evaporation sources.

34) If not using the BAF 400 immediately, turn off the EVM 030 and the BMS 101.

APPENDIX D SERVICING THE PLATINUM-CARBON ELECTRON GUN SOP

1) Check that the nitrogen cylinder is turned on and regulated at 80 psi. The ALC 101 valve controller should be turned on if it is off and all of the switches to the valves in the "off" or down position. If the liquid nitrogen tank is attached, open the tank slightly or disconnect it completely. Make sure the EVM 030 evaporation control unit is turned off.
2) The Key ACP-3000 cryo pump system controller should be on and running in "AUTOMATIC MODE." There is a button just below the display screen labeled "VENT MODE." Press this button and wait for the sample chamber to reach atmospheric pressure. The cryo pump system controller will automatically close and open the appropriate valves for venting the sample chamber.
3) Open the sample chamber once it has reached 1 atm by unscrewing the knob that holds the door closed. (Is the EVM 030 evaporation control unit turned off?)
4) The Pt-C gun is located on the right side of the sample chamber. Rotate the arm holding the Pt-C gun and unplug the cables that connect the evaporation control unit. It is wise to ensure there is no residual electric charge present by using the grounding probe next to the vacuum chamber, touching it to the metal parts of the gun and cold shroud.
5) Unscrew the thumb screw that holds the Pt-C gun to the arm. Remember to wear gloves when handling the gun and touching the inside of the chamber.
6) Remove the Wehnelt shield with the deflector plate.
7) Remove the threaded insert that holds the Pt-C rod.
8) Remove the lower cathode cover or plate.

9) Clean all pieces of the electron gun of deposited platinum. Canned air, tape, applicator sticks, etc. can be used to remove as much deposited material as possible. Be careful when working around the filament if it is going to be reused. Once all the pieces have been cleaned, it can be put back together.

10) Replace the cathode cover or plate.

11) Replace the cathode or filament if needed. Remove the old filament if it has not been done already. Use the setting gauge tool for setting the new filament and screw it into place under the pressure lamina.

12) Remove the old platinum-carbon rod by loosening the screw on the bottom of the threaded insert to release the Pt-C rod from the collet chuck.

13) Insert the new predrilled carbon rod and leave the screw just loose enough to be able to move the rod up and down in the collet chuck. There is an assembly tool that is used to set the correct height of the rod. One side of the tool has a Pt-C embossed on it. This is how high the Pt-C rod should protrude from the chuck. Tighten the screw once the carbon rod is at the correct height.

14) Add the Pt insert into the hole of the carbon rod.

15) Replace the Wehnelt shield and deflector plate.

16) Replace the Pt-C gun on the arm in the sample chamber, but attach it upside down so that the Pt-C rod points up preventing the Pt insert from dropping out.

17) Connect all the wires making sure you attach them to the same place they were before.

18) Close the sample chamber door and tighten the knob that holds the door closed.

19) Vacuum down the sample chamber. This can be accomplished by pressing the "Automatic Mode" button on the cryo pump system controller or can be done manually by opening the appropriate valves while the cryo pump controller is in manual mode.

20) Once the chamber is under vacuum, turn on the EVM 030 evaporation control unit.

21) Select the Pt-C gun by pressing "Gun 1" button above evaporation. Then degas for 4 seconds to fuse the Pt insert to the carbon rod by pressing "Gun 1" button above degas.

22) Press the off button and turn off the EVM 030 evaporation control unit.

23) Vent the vacuum chamber as before and open the door.

24) Remove any remaining electrical charge by touching the Pt-C gun with the grounding probe.

25) Disconnect the Pt-C gun and reposition so the gun is correctly aligned for deposition. Make sure the arm that the Pt-C gun attaches to is push back to the proper position.

26) Connect the wires and make sure the gun is in the right position. The gun attaches to an arm that must be pushed back in place to deposit Pt on the samples.

27) Close the vacuum chamber and press the "Automatic Mode" button on the cryo pump system controller.

28) Once the system has reached the appropriate vacuum, replicas can be made after degassing and testing both guns.

APPENDIX E DEGASSING SOP

If both guns need to be degassed, start with step 1 below; otherwise, start with step 5 to degas the carbon gun only. Remember: gun 1 is the Pt-C gun and gun 2 is the carbon deposition gun.

1) To degas the guns, turn on the EVM 030 Evaporation Control Unit by flipping the knob/switch on the left of the EVM 030 to "ON" position. Make sure the cryo pump controller is in automatic mode and operating within normal parameters.
2) Start by selecting gun 1 by pressing the button labeled "Gun 1" above the word "Evaporation" written on the EVM 030. A blinking green light on the button will indicate the active gun.
3) Degas gun 1 by the button labeled "Gun 1" above the word "Degas."
4) Press "OFF" after 2 min. have passed and continue to gun 2.
5) To degas gun 2, press "Gun 2" button above evaporation to activate gun 2.
6) Press "Gun 2" button above degas to begin degassing.
7) Press "OFF" after 5 minutes are up. It may automatically stop and the red light on the off button will light up.
8) If not using the BAF 400 immediately, turn off the EVM 030 and the BMS 101.

APPENDIX F SEMI-DILUTE SOLUTIONS OF HYDROXYPROPYL CELLULOSE

F.1 Introduction

Less is understood of semidilute than dilute solutions of macromolecules. As concentration increases, multiple decay rates are observed in dynamic light scattering (DLS). This multimodal phenomenon of 1 MDa hydroxypropyl cellulose (HPC) was investigated using DLS. The resulting decays were fitted using two-exponential fits and CONTIN. Several decay rates and amplitudes were obtained with each CONTIN fit but the two with the highest amplitude were determined to be the decay rates of interest—a fast and slow mode.

F.2 Results and Discussion

Solutions of 1 MDa HPC prepared using Barnstead Nanopure™ water were forced through a Millipore Durapore™ 0.45 micron filter to remove dust. Two different concentrations were used in the DLS experiments: 0.1 (dilute) and 0.89 wt% (semidilute) solution. All experiments were run at 25°C.

The decays of dilute HPC and concentrated HPC yield different curves as shown in Appendix Figure K. The concentrated HPC solution shows a multiexponential decay. This represents a fast and a slow mode. The CONTIN analysis of concentrated HPC gave decay rates and amplitudes that correlate with the fast and slow modes observed. Appendix Figure L shows the CONTIN plot with the decay rate of concentrated HPC at angle 25°.

Laplace inversion was performed on the correlograms obtained at each angle (20°-120°) and plotted in Appendix Figure M. The points that were considered to not contribute to the appropriate mode were omitted. Taking the data from CONTIN and using the

Einstein-Stokes equation, a hydrodynamic radius vs. q^2 plot was generated. It shows that the concentrated HPC has two modes corresponding to two different radii.

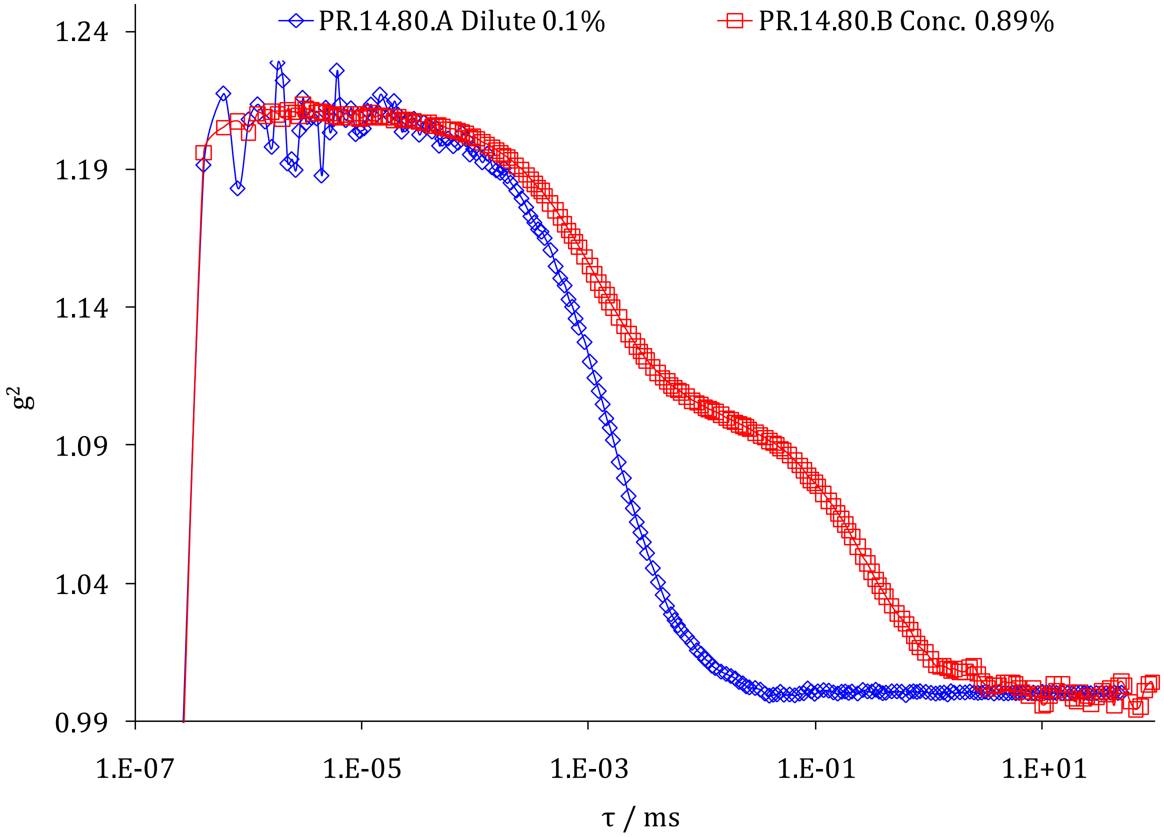

Appendix Figure K 1M Mw hydroxypropyl cellulose at 0.1 (—□—) and 0.89 (—○—) wt% solutions in Nanopure™ H2O. DLS sample holder maintained at 25°C at θ = 35° (q = 79421 cm^{-1}).

We can further convert the intensities to *Rayleigh* factors using the equation:

$$Rayleigh(\theta) = \left[I_{\text{sample}}\ (\theta) - I_{\text{sample}}\ (\theta)\right] \sin\theta \left[\frac{Rayleigh_{\text{toluene}}\ (90)}{I_{\text{toluene}}\ (90)}\right]\left[\frac{n_{\text{toluene}}}{n_{\text{sample}}}\right]$$

Equation 22

For each concentration, the angular dependence of the *Rayleigh* factor is fit to the function derived by Guinier (Equation 17). These results of the Guinier plot of the *Rayleigh* factor vs. q^2 is the apparent R_g.

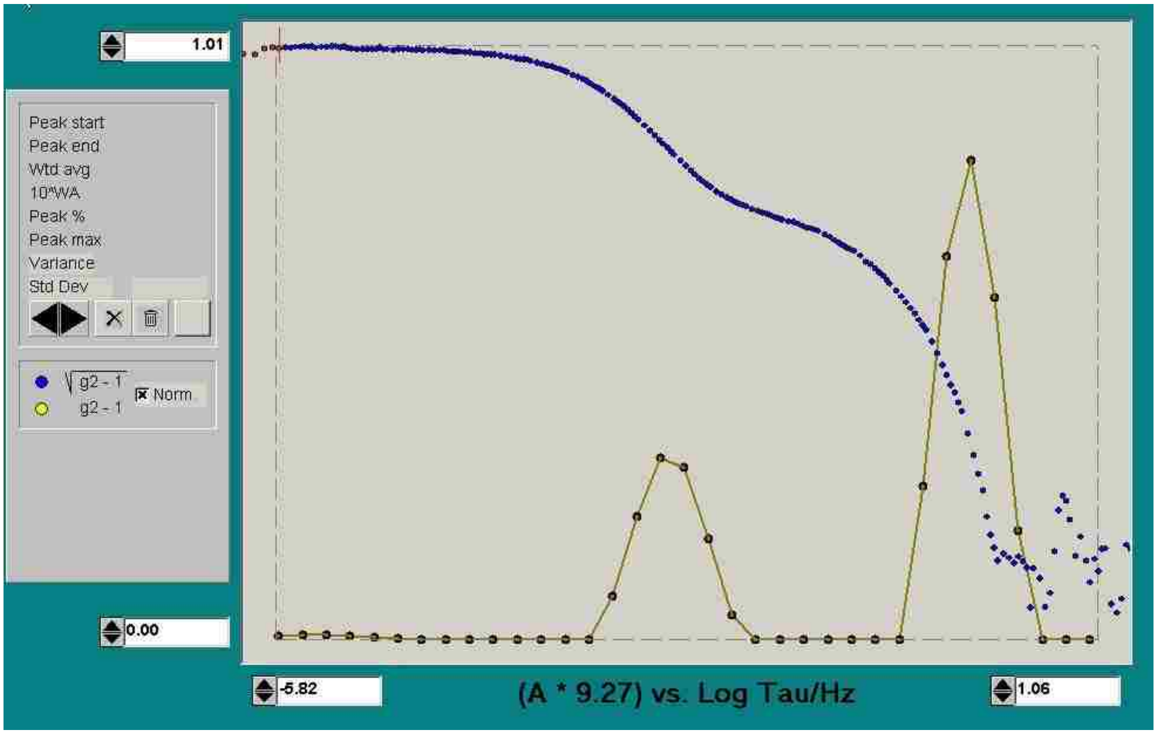

Appendix Figure L Overlay of decay time spectrum from CONTIN with $g^{(1)}(\tau)$ for 0.89 wt% HPC 1M g/mol at wavelength of 6.328×10^{-5} cm and 25° scattering angle ($q = 5.716 \times 10^4$ cm^{-1}). The inflection points of $g^{(1)}(\tau)$ correspond with the peaks from CONTIN.

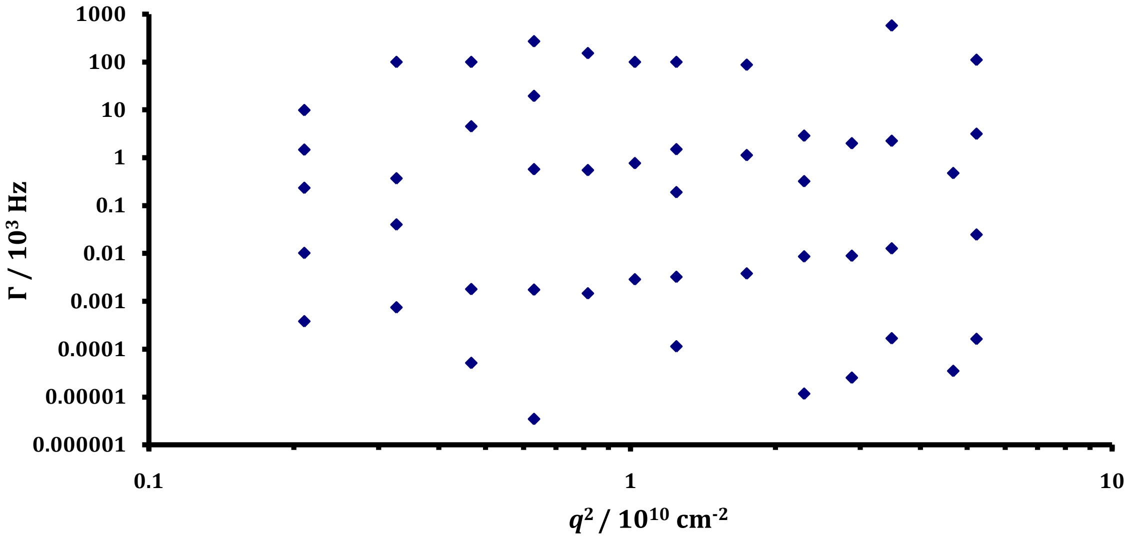

Appendix Figure M The Γ's given by CONTIN at each angle for 0.89 wt% 1M g/mol HPC. Even though multiple decay rates are obtained, most of them correspond to extremely small amplitudes. In the rest of the plots, the Γ's and amplitudes that account for a minuscule percentage of the total area under the CONTIN plot are eliminated in favor for the two that represent the fast and slow modes.

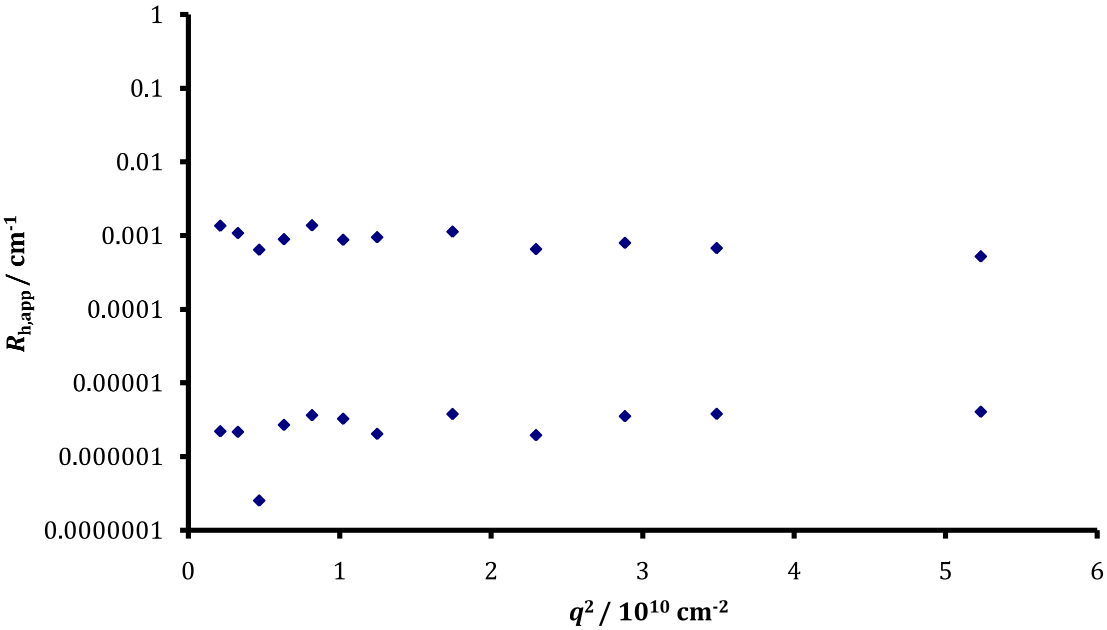

Appendix Figure N The apparent radii at each angle of the 0.89 wt% 1M g/mol HPC calculated by the Einstein-Stokes equation shows the size of the fast (bottom set of data points) and slow (upper set) modes to be several orders of magnitude apart.

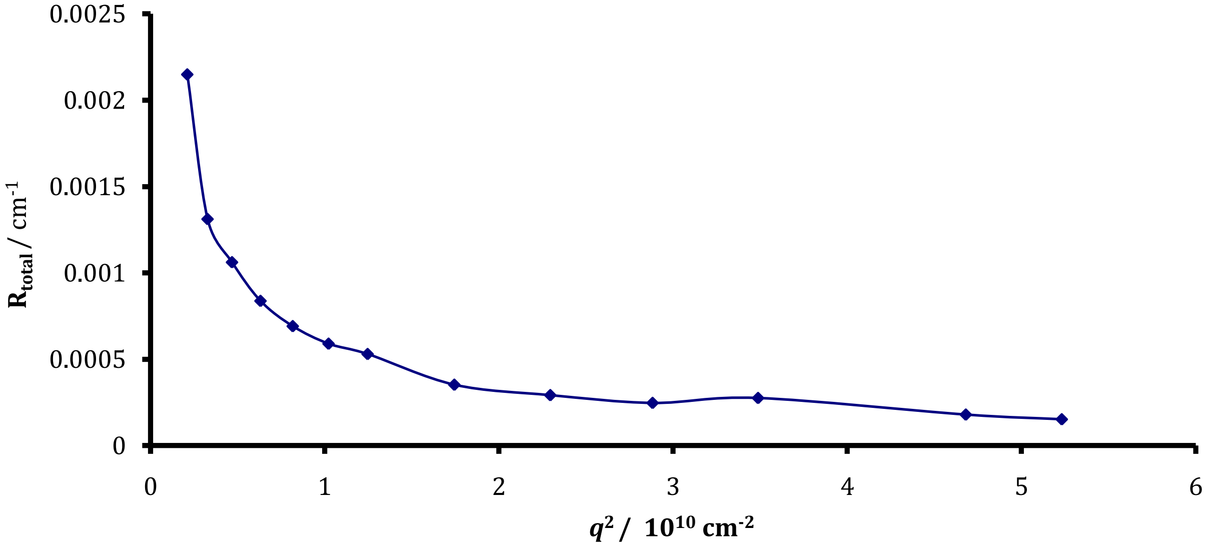

Appendix Figure O The total scattering envelope of 0.89 wt% 1M g/mol HPC.

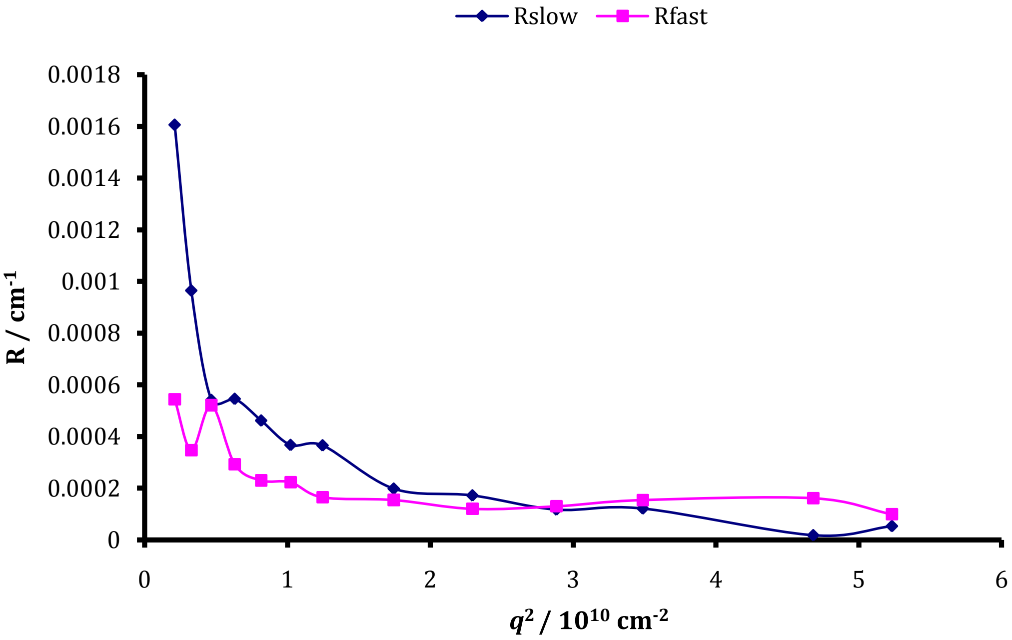

Appendix Figure P Same conditions as Appendix Figure O with slow and fast modes separated.

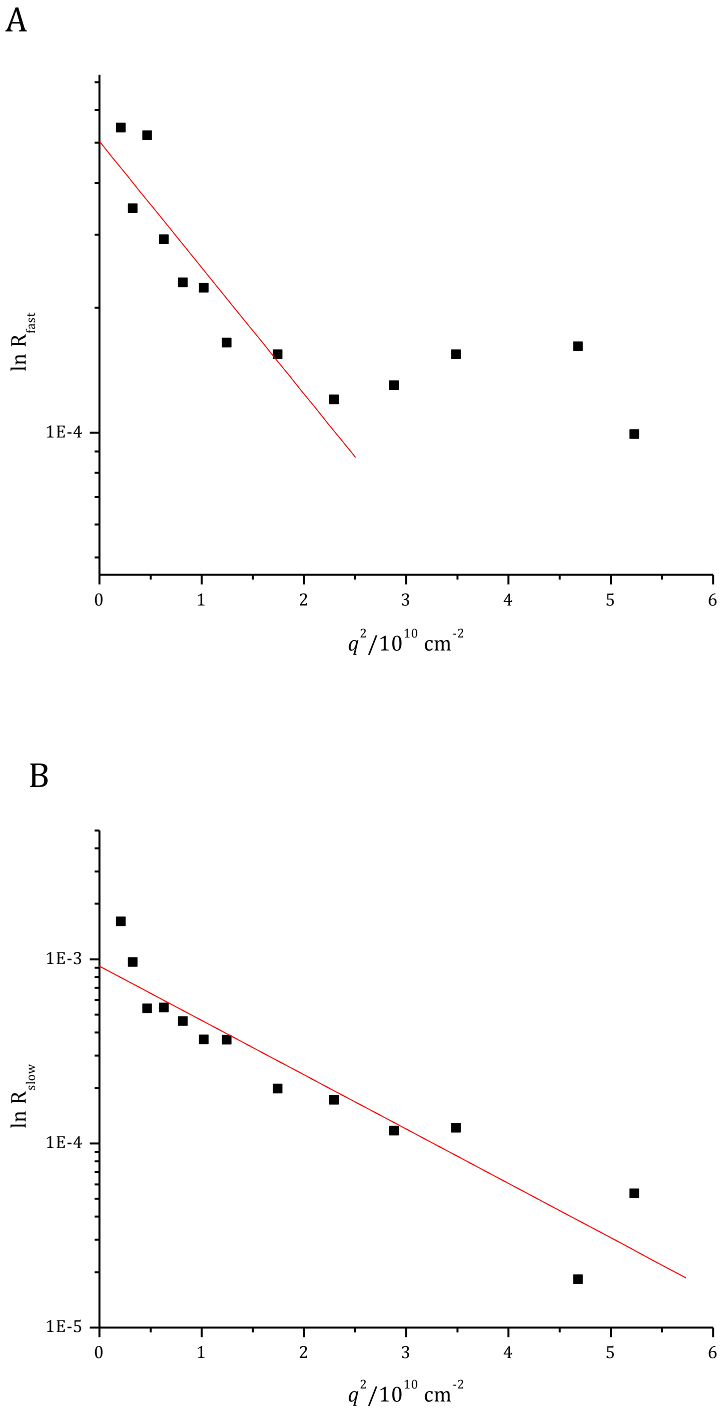

Appendix Figure Q A) A Guinier plot of the natural logarithm of Rayleigh scattering associated with the fast mode vs. q^2. The R_g obtained is 145 nm. B) A Guinier plot of the natural logarithm of Rayleigh scattering associated with the slow mode vs. q^2. The R_g obtained is 142 nm.

APPENDIX G DEXTRAN: GEL PERMEATION CHROMATOGRAPHY—MULTI-ANGLE LIGHT SCATTERING AND RHEOLOGY STUDY

Gel Permeation Chromatography (GPC) is a staple of macromolecular characterization. When carefully performed, it can yield accurate molecular weights and coupled with a Wyatt multi-angle light scattering (MALS), it is an absolute method not requiring a calibration curve. The preceding table contains data compiled from GPC-MALS work. Samples consisted of 3 mg/ml solutions of dextran standards from Polysciences, Inc.

Appendix Table A Weight average molecular weight, polydispersity, and root of the weight average and *z*-average of the squared radius of gyration of dextrans by GPC-MALS.

	Advertised			Measured			
Catalog#	Lot#	$M_w/10^3$	M_w/M_n	$M_w/10^3$	M_w/M_n	R_g (R_w)/nm	R_g (R_z)/nm
PSS-dxtkit[c§]	Dxtp1	0.180	1.0	N/A			
PSS-dxtkit[c§]	Dxtp2	0.342	1.0	N/A			
PSS-dxtkit[c§]	Dxt1n1	1.2	1.18	N/A			
PSS-dxtkit[c§]	Dxt5	5.2	1.6	N/A			
PSS-dxtkit[c§]	Dxt12	12.0	1.56	12.0 ± 0.6	1.12	-	-
PSS-dxtkit[c§]	Dxt25	23.8	1.30	23.8 ± 0.3	1.05	-	-
19412[a]	497100	40.0	1.5	41.6 ± 1.5	1.1	-	-
PSS-dxtkit[c§]	Dxt50	48.6	1.36	48.4 ± 2	1.07	-	-
19413[a]	503606	75.0	1.5	77.0 ± 3.6	1.3	-	-
PSS-dxtkit[c§]	Dxt150	148	1.47	143 ± 6.8	1.22	10.3 ± 2	10.7 ± 1
19414[a]	410586	170	2.0	161 ± 6.4	1.7	17 ± 4	17 ± 3
PSS-dxtkit[c§]	Dxt270	273	1.66	259 ± 7.4	1.16	14.2 ± 2	16 ± 2
PSS-dxtkit[c§]	Dxt410	410	1.73	389 ± 24	1.28	18.2 ± 1	19.1 ± 1
D-1037[b]	90K-1897	413	-	370 ± 17	3.8	20 ± 3	21 ± 2
19415[a]	451049	600	1.7	536 ± 21	1.7	21 ± 2	24 ± 1
dxt670k[c]	- [d]	676	1.94	647 ± 30	1.7	19 ± 4	22 ± 2
dxt2370k[c]	- [d]	2370	1.61	1770 ± 34	1.3	24 ± 2	26 ± 2
dxt2750k[c]	- [d]	2750	1.67	1550 ± 30	1.4	28 ± 2	30 ± 2

[a] Polysciences. [b] Sigma. [c] Polymer Standards Services. [d] Same as Catalog #

§ Measurement made by Derek Dorman

An AR 2000 Advanced Rheometer by TA Instruments in Dr. DeKee's laboratory at Tulane University was used to obtain viscosity vs. shear rate information (Appendix Figure R).

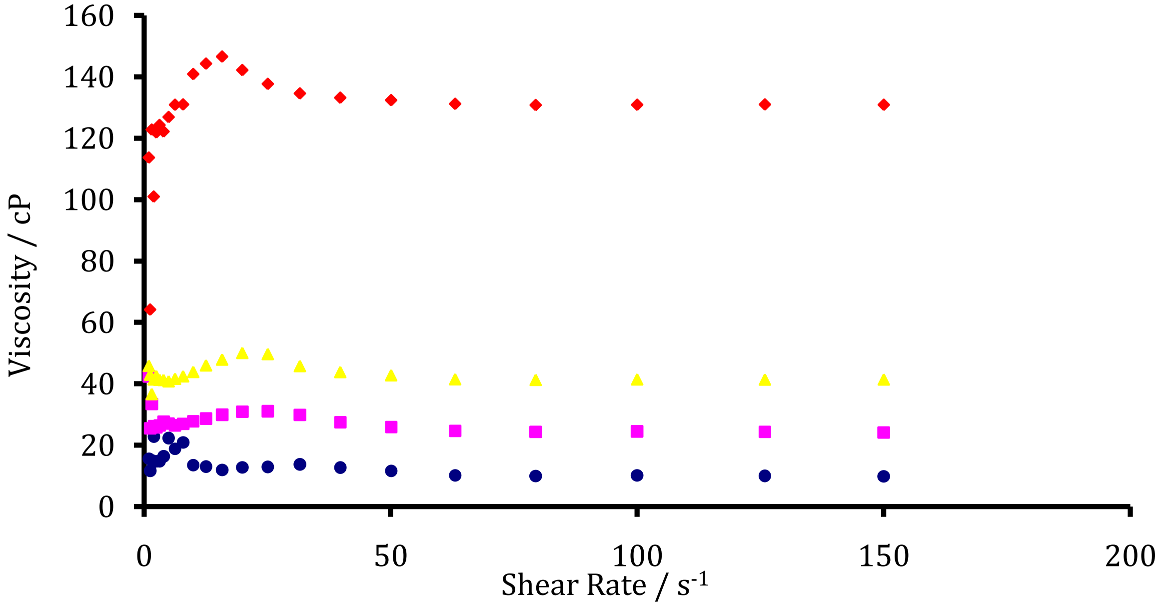

Appendix Figure R Data recorded from the AR 2000 of the viscosity of 15 wt% dextran solutions for M_w 43,000 (●), 188,000 (■), 413,000 (▲), and 2,000,000 (◆).

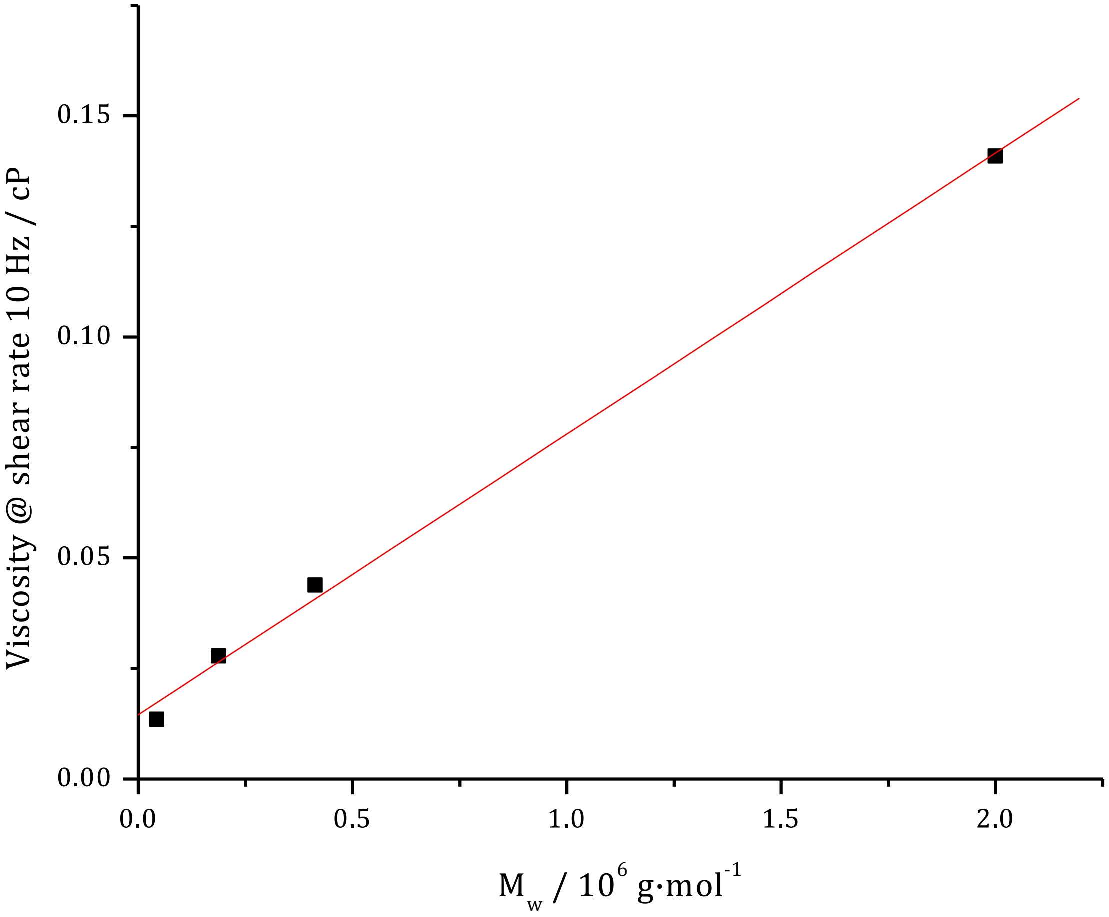

Appendix Figure S Viscosity vs. M_w of 15 wt% solutions of dextran. The viscosity increases linearly as the M_w increases.

APPENDIX H HEXAGONAL TERPYRIDINE-RUTHENIUM MACROCYCLIC COMPLEX STUDIES

Atomic force microscopy (AFM) was used to image HexRu. Earlier work by Newkome et al showed AFM images of HexRu forming rings consisting of 6 ruthenium atoms with terpyridine molecules between them.[71] The AFMs images did not show the same arrangement, which supports the deviation of experimental SAXS and WAXS data from the theoretical P(q). A 2 mg of HexRu was dissolved in 1 ml of acetonitrile 6 days before AFM could be performed. The AFM sample was prepared by adding 2 drops of the solution to a clean glass microscope slide, drying between each. The images showed large aggregates 10-20 mm across, Appendix Figure T and Appendix Figure U. To verify that the large particles observed were due to aggregation over time as DLS suggested, a fresh sample was made with a concentration of 1.8 mg/ml and imaged immediately. The resulting images, Appendix Figure V and Appendix Figure W, contained fewer and smaller aggregates than Appendix Figure T and Appendix Figure U.

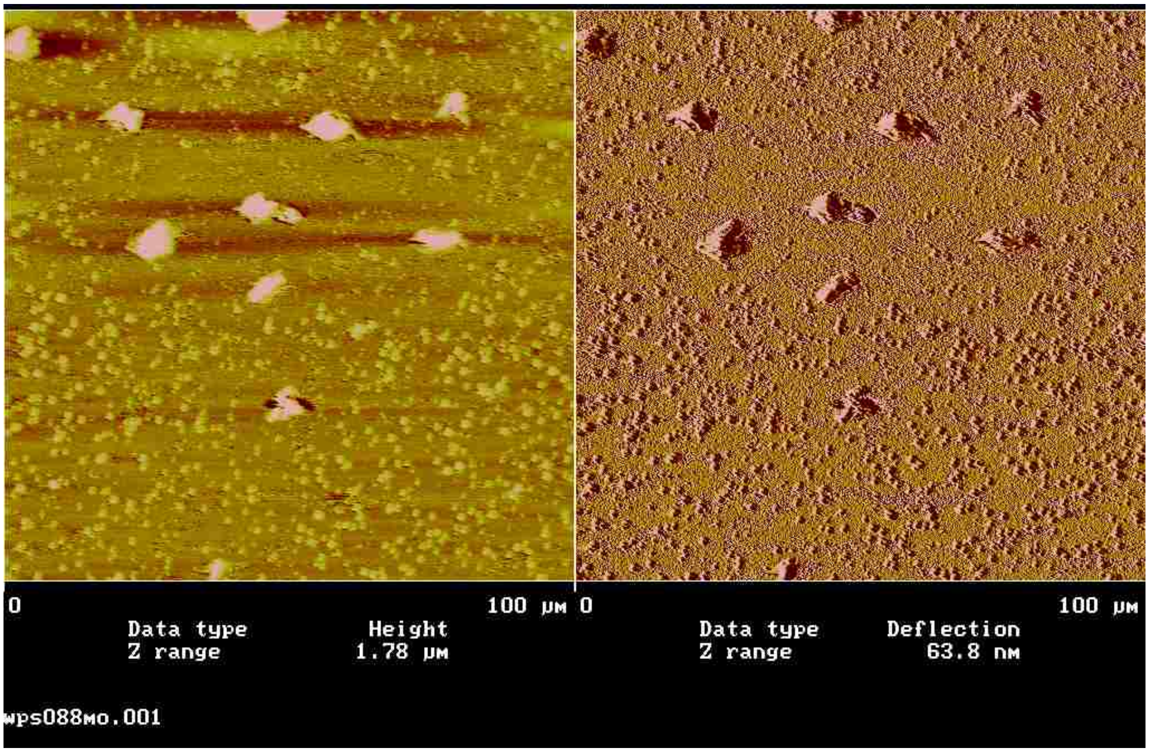

Appendix Figure T HexRu dissolved in acetonitrile 6 days before imaging. Two drops were allowed to dry on a glass slide to image. The large particles are between 10 and 20 μm across.

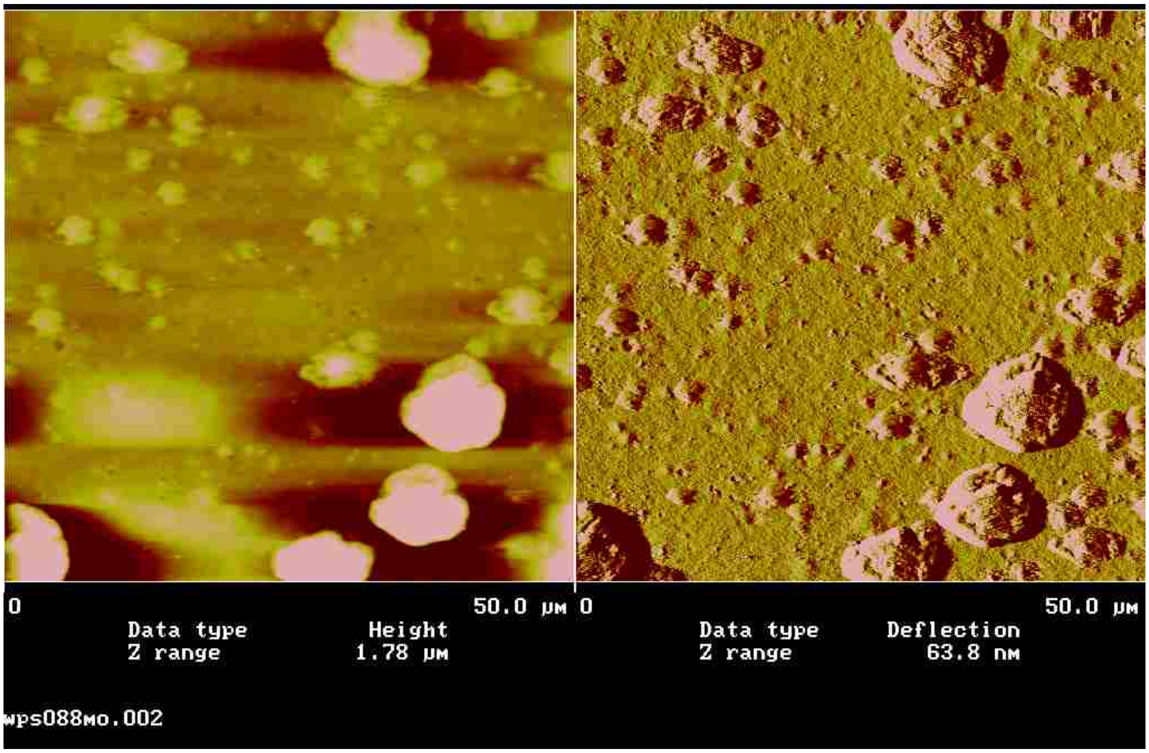

Appendix Figure U A magnified view of the large aggregates in the dried HexRu sample.

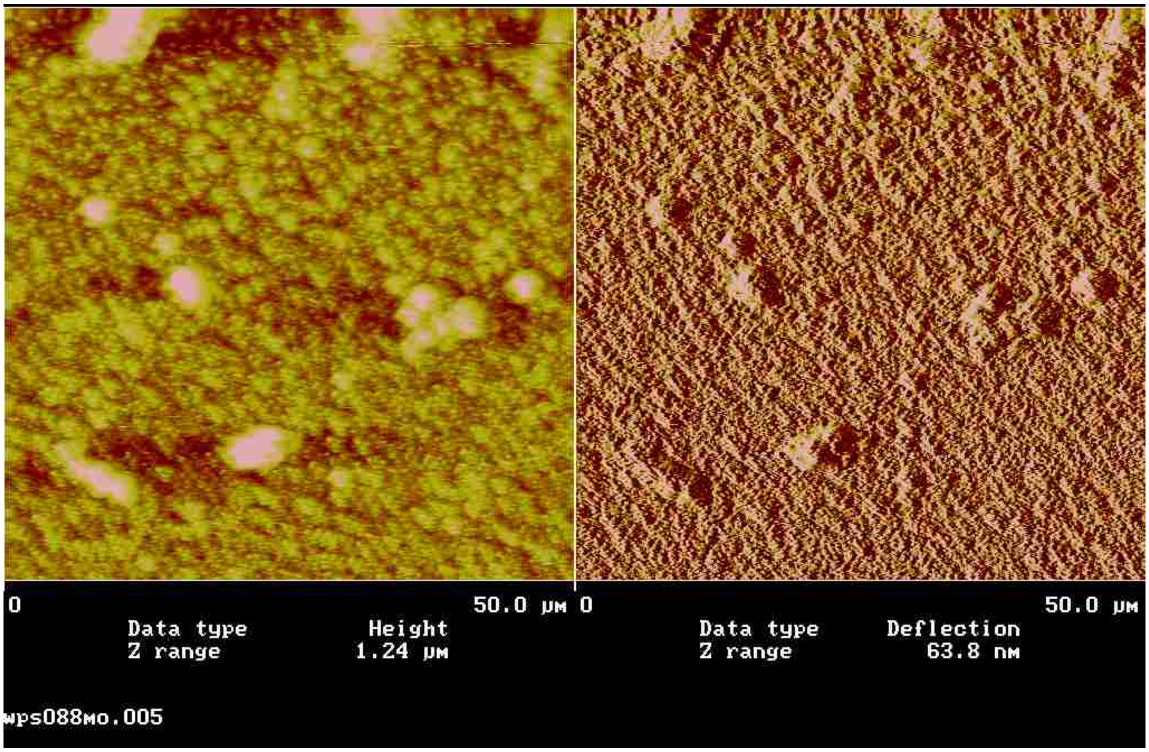

Appendix Figure V Newly prepared 1.8 mg/ml HexRu drop dried on a glass slide and imaged with AFM. Large aggregates are still visible.

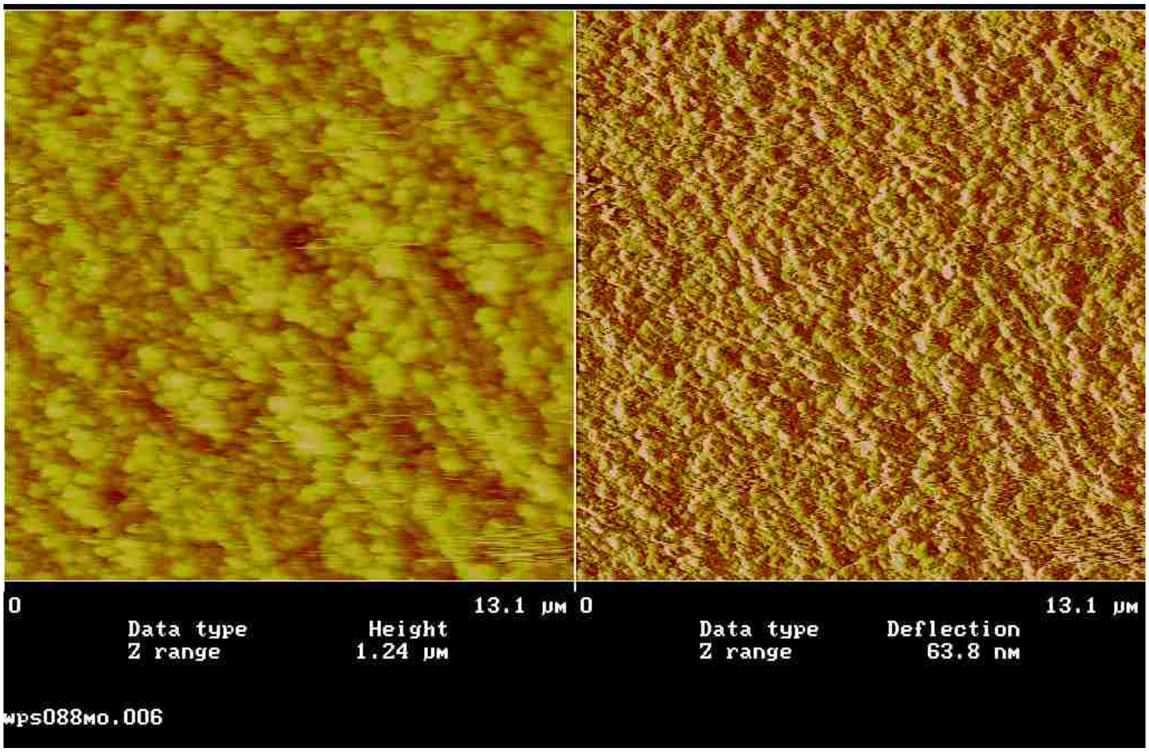

Appendix Figure W Area of newly prepared 1.8 mg/ml HexRu drop dried on a glass slide where no large aggregates exist.

REFERENCES

1. Kim, S.; Martin, G. M. Preparation of Cell-size Unilamellar Liposomes with High Captured Volume and Defined Size Distribution. *Biochimica et Biophysica Acta* **1981,** *646*, 1-9.

2. Tomalia, D. A.; Naylor, A. M.; Goddard, W. A. Starburst Dendrimers - Molecular-Level Control of Size, Shape, Surface-Chemistry, Topology, and Flexibility from Atoms to Macroscopic Matter. *Angewandte Chemie-International Edition in English* **1990,** *29* (2), 138-175.

3. *Advances in Dendritic Macromolecules;* Jai Press: Greenwich, CT, 1994.

4. Tomalia, D. A. Dendrimer Molecules. *Scientific American* **1995,** *272* (5), 62-66.

5. Mohwald, H. Phosphilipid and Phospholipid-Protein Monolayers at the Air/Water Interface. *Ann. Rev. Phys. Chem.* **1990,** *41*, 441-476.

6. Fendler, J. H.; Wiley Interscience *Membrane Mimetic Chemistry;* Wiley Interscience: New York, 1982.

7. Ludtke, S.; He, K.; Huang, H. Membrane Thinning Caused by Magainin 2. *Biochemistry* **1995,** *34*, 16764-16769.

8. Arnold, K.; Ohki, S.; Krumbiegel, M. Interaction of Dextran Sulfate with Phospholipid Surfaces and Liposome Aggregation and Fusion. *Chemistry and Physics of Lipids* **1990,** *55*, 301-307.

9. Haas, H.; Mohwald, H. Ordered Protein Arrays as Mesophases. *Langmuir* **1994,** *10*, 363-366.

10. Smith, L. J.; Clark, D. C. Measurement of the Secondary Structure of Adsorbed Protein by Circular Dichroism. 1. Measurements of the Helix Content of Adsorbed Melittin. *Biochimica et Biophysica Acta* **1992,** *1121*, 111-118.

11. Harvey, L. J.; Bloomberg, G.; Clark, D. C. The Influence of Surface Hydrophobicity on the Adsorbed Confonnation of a beta-Sheet-Forming Synthetic Peptide. *J. Coll. Int. Sci.* **1995,** *170*, 161-168.

12. Beschiaschvili, G.; Seelig, J. Peptide Binding to Lipid Bilayers. Nonclassical Hydrophobic Effect and Membrane-Induced pK Shifts. *Biochemistry* **1992,** *31*, 10044-10053.

13. Dufourcq, J.; Faucon, J. F.; Fourche, G.; Dasseux, J. L.; Lemaire, M.; Gulikkrzywicki, T. Morphological-Changes of Phosphatidylcholine Bilayers Induced by Melittin -

Vesicularization, Fusion, Discoidal Particles. *Biochimica et Biophysica Acta* **1986,** *859* (1), 33-48.

14. Saville, P. M.; White, J. W.; Hawker, C. J.; Wooley, K. L.; Frechet, J. M. J. Dendrimer and Polystyrene Surfactant Structure at the Air-Water Interface. *J. Phys. Chem.* **1993,** *97*, 293-294.

15. Slany, M.; Bardaji, M.; Casanove, M. J.; Caminade, A. M.; Majoral, J. P.; Chaudret, B. Dendrimer Surface Chemistry. Facile Route to Polyphosphines and Their Gold Complexes. *J. Am. Chem. Soc.* **1995,** *117*, 9764-9765.

16. Wells, M.; Crooks, R. M. Interactions Between Organized, Surface-Confined Monolayers and Vapor-Phase Probe Molecules. 10. Preparation and Properties of Chemically Sensitive Dendrimer Surfaces. *J. Am. Chem. Soc.* **1996,** *118*, 3988-3989.

17. Caminati, G.; Turro, N. J.; Tomalia, D. A. Photophysical Investigation of Starburst Dendrimers and Their Interactions with Anionic and Cationic Surfactants. *J. Am. Chem. Soc.* **1990,** *112*, 8515-8522.

18. Li, Y.; Dubin, P. L.; Spindler, R.; Tomalia, R. S. Complex Formation Between Poly(dimethyldiallylammonium chloride) and Carboxylated Dendrimers. *Macromolecules* **1995,** *28*, 8426-8428.

19. Jockusch, S.; Turro, N. J.; Tomalia, D. A. Aggregation of Methylene Blue Adsorbed on Starburst Dendrimers. *Macromolecules* **1995,** *28*, 7416-7418.

20. Zhang, H.; Dubin, P. L.; Spindler, R. Binding of Carboxylated Starburst Dendrimers to Poly(diallyldimethylammonium chloride). *Phys. Chem.* **1996,** *100*, 923-928.

21. Evers, O. A.; Fleer, G. J.; Scheutjens, J. M. H. M.; Lyklema, J. Adsorption of Weak Polyelectrolytes from Aqueous Solution. *J. Coll. Int. Sci.* **1986,** *111*, 446-454.

22. Muthukumar, M. Adsorption of a Polyelectrolyte Chain to a Charged Surface. *J. Chem. Phys.* **1987,** *86*, 7230-7235.

23. von Goeler; Muthukumar, M. Adsorption of Polyelectrolytes onto Curved Surfaces. *J. Chem. Phys.* **1994,** *100*, 7796-7803.

24. Liett, S. M.; Orrock, A.; Poon, W. C. K.; Pusey, P. N. Phase Behavior of a Model Colloid-Polymer Mixture. *Phys. Rev. E.* **1995,** *51*, 1344-1352.

25. Walz, J. Y. Effect of Polydispersity on the Depletion Interaction Between Colloidal Particles. *J. Coll. Int. Sci.* **1996,** *178*, 505-513.

26. Smith, N. J.; Williams, P. Depletion Flocculation of Polystyrene Latices by Water-Soluble Polymers. *A. J. Chem. Soc. Far. Trans.* **1995,** *91*, 1483-1489.

27. Mansfield, M. L. Surface Adsorption of Model Dendrimers. *Polymer* **1996,** *17*, 3835-3841.

28. Sunamoto, J.; Sato, T.; Taguchi, T.; Hamazaki, H. Naturally Occurring Polysaccharide Derivatives which Behave as an Artificial Cell Wall on an Artificial Cell Liposome. *Macromolecules* **1992,** *25*, 5665-5670.

29. Dagani, R. Lipids and Minerals Form Novel Composite Microstructures. *Chemical and Engineering News* **1993,** 19-20.

30. Ringsdorf, H.; Schlarb, B.; Tyminski, P. N.; O'brien, D. F. Permeability Characteristics of Liposomes in a Net--Membranes of Dihexadecyl Phosphate with Polymerizable Gegenions. *Macromolecules* **1988,** *21*, 671-677.

31. Oostwal, M. G.; Blees, M. H.; De, B.; Leyte, J. D. Chain Self-Diffusion in Aqueous salt-free Solutions of Sodium Poly(styrenesulfonate). *Macromolecules* **1993,** *26*, 7300-7308.

32. *Encyclopedia of Polymer Science;* John Wiley & Sons: New York, 1990.pp. 46-92.

33. Dubin, P. L.; Edwards, S. L.; Kaplan, J. I.; Mehta, M. S.; Tomalia, D. A.; Xia, J. Carboxylated Starbust Dendrimers as Calibration Standards for Aqueous Size Exclusion Chromatography. *Anal. Chem.* **1992,** *64*, 2344-2347.

34. Ottaviani, M. F.; Turro, N. J.; Jockusch, S.; Tomalia, D. A. Aggregational Process of the Positively Charged Surfactants CTAC and CAT16 in the Presence of Starburst Dendrimers: an Electron Paramagnetic Resonance Spectroscopic Study. *Colloids and Surfaces A: Physical and Engineering Aspects* **1997**.

35. Gopidas, K. R.; Leheny, A. R.; Caminati, G.; Turro, N. J.; Tomalia, D. A. Photophysical Investigation of Similarities Between Starburst Dendrimers and Anionic Micelles. *Journal of the American Chemical Society* **1991,** *113* (19), 7335-7342.

36. Ottaviani, M. F.; Daddi, R.; Brustolon, M.; Turro, N. J.; Tomalia, D. A. Interaction Between Starburst Dendrimers and SDS Micelles Studied by Continuous-wave and Pulsed Electron Spin Resonances. *Applied Magnetic Resonance* **1997,** *13* (3-4), 347-363.

37. Ottaviani, M. F.; Favuzza, P.; Sacchi, B.; Turro, N. J.; Jockusch, S.; Tomalia, D. A. Interactions Between Starburst Dendrimers and Mixed DMPC/DMPA-Na Vesicles Studied by the Spin Label and the Spin Probe Techniques, Supported by Transmission Electron Microscopy. *Langmuir* **2002,** *18* (6), 2347-2357.

38. Ottaviani, M. F.; Andechaga, P.; Turro, N. J.; Tomalia, D. A. Model for the Interactions Between Anionic Dendrimers and Cationic Surfactants by Means of the Spin Probe Method. *Journal of Physical Chemistry B* **1997,** *101* (31), 6057-6065.

39. Ottaviani, M. F.; Daddi, R.; Brustolon, M.; Turro, N. J.; Tomalia, D. A. Structural Modifications of DMPC Vesicles upon Interaction with Poly(amidoamine) Dendrimers Studied by CW-Electron Paramagnetic Resonance and Electron Spin-Echo Techniques. *Langmuir* **1999,** *15*, 1973-1980.

40. Zhang, Z.; Smith, B. D. High-Generation Polycationic Dendrimers Are Unusually Effective at Disrupting Anionic Vesicles: Membrane Bending Model. *Bioconjugate Chemistry* **2000,** *11*, 805-814.

41. Mecke, A.; Uppuluri, S.; Sassanella, T. M.; Lee, D. K.; Ramamoorthy, A.; Baker, J. R.; Orr, B. G.; Holl, M. M. B. Direct Observation of Lipid by Poly(amidoamine) Bilayer Disruption Dendrimers. *Chemistry and Physics of Lipids* **2004,** *132* (1), 3-14.

42. Polo, L.; Bianco, G.; Reddi, E.; Jori, G. The Effect of Different Liposomal Formulations on the Interaction of Zn(Ii)-Phthalocyanine with Isolated Low and High-Density-Lipoproteins. *International Journal of Biochemistry & Cell Biology* **1995,** *27* (12), 1249-1255.

43. Ruozi, B.; Tosi, G.; Leo, E.; Vandelli, M. A. Application of atomic force microscopy to characterize liposomes as drug and gene carriers. *Talanta* **2007,** *73* (1), 12-22.

44. Antonietti, M.; Forster, S. Vesicles and liposomes: A self-assembly principle beyond lipids. *Advanced Materials* **2003,** *15* (16), 1323-1333.

45. Yatvin, M. B.; Lelkes, P. I. Clinical Prospects for Liposomes. *Medical Physics* **1982,** *9* (2), 149-175.

46. Woodle, M. C.; Storm, G.; Newman, M. S.; Jekot, J. J.; Collins, L. R.; Martin, F. J.; Szoka, F. C. Prolonged Systemic Delivery of Peptide Drugs by Long-Circulating Liposomes - Illustration with Vasopressin in the Brattleboro Rat. *Pharmaceutical Research* **1992,** *9* (2), 260-265.

47. Sun, J.; Ramanathan, M.; Dorman, D.; Newkome, G. R.; Moorefield, C. N.; Russo, P. S. Surface properties of a series of amphiphilic dendrimers with short hydrophobic chains. *Langmuir* **2008,** *24* (5), 1858-1862.

48. Rontgen, W. C. On a New Kind of Rays. *Nature* **1896,** *53* (1369), 274-276.

49. News, information, and educational materials about the world's synchrotron and free electron laser light source facilities. *lightsources. org* http://www.lightsources.org/cms/ [Accessed 2010 June 3] **2010**.

50. Rigaku SAXS products. *Rigaku Website* http://www.rigaku.com/ [Accessed 2010 June 3] **2010**.

51. Barbosa, A. F.; Gabriel, A.; Craievich, A. An X-Ray Gas Position-Sensitive Detector - Construction and Characterization. *Review of Scientific Instruments* **1989,** *60* (7), 2315-2317.

52. Gabriel, A. Position-Sensitive X-Ray Detector. *Review of Scientific Instruments* **1977,** *48* (10), 1303-1305.

53. Gabriel, A.; Dupont, Y. Position Sensitive Proportional Detector for X-Ray Crystallography. *Review of Scientific Instruments* **1972,** *43* (11), 1600-&.

54. Knoll, G. F. *Radiation Detection and Measurement;* 2nd ed.; Wiley: 1989.

55. Grupen, C.; Shwartz, B. *Particle Detectors;* 2nd ed.; Cambridge University Press: 2008.

56. Hubbell, J. H.; Seltzer, S. M. Tables of X-Ray Mass Attenuation Coefficients and Mass Energy-Absorption Coefficients (version 1.4). *NIST Online* [Online] Available: http://physics.nist.gov/xaamdi [2010 March 4] **2004**.

57. Niatel, M. T.; Perrocheroux, A. M.; Boutillon, M. 2 Determinations of W for Electrons in Dry Air. *Physics in Medicine and Biology* **1985,** *30* (1), 67-75.

58. Boutillon, M.; Perrocheroux, A. M. Reevaluation of the W-Value for Electrons in Dry Air. *Physics in Medicine and Biology* **1987,** *32* (2), 213-219.

59. Bellamy, H. D.; Butler, L. G.; Carver, D.; Choi, J.; Marceau-Day, L.; Dowben, P. A.; Ederer, D.; Goettert, J. S.; Keel, B.; Kumar, C.; Kurtz, R. L.; Meng, W. J.; Morilawa, E.; Morris, K.; Newcomer, M. E.; Poliakoff, E. D.; Roy, A.; Scott, J. D.; Sprunger, P.; Stevens, C. P.; Suller, V. P. *The ROSE Report: CAMD, Past, Present and Future*; 09.

60. Ilavsky, J.; Jemian, P. R. Irena: tool suite for modeling and analysis of small-angle scattering. *Journal of Applied Crystallography* **2009,** *42*, 347-353.

61. Sztucki, M.; Narayanana, T.; Beaucage, G. In situ study of aggregation of soot particles in an acetylene flame by small-angle x-ray scattering. *Journal of Applied Physics* **2007,** *101* (11).

62. Hyeon-Lee, J.; Beaucage, G.; Pratsinis, S. E.; Vemury, S. Fractal analysis of flame-synthesized nanostructured silica and titania powders using small-angle X-ray scattering. *Langmuir* **1998,** *14* (20), 5751-5756.

63. Blanton, T. N.; Barnes, C. L.; Lelental, M. Preparation of silver behenate coatings to provide low- to mid-angle diffraction calibration. *Journal of Applied Crystallography* **2000,** *33*, 172-173.

64. Huang, T. C.; Toraya, H.; Blanton, T. N.; Wu, Y. X-Ray-Powder Diffraction Analysis of Silver Behenate, A Possible Low-Angle Diffraction Standard. *Journal of Applied Crystallography* **1993,** *26*, 180-184.

65. Hubbard, C. R. New Standard Reference Materials for X-Ray-Powder Diffraction. *Advances in X-Ray Analysis* **1983,** *26*, 45-51.

66. Gilles, R.; Keiderling, U.; Wiedenmann, A. Silver behenate powder as a possible low-angle calibration standard for small-angle neutron scattering. *Journal of Applied Crystallography* **1998,** *31*, 957-959.

67. Keiderling, U.; Gilles, R.; Wiedenmann, A. Application of silver behenate powder for wavelength calibration of a SANS instrument - a comprehensive study of experimental setup variations and data processing techniques. *Journal of Applied Crystallography* **1999,** *32*, 456-463.

68. Santos, S. F.; Zanette, D.; Fischer, H.; Itri, R. A systematic study of bovine serum albumin (BSA) and sodium dodecyl sulfate (SDS) interactions by surface tension and small angle X-ray scattering. *Journal of Colloid and Interface Science* **2003,** *262* (2), 400-408.

69. Gelamo, E. L.; Itri, R.; Alonso, A.; da Silva, J. V.; Tabak, M. Small-angle X-ray scattering and electron paramagnetic resonance study of the interaction of bovine serum albumin with ionic surfactants. *Journal of Colloid and Interface Science* **2004,** *277* (2), 471-482.

70. Rigaku Americas - SAXS Aplication Byte: Turkey Tendon Collagen. *Rigaku Website* http://www.rigaku.com/saxs/saxs-app-006.html [Accessed 2010 March 4] **2010**.

71. Newkome, G. R.; Cho, T. J.; Moorefield, C. N.; Cush, R.; Russo, P. S.; Godinez, L. A.; Saunders, M. J.; Mohapatra, P. Hexagonal Terpyridine-Ruthenium and -Iron Macrocyclic Complexes by Stepwise and Self-assembly Procedures. *Chemistry-A European Journal* **2002,** *8* (13), 2946-2954.

72. Debye, P. J. W. Scattering of X-Rays. In *The collected papers of Peter J. W. Debye*, Interscience Publishers, Inc.: New York, 1954; pp 40-50.

73. Hall, C. E. A Low Temperature Replica Method for Electron Microscopy. *Journal of Applied Physics* **1950,** *21* (1), 61-62.

74. Steere, R. L. Electron Microscopy of Structural Detail in Frozen Biological Specimens. *Journal of Biophysical and Biochemical Cytology* **1957,** *3* (1), 45-&.

75. Moor, H.; Muhlethaler, K. Fine Structure in Frozen-Etched Yeast Cells. *Journal of Cell Biology* **1963,** *17* (3), 609-&.

76. Moor, H.; Waldner, H.; Muhlethaler, K.; Freywyssling, A. New Freezing-Ultramicrotome. *Journal of Biophysical and Biochemical Cytology* **1961,** *10* (1), 1-&.

77. Meyer, H. W.; Richter, W. Freeze-fracture studies on lipids and membranes. *Micron* **2001,** *32* (6), 615-644.

78. Severs, N. J. Freeze-fracture electron microscopy. *Nature Protocols* **2007,** *2* (3), 547-576.

79. Egelhaaf, S. U.; Wehrli, E.; Muller, M.; Adrian, M.; Schurtenberger, P. Determination of the size distribution of lecithin liposomes: A comparative study using freeze fracture, cryoelectron microscopy and dynamic light scattering. *Journal of Microscopy-Oxford* **1996,** *184*, 214-228.

80. Mondain-Monval, O. Freeze fracture TEM investigations in liquid crystals. *Current Opinion in Colloid & Interface Science* **2005,** *10* (5-6), 250-255.

81. Pollard, T. D.; Earnshaw, W. C. *Cell Biology;* 1st ed.; Elsevier, Inc.: Philadelphia, Pennsylvania, 2004.

82. Campbel, N. A.; Reece, J. B. *Biology;* 6th ed.; Pearson Education, Inc.: San Francisco, CA, 2002.

83. Takeo, K.; Uesaka, I.; Uehira, K.; Nishiura, M. Fine-Structure of Cryptococcus-Neoformans Grown In-Vitro As Observed by Freeze-Etching. *Journal of Bacteriology* **1973,** *113* (3), 1442-1448.

84. Fattakhova, R. N.; Suzina, N. E.; Dmitriev, V. V.; Fattakhov, T. N.; Duda, V. I. Invaginations of the cytoplasmic membrane in basidiomycetous yeasts. *Microbiology* **2003,** *72* (3), 385-387.

85. Nagle, J. F.; Tristram-Nagle, S. Lipid bilayer structure. *Current Opinion in Structural Biology* **2000,** *10* (4), 474-480.

86. Rand, R. P.; Parsegian, V. A. Hydration Forces Between Phospholipid-Bilayers. *Biochimica et Biophysica Acta* **1989,** *988* (3), 351-376.

87. Costigan, S. C.; Booth, P. J.; Templer, R. H. Estimations of lipid bilayer geometry in fluid lamellar phases. *Biochimica et Biophysica Acta-Biomembranes* **2000,** *1468* (1-2), 41-54.

88. Lis, L. J.; Mcalister, M.; Fuller, N.; Rand, R. P.; Parsegian, V. A. Interactions Between Neutral Phospholipid-Bilayer Membranes. *Biophysical Journal* **1982,** *37* (3), 657-665.

89. Gruner, S. M.; Tate, M. W.; Kirk, G. L.; So, P. T. C.; Turner, D. C.; Keane, D. T.; Tilcock, C. P. S.; Cullis, P. R. X-Ray-Diffraction Study of the Polymorphic Behavior of N-Methylated Dioleoylphosphatidylethanolamine. *Biochemistry* **1988,** *27* (8), 2853-2866.

90. Tristram-Nagle, S.; Petrache, H. I.; Nagle, J. F. Structure and interactions of fully hydrated dioleoylphosphatidylcholine bilayers. *Biophysical Journal* **1998,** *75* (2), 917-925.

91. Petrache, H. I.; Gouliaev, N.; Tristram-Nagle, S.; Zhang, R. T.; Suter, R. M.; Nagle, J. F. Interbilayer interactions from high-resolution x-ray scattering. *Physical Review e* **1998,** *57* (6), 7014-7024.

92. Buhleier, E.; Wehner, W.; Vogtle, F. Cascade-Chain-Like and Nonskid-Chain-Like Syntheses of Molecular Cavity Topologies. *Synthesis-Stuttgart* **1978,** (2), 155-158.

93. Hawker, C. J.; Frechet, J. M. J. Preparation of Polymers with Controlled Molecular Architecture - A New Convergent Approach to Dendritic Macromolecules. *Journal of the American Chemical Society* **1990,** *112* (21), 7638-7647.

94. Hawker, C. J.; Frechet, J. M. J. A New Convergent Approach to Monodisperse Dendritic Macromolecules. *Journal of the Chemical Society-Chemical Communications* **1990,** (15), 1010-1013.

95. Newkome, G. R.; Moorefield, C. N.; Vogtle, F. *Dendrimers and Dendrons: Concepts, Syntheses, Applications;* Wiley-VCH: Weinheim, Germany: 2001.

96. Sun, J. Self-Assembly and Its Inhibition in Bolaform Amphiphilic Dendrimers. Ph.D.Dissertation Louisiana State University, 2006.

97. Newkome, G. R.; Baker, G. R.; Saunders, M. J.; Russo, P. S.; Gupta, V. K.; Yao, Z. Q.; Miller, J. E.; Bouillion, K. 2-Directional Cascade Molecules - Synthesis and Characterization of [9]-N-[9] Arborols. *Journal of the Chemical Society-Chemical Communications* **1986,** (10), 752-753.

98. Provencher, S. W. A Constrained Regularization Method for Inverting Data Represented by Linear Algebraic or Integral Equations. *Compo Phys.* **1982,** *27*, 213-227.

99. Provencher, S. W. Contin: A General Purpose Constrained Regularization Program for Inverting Noisy Linear Algebraic and Integral Equations. *Compo Phys.* **1982,** *27*, 229-242.

100. Hallett, F. R.; Watton, J.; Krygsman, P. Vesicle Sizing - Number Distributions by Dynamic Light-Scattering. *Biophysical Journal* **1991,** *59* (2), 357-362.

101. Pencer, J.; Hallett, F. R. Small-angle Neutron Scattering from Large Unilamellar Vesicles: An Improved Method for Membrane Thickness Determination. *Physical Review e* **2000,** *61* (3), 3003-3008.

102. Pencer, J.; Barnett, E.; White, G.; Hallett, F. R. Osmotically Induced Shape Changes to Large Unilamellar Vesicles: Effects of Lipid and Solute Composition. *Biophysical Journal* **2000,** *78* (1), 156A.

103. Hope, M. J.; Cullis, P. R. Bilayer Stability of Inner Monolayer Lipids from the Human-Erythrocyte. *FEBS Letters* **1979,** *107* (2), 323-326.

104. Liang, X. M.; Mao, G. Z.; Ng, K. Y. S. Mechanical properties and stability measurement of cholesterol-containing liposome on mica by atomic force microscopy. *Journal of Colloid and Interface Science* **2004,** *278* (1), 53-62.

105. Liu, D. Z.; Chen, W. Y.; Tasi, L. M.; Yang, S. P. Microcalorimetric and shear studies on the effects of cholesterol on the physical stability of lipid vesicles. *Colloids and Surfaces A-Physicochemical and Engineering Aspects* **2000,** *172* (1-3), 57-67.

106. Liu, D. Z.; Chen, W. Y.; Tsai, L. M.; Yang, S. P. The effects of cholesterol on the release of free lipids and the physical stability of lecithin liposomes. *Journal of the Chinese Institute of Chemical Engineers* **2000,** *31* (3), 269-276.

107. Mecke, A.; Lee, I.; Baker, J. R.; Holl, M. M. B.; Orr, B. G. Deformability of Poly(amidoamine) Dendrimers. *European Physical Journal e* **2004,** *14* (1), 7-16.

VITA

Derek Richard Dorman was born in Jackson, Mississippi, in 1978, to Alice and Richard Dorman. Derek completed grades K-12 through the Jackson Public School system and was accepted to an extracurricular arts program, Academic and Performing Arts Complex (APAC), from grades 4-8th. Derek attended Wingfield High School where he was an active member in student government, serving as sophomore and junior class treasurer and finally, senior class president. He was member of Mu Alpha Theta and Science Olympiad placing in several of the state competitions. Derek was the valedictorian and graduated in May 1996.

Derek was accepted to The University of Southern Mississippi School of Polymers and High Performance Materials in August 1996. While attending Southern Miss, he worked in the lab of Professor Robert Y. Lochhead and presented work on "*Interfacial surface tension activity and emulsion stability of hydrophobically modified dextran and glycogen*" at the 63rd annual meeting of the Mississippi Academy of Sciences in Tupelo, Mississippi. He graduated with a Bachelor of Science degree in December 2000 and accepted a computer technician position with the Office of Technology Resources at Southern Miss.

In 2002 Derek was accepted to Louisiana State University and received a Graduate Student Enhancement award to pursue a Doctor of Philosophy in chemistry. He joined the Macromolecular Studies Group, was awarded a National Science Foundation Integrative Graduate Education Research Training Program (NSF-IGERT) Fellowship for the Teaching

Craft for Macromolecular Creativity (CMC), and began working in the laboratory of Dr. Paul S. Russo in January, 2003.

While at LSU, Derek attended several national and local scientific meetings. He attended the 2007 and 2008 American Physical Society March meetings and presented a poster at each. He was awarded two CMC-IGERT grant proposals totaling $10,000 to perform research abroad. Derek will receive his Ph.D. on August 6, 2010, during the summer commencement ceremony.